Cosmic Ray Energy Spectrum Measurement with the Antarctic Muon and Neutrino Detector Array (AMANDA)

by

Dmitry Aleksandrovich Chirkin

B.A. (Moscow Institute of Physics and Technology) 1996
M.S. (University of California at Berkeley) 1998

A dissertation submitted in partial satisfaction of the
requirements for the degree of
Doctor of Philosophy

in

Physics

in the

GRADUATE DIVISION
of the
UNIVERSITY of CALIFORNIA at BERKELEY

Committee in charge:

Professor Buford Price, Chair
Professor Hitoshi Murayama
Professor Alex Filippenko

Fall 2003

The dissertation of Dmitry Aleksandrovich Chirkin is approved:

_____

Chair   Date

_____

Date

_____

Date

University of California at Berkeley

Fall 2003

Cosmic Ray Energy Spectrum Measurement with the Antarctic Muon and Neutrino

Detector Array (AMANDA)

Copyright 2003

by

Dmitry Aleksandrovich Chirkin

Abstract

Cosmic Ray Energy Spectrum Measurement with the Antarctic Muon and Neutrino

Detector Array (AMANDA)

by

Dmitry Aleksandrovich Chirkin

Doctor of Philosophy in Physics

University of California at Berkeley

Professor Buford Price, Chair

AMANDA-II is a neutrino telescope composed of 677 optical sensors organized along 19 strings

buried deep in the Antarctic ice cap. It is designed to detect Cherenkov light produced by cosmic-

ray- and neutrino-induced charged leptons. The majority of events recorded by AMANDA-II are

caused by muons which are produced in the atmosphere by high-energy cosmic rays. The lead-

ing uncertainties in simulating such events come from the choice of the high-energy model used

to describe the first interaction of the cosmic rays, uncertainties in our knowledge and implemen-

tation of the ice properties at the depth of the detector, and individual optical module sensitivities.

Contributions from uncertainties in the atmospheric conditions and muon cross sections in ice are

smaller.

The downgoing muon simulation was substantially improved by using the extensive air shower generator CORSIKA to describe the shower development in the atmosphere, and by writing a new software package for the muon propagation (MMC), which reduced computational and algorithm errors below the level of uncertainties of the muon cross sections in ice.

A method was developed that resulted in a flux measurement of cosmic rays with energies $1.5 - 200$ TeV per nucleon (95% of primaries causing low-multiplicity events in AMANDA-II have energies in this range) independent of ice model and optical module sensitivities. Predictions of six commonly used high-energy interaction models (QGSJET, VENUS, NEXUS, DPMJET, HDPM, and SIBYLL) are compared to data. The best agreement with direct measurements is achieved with QGSJET, VENUS, and NEXUS. Assuming a power-law energy spectrum ($\Phi_{0,i} \cdot E^{-\gamma_i}$) for cosmic-ray components from hydrogen to iron ($i = H, ..., Fe$) and their mass distribution according to Wiebel-Sooth (Wiebel-Sooth & Biermann, 1999), $\Phi_{0,i}$ and γ_i were corrected to achieve the best description of the data. For the hydrogen component, values of $\Phi_{0,H} = 0.106 \pm 0.007$ $\text{m}^{-2}\text{sr}^{-1}\text{s}^{-1}\text{TeV}^{-1}$, $\gamma_H = 2.70 \pm 0.02$ are obtained. For the South Pole, a vertical muon flux at 1 TeV of $(1.05 \pm 0.07) \cdot 10^{-10}$ $\text{cm}^{-2}\text{sr}^{-1}\text{s}^{-1}\text{GeV}^{-1}$ is obtained (for all interaction models), and the fitted spectral index is 2.66 ± 0.02 (for QGSJET, VENUS, and NEXUS). The difference in the predicted value of the spectral index γ between high-energy interaction models is as much as 0.1, which is explained by the difference in the observed muon multiplicity at the depth of the detector in data simulated with different interaction models.

Professor Buford Price
Dissertation Committee Chair

To my Mom,

for I can always count on you.

Contents

List of Figures

List of Tables

Acknowledgements

It gives me great pleasure, having concluded this thesis, to acknowledge all the wonderful people who helped me advance this work. I enjoyed a fruitful collaboration with my friends in Berkeley, most of all Kurt Woschnagg and Predrag Miočinović, and during my visit to Wuppertal, with Frank Schröder and Ulf Kleinevoß.

I would have likely been searching for a field of study for much longer, had it not been for Wolfgang Rhode, who introduced the field of astrophysics to me, and was able to fascinate me with the concept of the AMANDA detector. I have enjoyed collaborating with him throughout the years and am very thankful for his suggestion of several projects.

Many thanks to Tom Gaisser, who helped me clarify my explanation of the features of the data. I hope this thesis correctly conveys the ideas we developed. I would like to thank Paolo Desiati, Stephan Hundertmark, Heiko Geenen, and Peter Steffen for helping me write and debug software needed for my thesis. Many thanks to Steve Barwick, Per Olof Hulth, Robert Morse, and the many other members of the AMANDA and IceCube collaborations, who have expressed interest in my work and provided me with inspiration to continue this research.

I would like to thank Shigeru Yoshida and the wonderful people of the Chiba group who came to my rescue while I was delayed in Japan. Their kind attitude allowed me to finish a large part of the final results of this thesis during my stay there.

Most of all I thank my adviser Buford Price for guidance and inspiration, for the freedom permitted me while searching for a suitable problem to study, and his enthusiastic support of the topic I chose to research. I would not have been able to find a subject I have enjoyed so much had it not been for his incredible ability to generate ideas and make them available to me.

AMANDA
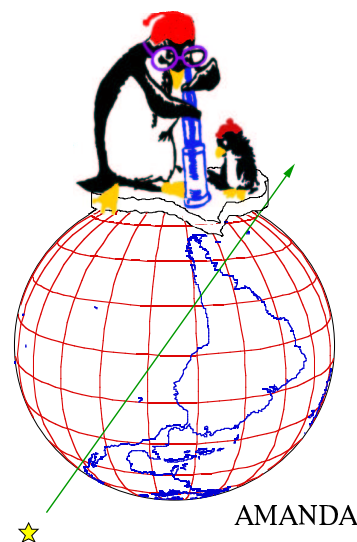
Chapter 1

Introduction

- If there is a solution, there must have been a problem -

An important goal of astrophysics is to understand the properties of cosmic rays, the energy spectrum of which spans over many orders of magnitude (Figure 1.1). For almost six decades in energy up to about $5 \cdot 10^{15}$ eV (the "knee" in the spectrum) the spectrum follows a power law, $dN/dE \propto E^{-\gamma}$, with a spectral index of $\gamma \approx 2.7$. The chemical composition and energy spectra of the cosmic rays have been measured by balloon and satellite experiments (direct measurements) [1] in the energy range below 100 TeV. Various ground-based experiments complement these data for energies above 1 TeV (indirect measurements). The mechanism which leads to the power law dependence was known as "Fermi" acceleration since 1949 [2], however not until 1978 [3] was the spectral index of ~ 2.7 possible to explain (with the first order Fermi acceleration mechanism, see also [4] and [5], together with models of propagation, which describe the escape rate of the cosmic rays from the Galaxy [6], e.g., the so-called leaky-box model, [5]).

Cosmic rays arriving at Earth consist of nuclei, electrons, gamma rays, and neutrinos (Figure 1.2). Charged particles change their direction in the Galactic and extragalactic magnetic
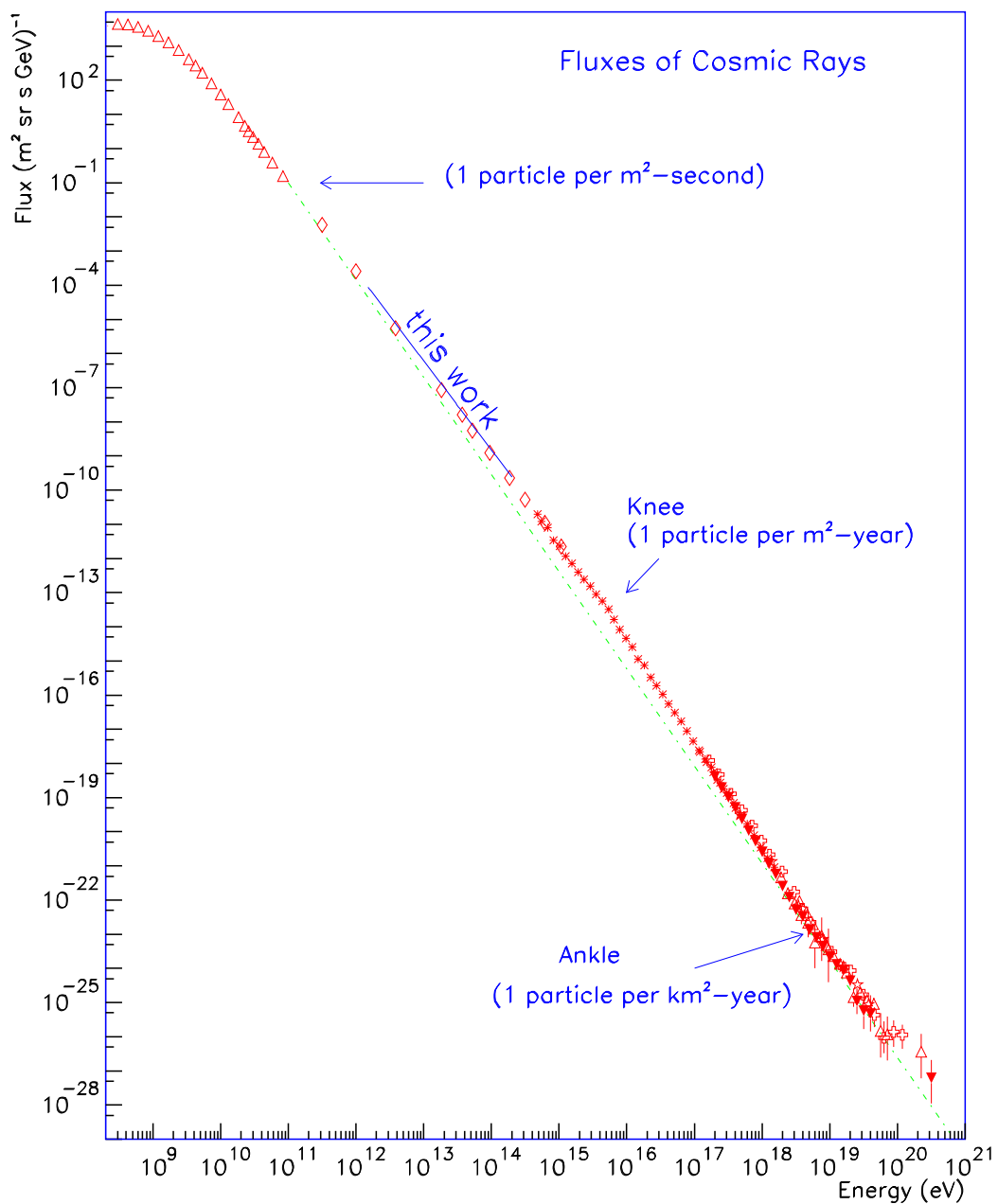
Figure 1.1: Energy spectrum of cosmic rays, figure adapted from [7]. Results of this work (Chapter 5) are shown with blue solid line in the region of AMANDA-II sensitivity

fields, and gamma rays are absorbed by interstellar dust, which makes neutrinos very interesting due to their neutrality and extremely small interaction with matter.
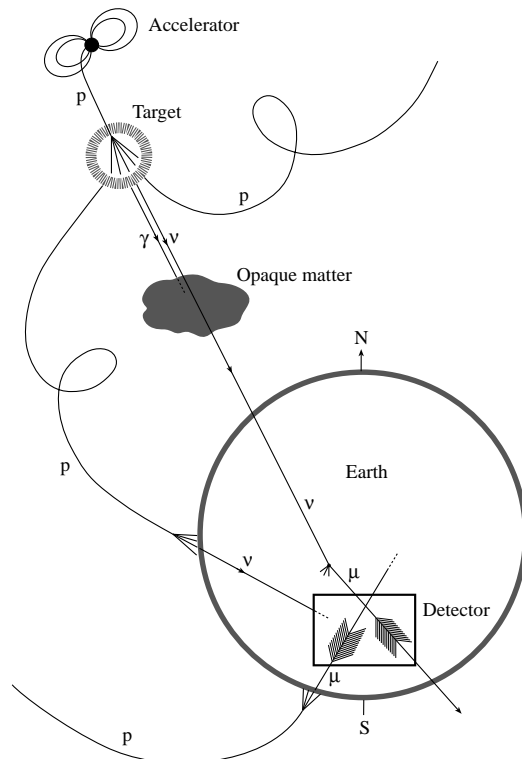
Figure 1.2: Different constituents of cosmic rays, from [8]. Behavior of charged components with Z>1 is similar to that of p
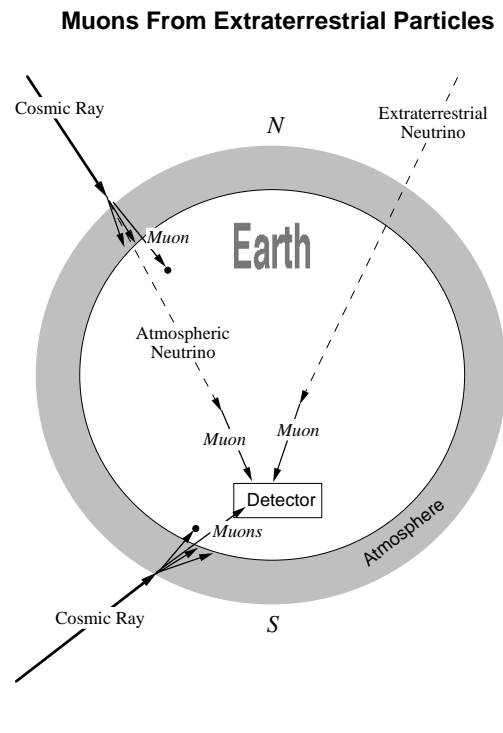
Figure 1.3: Production of muons seen by AMANDA-II, from [9]

A detection volume of ~ 1 km^3 is necessary for detection of high-energy extraterrestrial neutrinos [10]. Several large underwater/ice detectors (AMANDA, Antares, Baikal, IceCube, NESTOR, NEMO) designed to search for extraterrestrial neutrinos are presently at different stages of planning and operation. These telescopes look for Cherenkov photons in a naturally occurring transparent medium [11]. The signal consists of muons, stemming from interactions of cosmic neutrinos in or close to the detector, and the main background consists of muons from air showers initiated by charged cosmic rays (Figure 1.3).
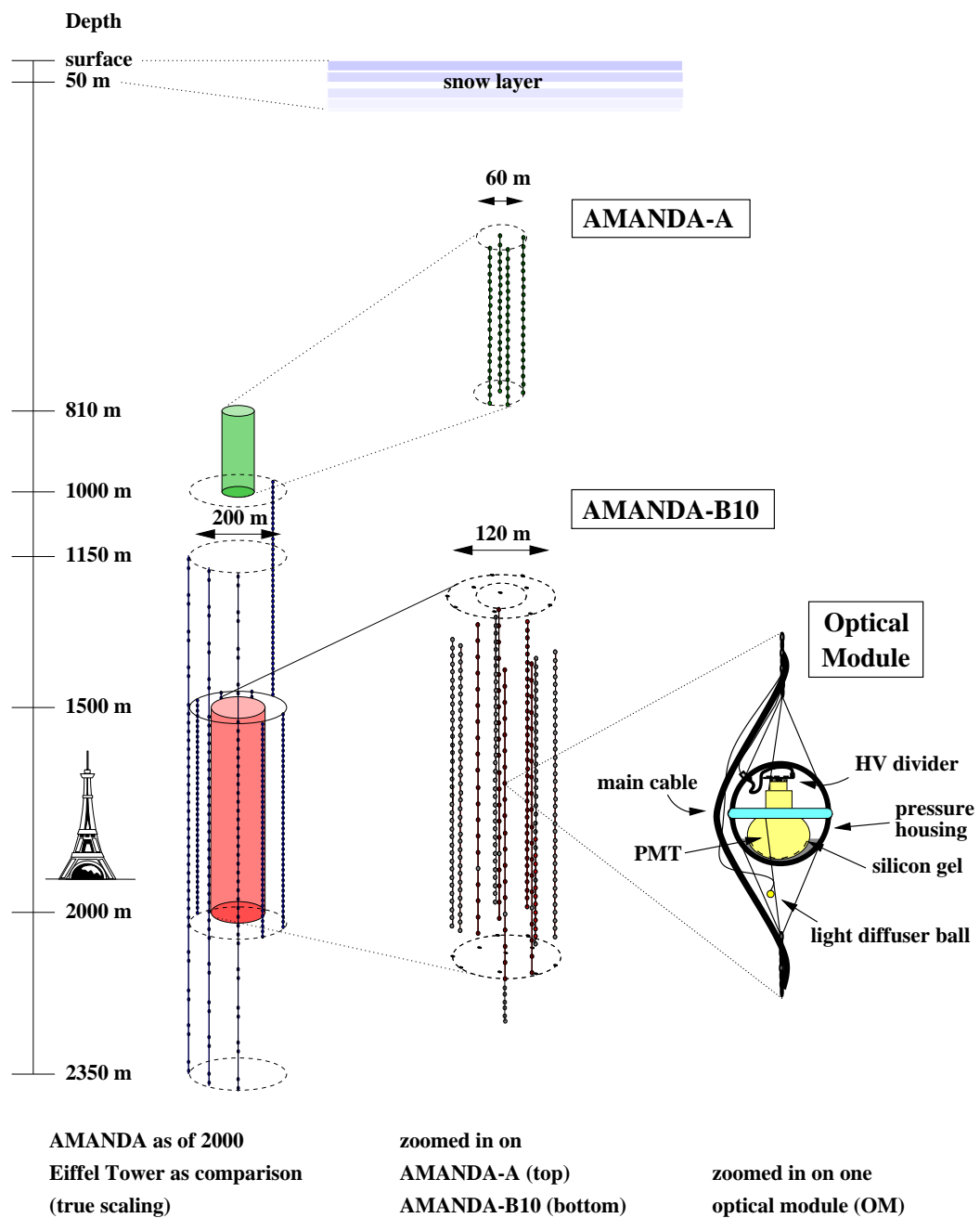
Figure 1.4: AMANDA-II telescope view

AMANDA-II (Antarctic Muon and Neutrino Detector Array, as operated since year 2000, [12]) is a neutrino telescope composed of 677 optical sensors organized along 19 strings buried deep in the Antarctic ice cap (Figure 1.4). The signal consists of hits produced by Cherenkov photons emitted by muons passing through ice (Figure 1.5).
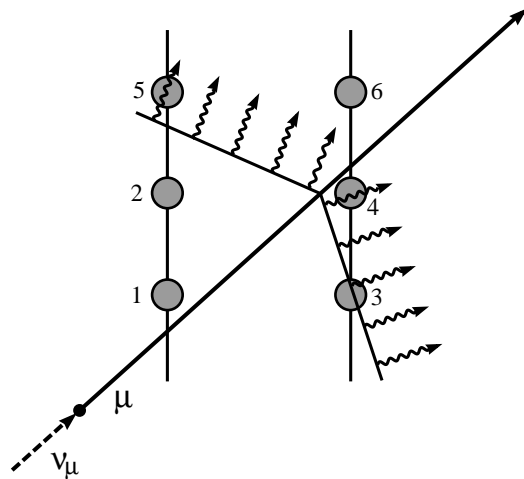
Figure 1.5: Cherenkov photons in ice, from [8]
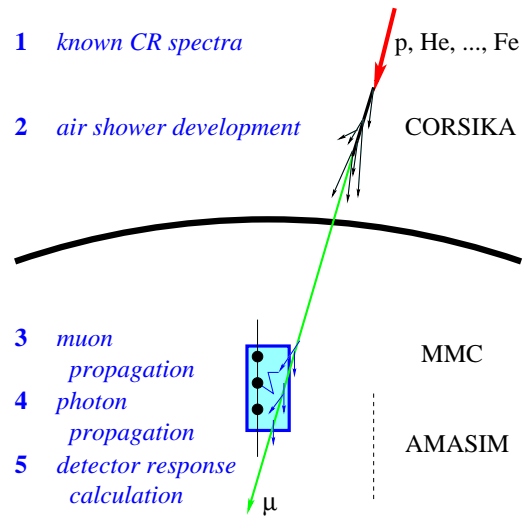
Figure 1.6: Data simulation chain

Although the primary goal of AMANDA-II is to observe a possible extra-terrestrial neutrino signal, the majority of events in AMANDA-II are caused by downward-going muons and neutrinos produced in the atmosphere by high-energy cosmic rays (Figure 1.7). It is therefore possible to use AMANDA-II data to indirectly measure the flux of cosmic rays in the energy range where AMANDA-II is most sensitive ($\sim 1 - 100$ TeV). As shown in this work, AMANDA-II provides important additional data in the transitional region between direct and indirect measurements, where significant disagreement between experiments exists (of up to 50%, as seen in [13]). Moreover, AMANDA-II does this by using the penetrating muon component of the cosmic-ray induced
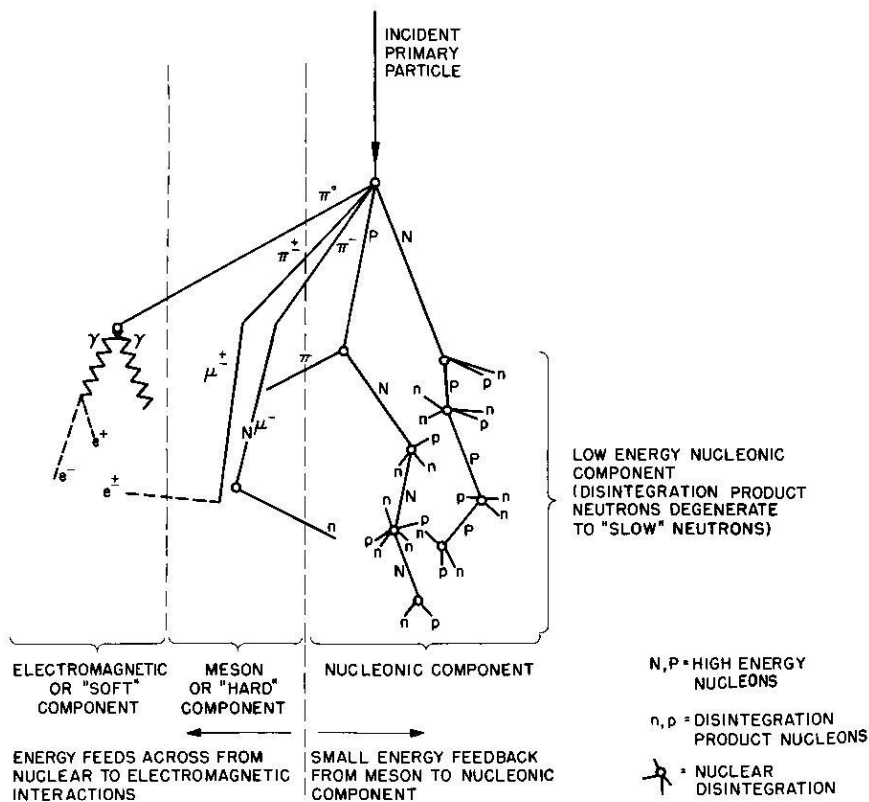
Schematic Diagram of Cosmic Ray Shower

Figure 1.7: Shower development in the atmosphere, from [14]

air showers (as opposed to the e-m component[1]), thus providing a different test of the interaction models widely used to explain data from air shower experiments.

To measure the cosmic ray flux with AMANDA-II, comparison of data with a detector simulation is necessary. In the Monte Carlo simulations (Figure 1.6), a power law energy spectrum of the cosmic ray components with relative abundances taken from [1] (Appendix A) was assumed. Overall normalization and spectral index were varied to match experimental data with simulated data. CORSIKA [15] (versions 6.016 and 6.018) was used to generate the muon flux at the ice

---

[1]Electrons and photons, which provide the signal for the majority of the surface arrays in this energy range.

surface from the assumed cosmic ray flux. Simulation was performed for six high-energy models available with CORSIKA. Muons were propagated through ice to and through the detector with MMC [16] (version 1.08). To generate Cherenkov photons and simulate AMANDA-II response, the detector simulation program AMASIM [17] (version 2.73.14) was used.

Emphasis was put on understanding and minimizing systematic uncertainties. The systematic uncertainty in the knowledge of atmospheric conditions was estimated by comparing experimental and simulated data from several different periods during the year 2000. The uncertainty in the muon cross sections in ice is less than 1% [18] (Section 3.10). Errors due to approximations in the muon propagation algorithm and computational errors were estimated to be much smaller [19] (Section 3.4). The knowledge of the ice density profile and the depth of the optical modules (OM) introduces an error of less than 1 m, which contributes less than 1% to the uncertainty in muon propagation.

To minimize hardware-related uncertainties, the number of muon events seen at the depth of each optical module of the detector was calculated using a method described in Section 4.3. The distribution of noise hits was determined from data uncorrelated with the muon signal. This distribution was folded with the distribution of hits coming from observed Cherenkov photons emitted by muons inside the detector. To account for photons from muons passing close to a given OM which are possibly missed by that OM, the *efficiency* of that OM was determined by analyzing the signal in the surrounding OMs (i.e., in the OMs above and below the given OM). To calculate the number of muons seen by the detector, noise is subtracted and the signal missed as a result of an efficiency $< 100\%$ is added to the signal recorded by each OM. This method is most precise for the OMs located close to the center of the detector.

The largest uncertainties in the simulation chain come from the photon propagation and detector signal simulation. These are estimated to be 15% for absolute OM sensitivities and 20% for optical properties of ice. A method presented in Chapter 4 attempts to make the flux measurement insensitive to these uncertainties.

Several energy reconstruction techniques (calibrated with Monte Carlo simulations) have been used to reconstruct cosmic ray and muon energy spectra with AMANDA [20, 21, 22]. These methods use simulated data twice: to calibrate the energy reconstruction method, and then to build the kernel for the unfolding algorithm. In this work, simulated data are only used once in a way which places the main emphasis on reduction of systematic uncertainties. Results are quoted with much smaller uncertainties than in previous works.

Chapter 2

Air Shower Generation with CORSIKA

- Second things first -

2.1 Introduction

In order to simulate the AMANDA-II muon background, which for the purpose of this work is the actual signal, protons and heavier nuclei are generated at the top of the atmosphere and propagated down to the Earth's surface using the air shower generator CORSIKA [23]. The resulting air showers contain muons and neutrinos, which are propagated through the ice to the detector. Neutrinos occasionally interact with ice or underlying bedrock producing muons; however, their signal is typically four orders of magnitude lower than signal from muons created in the atmosphere (see, e.g., [24]) and is ignored in this work. Cherenkov photons created in the ice by high-energy muons are propagated to optical receivers. This results in Monte Carlo simulated data, which are compared to the experimental data.

This section discusses modifications to CORSIKA that were made to ensure an accurate

representation of the conditions of the AMANDA-II experiment.

2.2 CORSIKA settings

The air shower generator used to simulate AMANDA-II data is based on CORSIKA (versions 6.018 and 6.020). All six high-energy interaction models QGSJET, VENUS, NEXUS, DPM-JET, HDPM, and SIBYLL [23, 25] (see Table 2.1 for comparison of basic features) available with CORSIKA were tested.

Table 2.1: Basic features of hadronic interaction models (from [26]). Execution times are given for 1 GHz P3 computer with optimal AMANDA-II settings determined in this chapter: $E_{low,pri} = 600$ GeV, $E_{low,\mu} = 273$ GeV. Model features and assumptions listed in the first column are explained in [27].

	QGSJET	VENUS	NEXUS	DPMJET	HDPM	SIBYLL
Gribov-Regge	+	+	+	+		
Minijets	+		+	+		+
Sec. Interactions		+	+			
N-N Interactions	+	+	+	+		
Superposition					+	+
Max. Energy (GeV)	$> 10^{11}$	$2 \cdot 10^7$	$2 \cdot 10^8$	$> 10^{11}$	10^8	$> 10^{11}$
CPU time/shower (ms)	0.8	30	365	73	1.6	1.1

Cosmic rays with their energy spectra (parametrized as $\Phi_i(E) = \Phi_0^i E^{-\gamma}$ for $i = $ H...Fe) and relative abundances from [1] (Appendix A) were used as primaries in CORSIKA.

The zenith-angle distribution function of primaries was changed from the default for a flat detector to $dN \propto d\Omega \cdot (\pi r^2 \cdot \cos\theta + l \cdot 2r \cdot \sin\theta)$ for a cylindrical detector with radius r and length l (Figure 2.1). This modification better represents the AMANDA-II detector geometry and simplifies the following analysis.

In order to save disk space and computing time the detailed Monte Carlo simulation of e-m cascades can be substituted with the results of the Nishimura, Kamata, and Greisen (NKG)
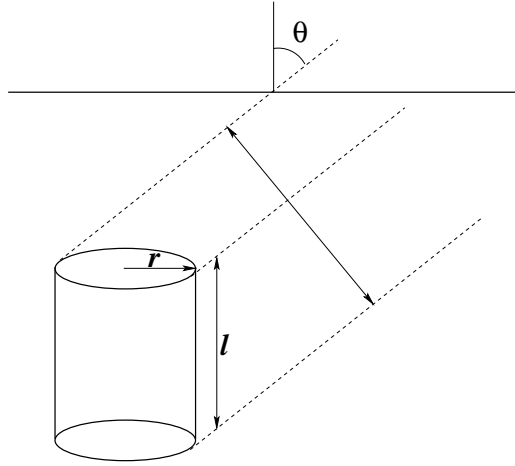
Figure 2.1: Zenith-angle dependent geometrical area of the detector

analytical description of the electromagnetic shower, only recording the age parameter s and number

of particles N_e. The average distribution of particles on the observation level can then be obtained

from the NKG formula, as given in [23]:

$$\rho_e = \frac{N_e}{2\pi r_{mol}^2 s_m^2} \frac{\Gamma(4.5 - s)}{\Gamma(s)\Gamma(4.5 - 2s)} \left(\frac{r}{r_{mol} s_m}\right)^{s-2} \left(1 + \frac{r}{r_{mol} s_m}\right)^{s-4.5},$$

where $s_m = 0.78 - 0.21s$, $r_{mol} = 9.6g \cdot cm^{-2}/\rho_{air} =$ Moliere radius. This approach can be used

to correlate the muon signal with the e-m component at the surface. It neglects the photoproduction

of pions and may lead to some loss in number of secondaries. As of version 6.020 of CORSIKA,

however, it can only be used together with the flat atmosphere approximation.

Profiles of the atmosphere at the location of the South Pole were generated with the MSIS-

E-90 (Mass Spectrometer and Incoherent Scatter Extended Model) program (available at [28]) for

March 31, July 1, October 1, and December 31 (Figure 2.2). No significant change for each season

from year to year (1997 to 2001) was found. October 1 and March 31 represent the typical behavior

over the year, the October profile being taken as the default for the background muon simulation.
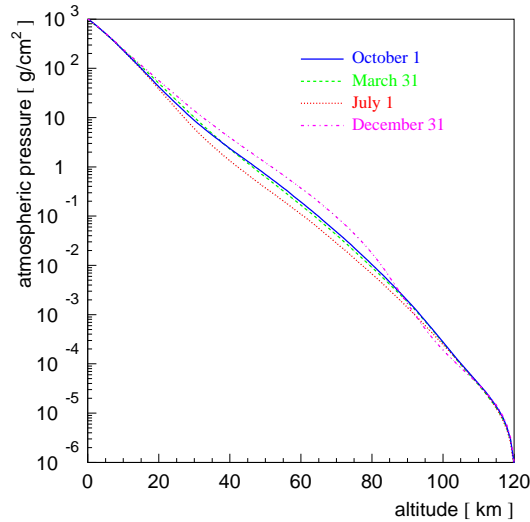
Figure 2.2: Comparison of four South Pole atmospheres

To determine the magnetic field, a National Geophysical Data Center (NGDC) program (available at [29]) was used. For the South Pole on January 31, 1998 a field of 55911 nT with the declination of $-27°43.0'$ (from a zero meridian) and inclination of $-72°54.5'$ was obtained. No significant variation from these values during years 1997 to 2001 was observed.

2.3   Zenith angle distributions

The CORSIKA frame of reference is mapped into the detector frame. This is not necessary if the surface of the Earth can be considered flat. The muons which travel at angles affected by this transformation (above $\theta = 88°$) have to travel through more than 45 km of ice (48.7 km for a flat surface geometry) to reach the detector. As follows from the results of Section 2.4, less than 0.1% of muons with energies as high as 26.6 PeV can penetrate through this much ice. From Section 3.7 the typical energy of a muon that travels this far is $1.5 \cdot 10^{20}$ eV. While irrelevant to

the background muon analysis, a correct treatment of these muons may be required for ultra-high energy (UHE) analysis of the AMANDA-II data. Additionally, it allows a mapping of the good CORSIKA region that exhibits no suppression (due to shower propagation algorithm imperfections, [30], $0°$ to $88.67°$) into the whole range of zenith angles from $0°$ to $90°$ in the detector frame (Figure 2.3).

$$\sin\theta_c = \sin\theta_d(1 - h/R)$$
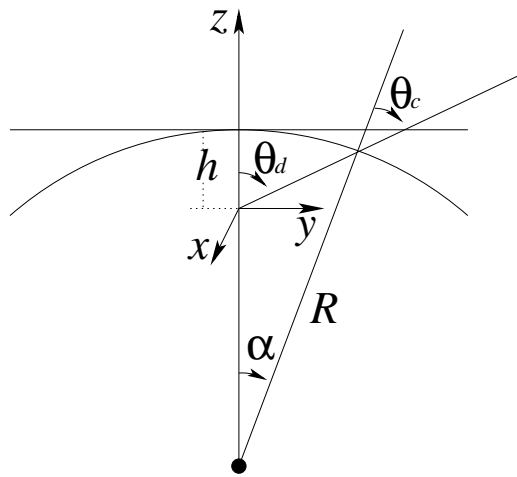
Figure 2.3: CORSIKA (θ_c) to detector (θ_d) angle mapping

All shower coordinates and angles are transferred from the CORSIKA (c) frame of reference to the detector (d). To ensure that the magnetic field direction is described as well as possible, the CORSIKA frame is chosen so as to match the detector frame by one rotation by α, performed around the center of the Earth. The coordinate transformation between the two frames can be written as

$$
\left\| \begin{matrix} x_d \\ y_d \\ z_d \end{matrix} \right\| = A \cdot \left[\begin{pmatrix} \cos\alpha\cos\phi & \cos\alpha\sin\phi & \sin\alpha \\ -\sin\phi & \cos\phi & 0 \\ -\sin\alpha\cos\phi & -\sin\alpha\sin\phi & \cos\alpha \end{pmatrix} \cdot A^T \left\| \begin{matrix} x_c \\ y_c \\ z_c \end{matrix} \right\| + \left\| \begin{matrix} R\sin\alpha \\ 0 \\ R(\cos\alpha - 1) \end{matrix} \right\| \right]
$$

$$
\text{with} \quad A = \begin{pmatrix} \cos\phi & -\sin\phi & 0 \\ \sin\phi & \cos\phi & 0 \\ 0 & 0 & 1 \end{pmatrix}
$$

Here ϕ is the azimuth angle of the primary. The values of x_c, y_c are randomized inside the projection of the cylinder of the detector on the surface of the Earth made along the direction of the primary. CORSIKA coordinates (x_c, y_c, z_c) are given inside the plane tangent to the surface of the Earth at an intersection point of the shower core with the surface, therefore $z_c = 0$. Once in the detector frame, all particles are propagated from the tangent plane to the surface of the Earth. A similar transformation was applied to the angles at which particles enter the surface. The change in the magnetic field direction introduced by this transformation is given by the rotation angle α, the maximum value of α in the upper hemisphere being $1.3°$.

To preserve the correct (isotropic) angular distribution of the primaries, the zenith angle is first determined by CORSIKA at random in the detector frame (θ_d) and then translated into the internal CORSIKA angle (θ_c). This translation is enabled by the new INPUTS file (see Appendix F.1) flag "SCURV T 6.4E8 1.73E5". The shower core location is randomized by program "ucr" with a "-curved=[1-4]" flag. To apply curved randomization,"ucr" is run with the following flags: "-LENGTH=[l] -RADIUS=[r] -HEIGHT=2834 -EARTHR=6.4e6 -DEPTH=[1730 or 1695] -curved=4 -cutth=85". This enables 2x oversampling of muons coming from zenith angles

$85° < \theta < 90°$ thus including primaries with $\theta > 90°$ into the analysis. Some of these upgoing primaries create a number of downgoing muons through scattering or by being deflected in the magnetic field. The ratio l/r must correspond to the ratio $l/d = l/2r$ specified by the flag DETCFG in the INPUTS file.

Since the same angle θ_c can translate into two different angles θ_d, it is possible to generate upgoing flux at the shower core randomization stage (by "ucr") from the same CORSIKA files as downgoing. Options "-curved=4 -cutth=$[\theta_{cut}]$" allow one to oversample (x2 on top of the existing oversampling number set by "-over=[number]") events originating from primaries with zenith angles $\theta_{cut} \leq \theta \leq 90°$ in the detector frame. This allows one to generate reliable results with only slightly bigger Monte Carlo files (and almost no increase in execution time, since "ucr" is extremely fast).

Figure 2.4 shows the muon zenith angle distribution for angles from $0°$ to $180°$. The distribution looks somewhat symmetric (around $\cos \theta = 0$) because each event was used twice: once as downgoing and once as upgoing (this is enabled by the "-curved=4 -cutth=0" options). The number of entries in the distribution follows $1/\cos \theta$ at small angles (according to [31]) and flattens at the horizon which is consistent with the following facts.

The number of created muons is proportional to the pion mean free path at the top of the atmosphere. This increases as $1/\cos \theta$ only at small zenith angles, slowing down near the horizon.

A 400 GeV muon has a decay length of 2500 km. Such a muon is on average produced at an altitude of 24 km or higher for larger zenith angles. A horizontal muon travels more than 550 km before entering the ice. It has at least a 20% chance of decaying before entering the detector. This probability depends exponentially on the traveled distance and grows fast for zenith angles
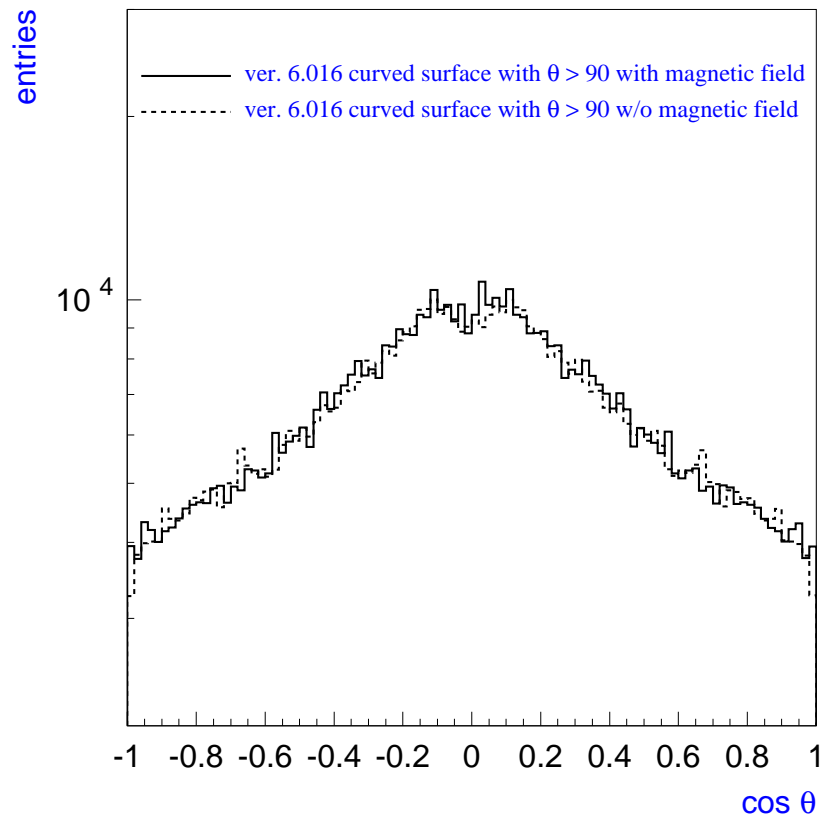
Figure 2.4: Muon zenith angle distribution from $0°$ to $180°$

approaching $90°$. A small reduction of the muon flux at the horizon is therefore expected.

The muon energy loss is proportional to the mass overburden of air it crossed. This mass overburden grows from 7 mwe[1] (at the South Pole) for a vertical muon track to 149 mwe for a horizontal track. A 400 GeV muon traveling to the surface loses on average 2.8 GeV for a vertical track and 60 GeV for a horizontal track. If a constant muon energy threshold is maintained for all zenith angles, then the number of muons left with energies above this threshold after propagating to the observation point is smaller at larger zenith angles. For the muon energy distribution with spectral index 2.7 to 3.7 the reduction of integrated muon flux for $\theta = 0°$ is 1.2% to 1.9%, while for

---

[1]Meters of water equivalent.

$\theta = 90°$ this reduction is 21% to 31%. Clearly, this further reduces the number of horizontal muon tracks, while leaving the number of vertical muon tracks almost unchanged.

2.4   Optimization of CORSIKA settings

CORSIKA allows the user to filter out events in which the primary has insufficient energy to produce a muon that would reach the detector. This feature saves computational time and disk space and is enabled by the "LOCUT T" flag. It is also possible to remove muons (and whole events containing only such muons) that are in the CORSIKA output but cannot reach the detector. This mainly saves disk space and can be done at the shower core randomization ("ucr") stage using the "-cutfe=[E_{low}]" flag.

The energy of a muon is compared to the function $E_{cut}(x)$ of the ice thickness x, which is the minimum energy the muon is required to have to reach a certain depth h. During the CORSIKA step the energy of the muon for such comparison is assumed to be smaller than some fraction ν of the energy of the primary. The depth h is determined from the condition $E_{cut}(h) = E_{low}$, where E_{low} is the energy below which muons are not recorded by CORSIKA (specified by "ECUTS [E_{low}] ..." flag in the INPUTS file) or the value of the "-cutfe=[E_{low}]" flag used by "ucr" (usually equal to the first argument of the "ECUTS" flag in the corresponding INPUTS file).

The slant depth x is given by $h/\cos\theta$ where θ is the zenith angle of the particle (muon or primary) in the CORSIKA frame of reference. This is a good value even when the surface of the Earth is considered curved as it consistently filters out particles that cannot reach a spherical subsurface located at the depth h below the Earth's surface.

To determine the function $E_{cut}(x)$, MMC (see Chapter 3) was run for ice as propagation
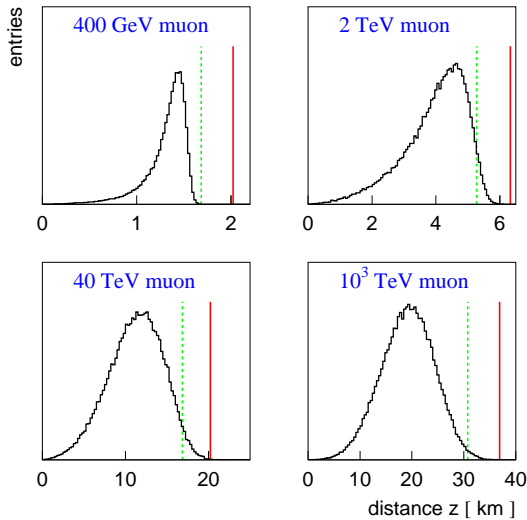
Figure 2.5: Muon range distributions in ice
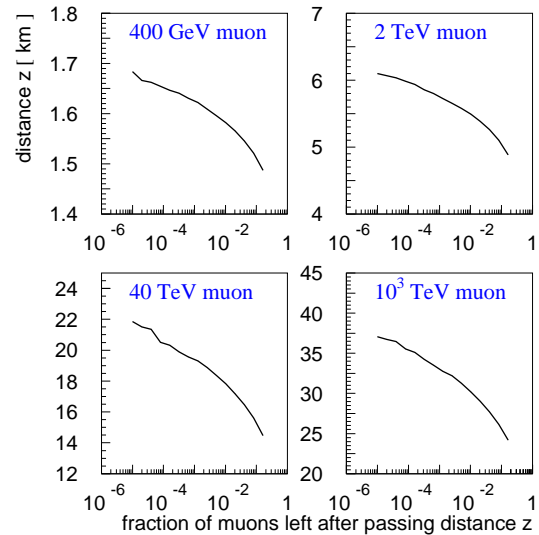
Figure 2.6: Distance in ice vs. survived muons

medium, with muon energies from 105 MeV to 10^{20} eV. For each energy 10^5 muons were propagated to the point of their disappearance and the distance traveled was histogrammed (Figure 2.5). This is similar to the analysis done in Chapter 3.7 (also in [32]). However, instead of the average distance traveled, the distance at which only a fraction of muons survives was determined for each muon energy (Figure 2.6). Two fixed fractions were used: 99% and 99.9%. MMC was run with 2 different settings: $v_{cut} = 10^{-2}$ with the *cont* (*continuous randomization* feature described in Chapter 3.3.2) option and $v_{cut} = 10^{-3}$ without *cont*. In Figure 2.7 the ratio of distances determined with both settings is displayed for 99% of surviving muons (red line) and for 99.9% (green line). Both lines are very close to 1.0 in most of the energy range except the very low energy part (below 2 GeV) where the muon does not suffer enough interactions with the $v_{cut} = 10^{-2}$ setting before stopping (which means v_{cut} has to be lowered for a reliable estimation of the shape of the travelled distance histogram). The ratio of 99% distance to 99.9% distance is also plotted (dark and light blue lines). This ratio is within 10% of 1, i.e., 0.1% of muons travel less than 10% farther than 1% of muons.
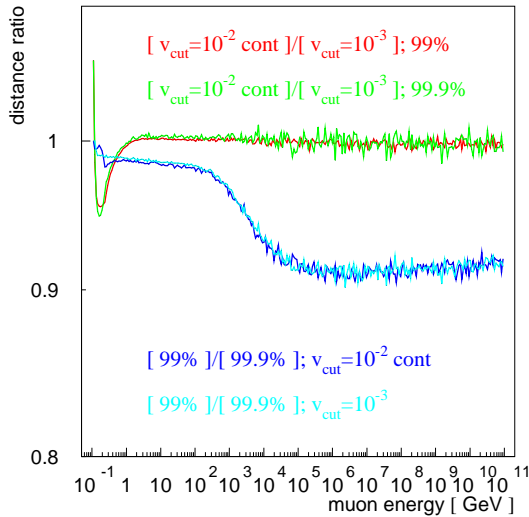
Figure 2.7: Comparison between different surviving fraction and MMC configuration settings
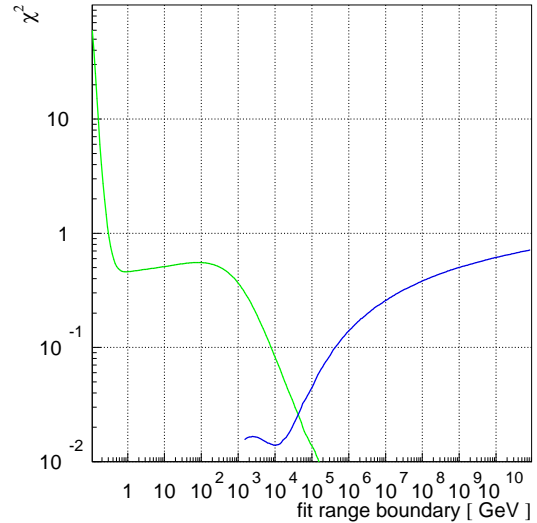
Figure 2.8: χ^2 of the fit as a function of fit boundaries

The value $v_{cut} = 10^{-3}$ with no *cont* setting, used to determine the maximum range of the 99.9% of the muons, was chosen for the estimate of the function $E_{cut}(x)$. The function

$$x_f = \log(1 + E_i \cdot b/a)/b,$$

which is a solution to the equation represented by the usual approximation to the energy losses: $dE/dx = a + bE$, was fitted to $E_{cut}(x)$. In Figure 2.8 the χ^2 of the fit is plotted as function of the lower (green) and upper (blue) boundaries of the fitted energy range. Using the same argument as in Chapter 3.7 the lower limit is chosen at just below 1 GeV while the upper limit was left at 10^{11} GeV. As seen from the plot, raising the lower boundary to as high as 400 GeV would not lower the χ^2 of the fit (and the root mean square of the deviation from it), so the lower boundary was left at 1 GeV for generality of the result. The fit is displayed in Figure 2.9 and the deviation of the actual x_f from the fit is shown on Figure 2.10. The maximum deviation is less than 20%, which can be accounted for by lowering a and b by 20%. Therefore, the final values used in CORSIKA and "ucr"

for the function

$$E_{cut}(x) = (e^{bx} - 1)a/b$$

are $\quad a = 0.212/1.2 \; \dfrac{\text{GeV}}{\text{mwe}} \quad$ and $\quad b = 0.251 \cdot 10^{-3}/1.2 \; \dfrac{1}{\text{mwe}}.$

The distances obtained with these values for four different muon energies are shown by red solid lines in Figure 2.5. The distances obtained with values of a and b not containing the 20% correction are shown with green dashed lines.
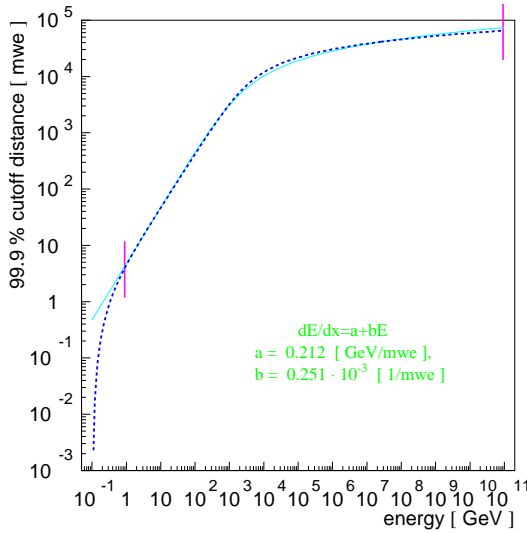
Figure 2.9: Fit to the $E_{cut}(x)$
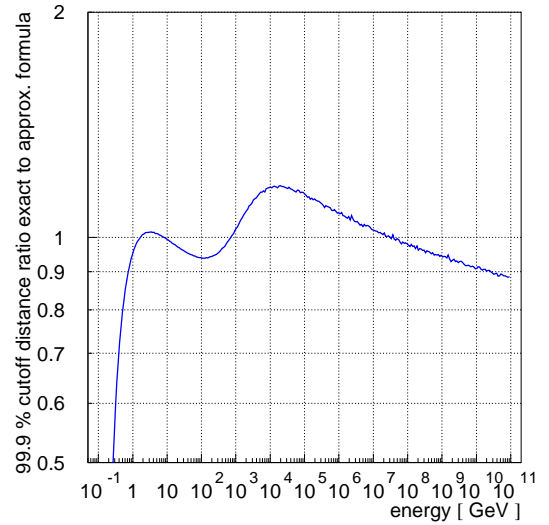
Figure 2.10: Deviation of the $E_{cut}(x)$ from the fit

To determine the fraction ν of the energy threshold of primaries ($E_{low,pri}$) above which 99% or 99.9% of muons are produced (Figure 2.11), more than 10^6 showers were generated for AMANDA-II with $E_{low,pri} = E_{low,\mu}$ from 1 GeV to 10^{11} GeV. The number of simulated muons is shown on Figure 2.13 with a black dashed line (scale to the right of the plot). This number normalized to 10^6 showers is shown in red. The fractions $\nu(99\%)$ and $\nu(99.9\%)$ are shown by green-dotted and blue-solid lines, respectively. For $E_{low,pri}$ for which less than 100 muons were generated, the energy of the second lowest energy muon is used to determine the 99% fraction, same
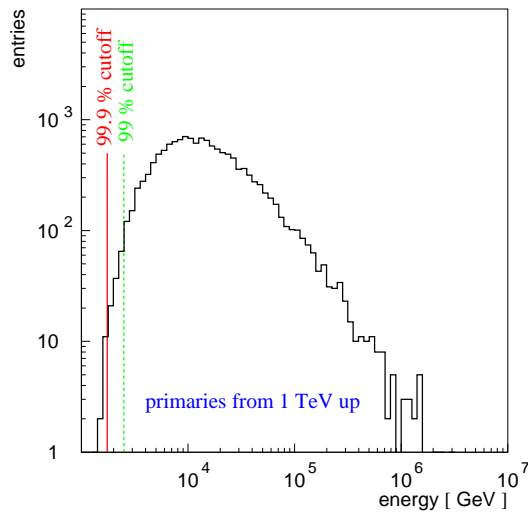
Figure 2.11: Distribution of primaries that produce muons with energies higher than 1 TeV
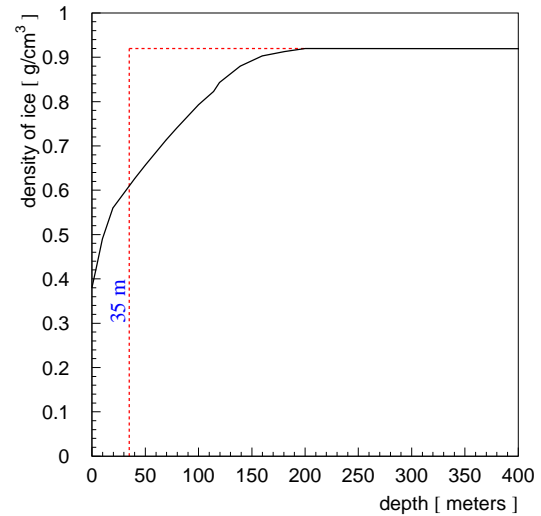
Figure 2.12: Ice density profile correction

for $E_{low,pri}$ for which less than 1000 muons were generated, used to determine the 99.9% fraction. The lowest ratios were found to be

$$\nu_{cut}(99\%) = 2.06 \quad \text{and} \quad \nu_{cut}(99.9\%) = 1.58.$$

These ratios can be used to determine the value of the first argument to "ERANGE" in the INPUTS file once the muon energy threshold ($E_{low,\mu}$) has been set by the first argument to the "ECUTS" flag.

It is also possible to use different energy thresholds (E_{low}) for different primaries (i.e., proportional to the atomic weight of the primaries). As can be deduced from Figure 2.14, 99.9% of muons above $E_{low,\mu} = 238$ GeV are produced by primaries with energies above $E_{low,pri} = 1.58 E_{low,\mu} A$, where A is the atomic weight of the primary. Figures 2.15 and 2.16 show the ratio $E_{low,pri}/E_{low,\mu} A$ for He and Fe. The lowest recorded values of $E_{low,pri}/(A E_{low,\mu})$ for He and Fe are 1.51 and 1.41, respectively, for the 99.9% ratio. These values are lower than the 1.58 chosen for
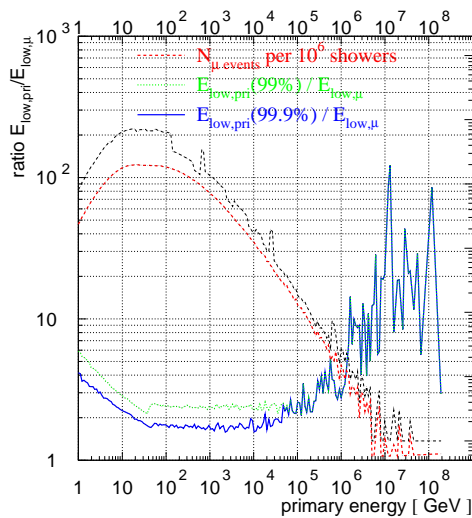
Figure 2.13: Ratio of the primary (H...Fe) to the main muon energies
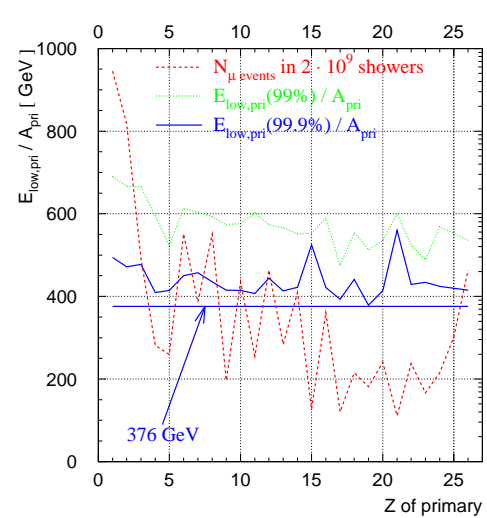
Figure 2.14: Ratio of the primary to muon energies per A for all elements
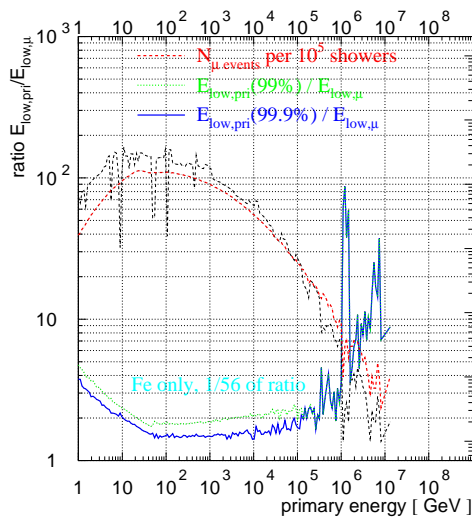
Figure 2.15: Ratio of the primary to muon energies for Fe
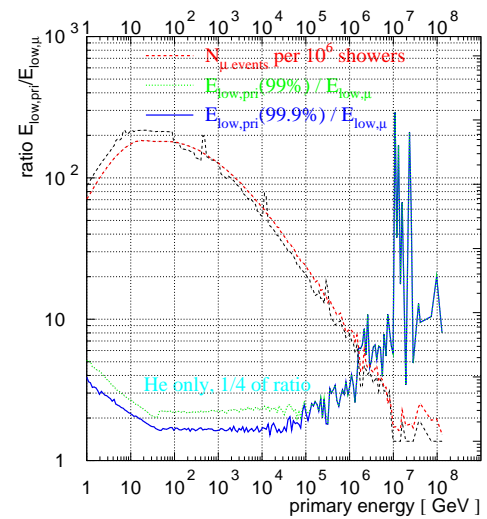
Figure 2.16: Ratio of the primary to muon energies for He

the mixture of primaries. For He, most values are above 1.58 with only two below (1.51 and 1.57).

Values of the ratio for Fe are consistently lower than 1.58. However, the number of muons produced

by Fe (and other primaries from Li to Mn) above 238 GeV is nearly two orders of magnitude smaller

(it amounts to only 3.6%) than those produced by H and He. Therefore, having merely 99% ratios

above 1.58 (1.80 for He and 1.65 for Fe) should be sufficient to maintain the overall ratio above

1.58 for the mixture of primaries when energy cutoffs of primaries are chosen proportional to their

atomic weight (just as when energy cutoffs of different primaries are kept the same).

In the above plots low statistics at high energies do not allow one to determine the 99.9%

ratio reliably for energies higher than 20 TeV. Extrapolating from the lower energy region, however,

it seems that it never gets below 1.58, since the ratio appears to be constant or even rising (for Fe,

see Figure 2.15) with energy.

To choose energy thresholds proportional to the atomic weight of the primaries, specify

"SPRIC T" in the INPUTS file. Doing so reduces *fluxsum*,

$$\sum_A \int_{E_{low}(A)} \Phi_A(E) dE \,,$$

from 0.793 m^{-2}sr^{-1}s^{-1} to 0.359 m^{-2}sr^{-1}s^{-1} (for energy threshold for primaries of 376 GeV),

increasing the lifetime of Monte Carlo files by a factor of 2.2.

2.5 Density depth correction

Due to the lower density of ice packed with air bubbles in the first 200 meters below the

surface, muons lose less energy while propagating down than with the constant ice density depth

profile [33]. To account for this, the exact density profile (Figure 2.12) is approximated by a constant

density profile starting 35 meters below the surface (represented in Figure 2.12 by red dashed lines)

so that the area under both the actual and artificial profiles is the same.

The muon cross sections in a medium are mostly proportional to the density multiplied

by the traveled distance (i.e., mass overburden), with two exceptions. First, the density correction

and dielectric suppression effects have more complicated density dependence, but are generally

very small (below 1%). Second, decay probability is proportional only to the distance (not mass overburden), but is quite small for the interesting muons traveling through 35 m/$\cos\theta$ of ice, because these muons still have about 1.5 km/$\cos\theta$ of ice to travel through to reach the detector, i.e., they must have quite high energy, thus suppressing the decay probability (which is inversly proportional to energy). Neglecting these effects, a muon traveling through a 200 m ice layer with a measured density profile is equivalent to the muon traveling through a 165 m artificial ice layer with constant density profile.

In the above argument the surface of ice was assumed flat in the CORSIKA coordinate system. This is a good approximation, because the muon traveling through $h = 35$ m of ice at the maximum in the CORSIKA frame angle of $\theta_{max} = 88.67°$ goes only $\delta x = h\tan\theta = 1.5$ km away from the point where it enters the ice, and deviation of the surface of ice from flat at that distance is only $R(\cos\alpha - 1) \approx R\alpha^2/2 = \delta x^2/2R = 18$ cm. To make the treatment precise, after reaching the ice surface, muons are transported to the spherical subsurface 35 m below the ice surface and then through the rest of ice (with uniform density) to the detector.

2.6   Discussion of optimizations

Taking for the density-corrected AMANDA-II center depth a value of $h = 1730 - 35 = 1695$ m, ice density $\rho = 0.917$ g/cm^3, and effective dimensions of AMANDA-II $r = 400$ m and $l = 800$ m, one gets for the muon energy threshold $E_{low} = E_{cut}(\rho\cdot(h-l/2)) = E_{cut}(1188$ mwe$) = 238$ GeV. The corresponding value of the energy threshold of the primaries is 490 GeV for 99% of muons recorded and 376 GeV for 99.9% of muons recorded. If instead of the dimensions of the

effective detector cylinder the z-coordinate[2] of the shallowest OM in AMANDA-B10[3] of 231.5 m

is used (also usually used to estimate geometrical dimensions of AMANDA-II), one gets $E_{low} =$

$E_{cut}(1342\ \text{mwe}) = 273$ GeV for muons and 563 GeV (99%) or 432 GeV (99.9%) for primaries.

It could be possible to further raise these numbers if the lowest energy of muons at which they

generate light, which can be recorded by the detector, were known. For the calculation above, it is

assumed to be close to the rest mass of the muon, since for the muon to generate Cherenkov light

its energy can be as low as $\gtrsim 160$ MeV. To summarize, the suggested energy cuts are presented in

Table 2.2.

Table 2.2: AMANDA-II-optimized CORSIKA energy cuts

400 m above the detector center		
fraction	E_{low} for muons	E_{low} for primaries
99%	238 GeV	490 GeV
99.9%	238 GeV	376 GeV
231.5 m above the detector center		
fraction	E_{low} for muons	E_{low} for primaries
99%	273 GeV	563 GeV
99.9%	273 GeV	432 GeV

Execution time and file size (for 10^5 primaries on a 1 GHz computer) are summarized in

Table 2.3.

A run with 10^5 primaries with $E_{low,pri} = 376$ GeV corresponds to 0.0266 seconds of

lifetime of the detector with dimensions $l = 800$ m and $r = 400$ m. Using the angle-dependent

energy cut for primaries accelerates the program by a factor of 3. If additionally the option "-

cutfe=[E_{low}]" is used with "ucr", and only primaries and muons are saved, only 20% of disk space

is used compared to the run with no such cuts. Setting the primary cutoff to $E_{low} = 563$ GeV

---

[2]As measured upward from the center of AMANDA-II, which is defined to be 1730 m below the ice surface.

[3]A part of AMANDA-II, which consists of only 10 strings, see Figure 1.4.

Table 2.3: Comparison of execution time and file size for LOCUT T/F

settings	LOCUT F	LOCUT T
time	55 min	18 min
size	131 Kb	97 Kb
size (only muons)	113 Kb	84 Kb
after "ucr" with "-cutfe=[E_{low}]"		
size	42 Kb	42 Kb
size (only muons)	24 Kb	24 Kb

increases the lifetime of the above run to 0.0527 seconds (with no change in execution time).

2.7 Geometrical area optimization

To determine the optimal dimensions of the cylinder around the detector to be used for the background muon simulation, $2 \cdot 10^{10}$ primaries with energies above $E_{low,pri} = 376$ GeV (muon energy cutoff at $E_{low,\mu} = 273$ GeV) were generated with CORSIKA for the detector with dimensions 800 m $\cdot$ 400 m (length $\cdot$ radius). The corresponding detector lifetime is 1.5 hours. AMANDA-II background simulation ("mass01v002" with mam ice model) produced 287346 triggers. The fraction η of the number of events with tracks, which produce hits during these events, left outside of the cylinder around the detector was calculated for different dimensions of this cylinder. This fraction is plotted on Figure 2.17 as a function of radius and length. The blue contours correspond to $\eta = 10^{-1}$ to 10^{-5}. The green contours correspond to the constant *areasum*

$$\int\limits_0^{\pi/2} (\pi r^2 \cdot \cos\theta + l \cdot 2r \cdot \sin\theta) \cdot d\Omega = \pi^2 r(r+l)$$

(in km^{2}sr). For each choice of η, one should select cylinder dimensions which minimize the *area-sum*. The lowest values of η appear to lie in the four corners of the plot. The plot is symmetrical around $l = 0$ ($-r$ is the same as r). A positive value of the detector length assumes a fixed bottom

at -400 m, and a negative value of the detector length assumes a fixed top at 400 m. Therefore the actual number of tracks outside of the cylinder with chosen dimensions is 1 to 2 times larger than the contour value in the plot. If a track misses both the top and bottom parts for some fixed radius, it misses the whole detector with that radius; however, the track could be contained between the value of the used radius and the maximum radius of 400 m.
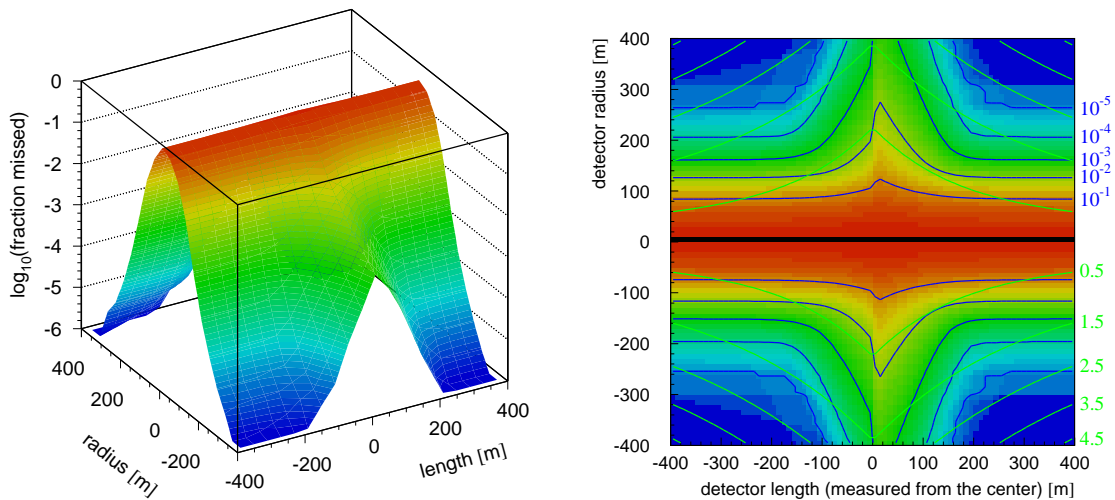
Figure 2.17: Fraction of the events left outside of the detector cylinder

For each fixed fraction *areasum* was minimized. The length and radius which minimize it are plotted as a function of the fraction η in Figure 2.18. The values of length and radius are matched values for each fraction and each part of the detector (top and bottom). Values $l_t = 230$ m and $r = 290$ m for the top part and $l_b = 240$ m and $r = 300$ m for the bottom part of the detector both correspond to no more than $1.5 \cdot 10^{-5}$ of tracks which missed the cylinder of the detector; recalculating for $l = 480$ m and $r = 300$ m of the whole detector (both top and bottom parts) one gets $1.7 \cdot 10^{-5}$ of tracks missed. It is convenient to use values $l = 600$ and $r = 300$ (which correspond to fraction $1.3 \cdot 10^{-5}$) instead, since they are compatible (ratio $l/d = l/2r$ is the same)
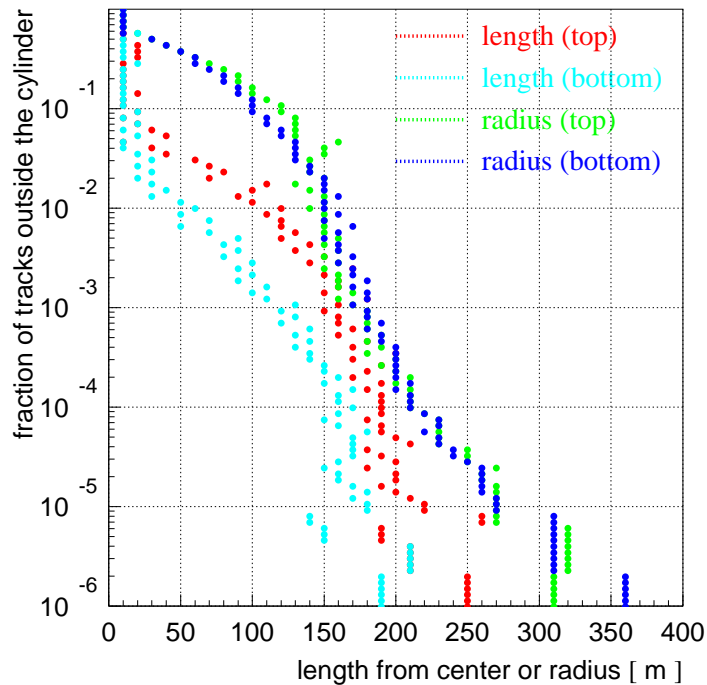
Figure 2.18: Optimal dimensions of the detector cylinder for background muon simulation

with settings $l = 800$ and $r = 400$ used by the rest of the AMANDA-II simulation (CORSIKA files are the same before randomization; *areasum* only depends weakly on l, changing by 15% when replacing 480 m with 600 m). Using these new settings (as compared to the default settings of $l = 800$ and $r = 400$) increases the lifetime of each run by a factor of 1.8 at the cost of increasing the fraction of missed tracks by one order of magnitude.

Figures 2.19 and 2.20 show the zenith angle and energy distributions of primaries at the trigger level. The highest value of the zenith angle is 83.8 degrees, at which the deviation of the surface of the Earth from flat is only 0.12%, i.e., the flat approximation is clearly acceptable (the curved surface is used for simulated data in this work nevertheless). The energy spectrum shows a threshold at just above 600 GeV. A cutoff at high energies (at just above 10^7 GeV) is due to the
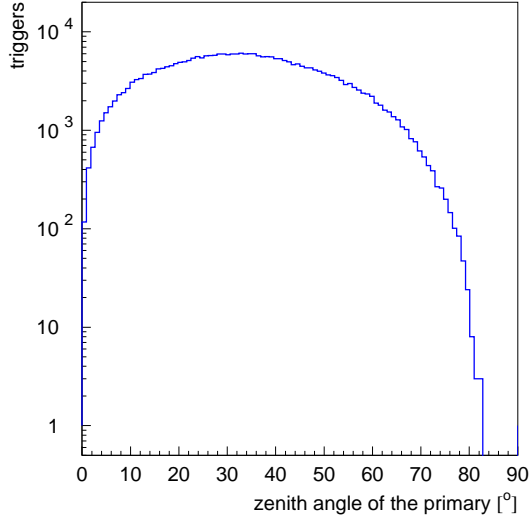
Figure 2.19: Zenith angle distribution of primaries at the trigger level
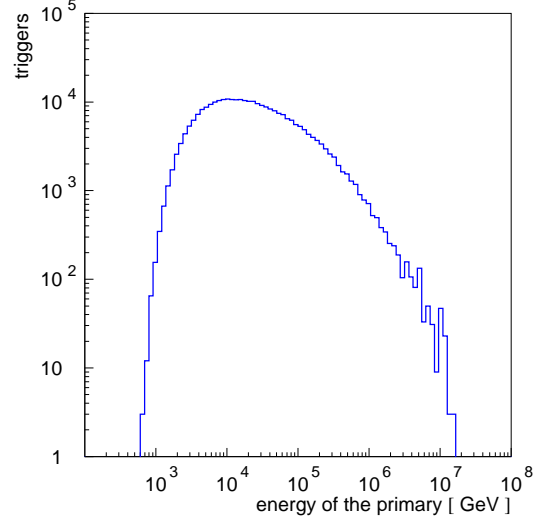
Figure 2.20: Energy distribution of primaries at the trigger level

energy spectrum of primaries falling fast with energy.

All events in Figure 2.17 with primaries (shower cores) missing the cylinder with large dimensions (e.g., $l = 600\,\text{m} \cdot d = 600\,\text{m}$) have at least one muon (Figure 2.21) passing much closer to the detector than its shower core. However, even if the coordinates of the highest energy muon are randomized inside the cylinder projection instead of those of the shower core, some events will still miss the smaller cylinder (with the dimensions given above), with the main contribution to the trigger coming from a smaller energy muon which passes much closer to the detector (Figure 2.22).

2.8   Energy cut optimizations

To determine the lowest energy of a primary which can produce a muon that triggers the detector, the fraction $v(E)$ of such primaries with energies below some energy E was plotted as a function of E (Figure 2.24). The fraction $v(E)$ shows a cutoff behavior and was fit with the 3-parameter function $f(E) = (a(E - E_{cut}))^b$. Table 2.4 summarizes results of an extrapolation of
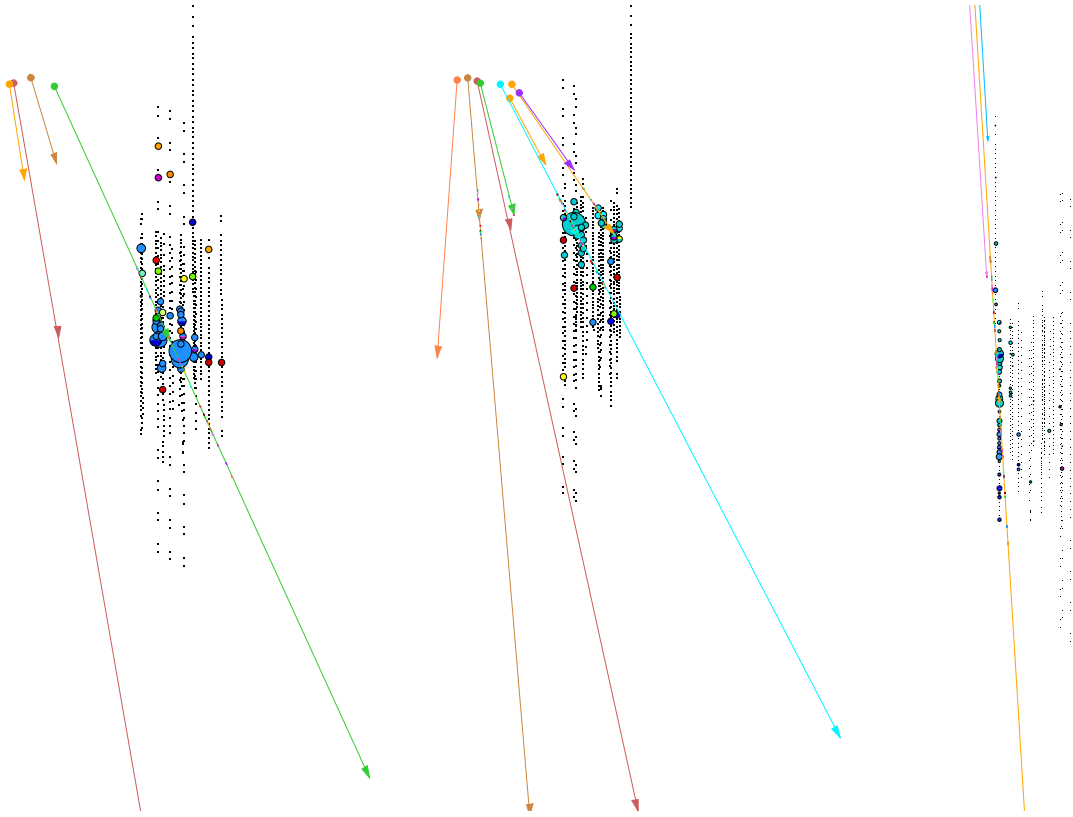
The size of the circles around OMs signifies the signal amplitude in those OMs, the color shows signal arrival time: blue is earlier, red is later

Figure 2.21: Event with shower core outside the cylinder with dimensions $l = 600$ m $\cdot$ $d = 600$ m

Figure 2.22: Event with highest energy muon outside the cylinder with dimensions $l = 600$ m $\cdot$ $d = 600$ m

Figure 2.23: Contribution from low energy muon to trigger condition

the fit to fractions 10^{-5}, 10^{-6}, and 10^{-7}.

Table 2.4: Primary energy cutoff

ice model	10^{-5}	10^{-6}	10^{-7}
stdkurt	676 GeV	622 GeV	600 GeV
mam	711 GeV	625 GeV	568 GeV

If energy thresholds of primaries are chosen to be proportional to the atomic weight A, the energy threshold divided by A must be evaluated. It is essentially the same (shown in Table 2.5)
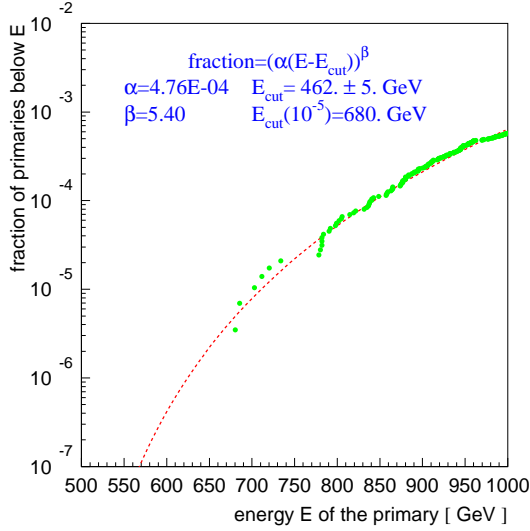
Figure 2.24: Primary energy cutoff (using mam ice model)
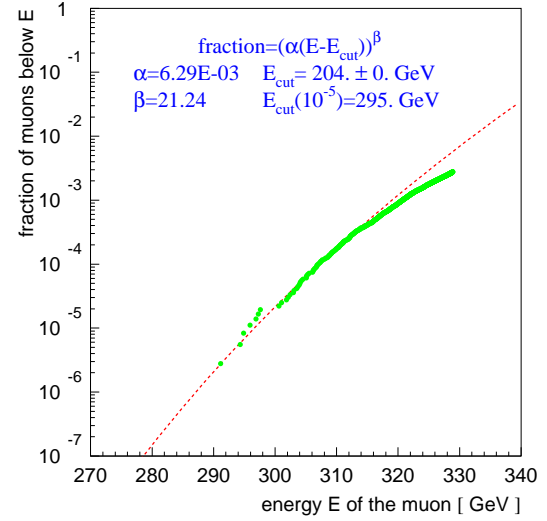
Figure 2.25: Muon energy cutoff (using mam ice model)

as the constant (for all A) energy threshold values of Table 2.4. To minimize $E_{low,\mu}$, energies of all muons producing secondary showers within the active volume of the AMANDA-II detector (chosen here as a cylinder with $l = 800$ m $\cdot$ $d = 800$ m) were translated into the energies that they would need to have to reach the same depth going straight down. The minimum (10^{-6} fraction) $E_{low,\mu}$ energy is 287 GeV (inferred from Figure 2.25), independent of the ice model (Table 2.5). Assuming $E_{low,\mu} = 287$ GeV, energies of all primaries were multiplied by $E_{low,\mu}/(A E_{cut,\mu}(x))$ to determine $E_{low,pri}$. The 10^{-6} fraction is achieved with 498 GeV and 578 GeV for the mam and stdkurt[4] ice models respectively (Table 2.5).

Table 2.5: Primary-weight dependent energy cutoffs, 10^{-6} fractions

ice model	$E_{cutoff,pri}/A$	$E_{low,\mu}$	$E_{low,pri}/A$
stdkurt	631 GeV	287 GeV	499 GeV
mam	624 GeV	287 GeV	578 GeV

---

[4]A brief description of the ice models used in this work is provided in Appendix E.1.

The ratios of $E_{low,pri}/E_{low,\mu}$ are 1.75 for stdkurt and 2.02 for mam ice models. These numbers are greater than the 99.9% ratio suggested in the Section 2.4. Since they differ considerably for different ice models, a safe choice would be to use the value 1.58 from the Section 2.4 (which is independent of ice models). Using $E_{low,\mu} = 287$ GeV one gets $E_{low,pri}/A = 453$ GeV. This value is considerably lower than $E_{cutoff,pri}/A = 624$ GeV of Table 2.5.

A more precise calculation of the energy threshold of muons presented in Table 2.6 (also dependent on ice model) considers only muons which produce photons (or secondary showers which produce photons) which hit detector OMs within the trigger window. The cutoff energies are given for three cases: (1) all OMs are considered, (2) only OMs with z-coordinate below 400 m are considered, and (3) only OMs with z-coordinate below 231.5 m are considered. In the first case muons with energies as low as 242 GeV caused OM hits (second OM on string 17 in Figure 2.23), which is just above the threshold used (238 GeV), chosen with only OMs below 400 m in mind.

Table 2.6: Energy thresholds for muons producing light in the active volume of the AMANDA-II detector

ice model	below 231.5 m	below 400 m	all hits
10^{-5} values			
stdkurt	335 GeV	307 GeV	246 GeV
mam	348 GeV	322 GeV	247 GeV
lowest recorded (approx. 10^{-6}) values			
stdkurt	322 GeV	287 GeV	239 GeV
mam	338 GeV	311 GeV	242 GeV
$E_{low,\mu}$, 10^{-6} values			
stdkurt	298 GeV	279 GeV	234 GeV
mam	312 GeV	305 GeV	227 GeV

The cutoff of $E_{low,\mu} = 273$ GeV introduced in Section 2.6 is clearly acceptable as long as only OMs below 400 m are taken into account. If string 17 or uppermost OMs on strings 11-13

are to be included[5] in the analysis, this setting is no longer sufficient and has to be decreased to 227 GeV.

It is possible to specify the ratio $E_{low,pri}/E_{low,\mu}$ independently of the primary energy threshold as a second parameter to the "LOCUT T 1.58" flag in the INPUTS file. Settings recommended for the AMANDA-II background simulation are $E_{cutoff,pri}/A = 600$ GeV, $E_{low,\mu} = 273$ GeV, LOCUT(2)=1.58, cylinder length=600 m, radius=300 m, and $l/d = 1$. These will result in less than 10^{-5} of triggered events unaccounted for (about 10^{-6} with $l = 800 \cdot r = 400$, which was chosen for simulated data of this work). The lifetime of a run with 10^6 primaries is 2.369 seconds.

Due to the angle-dependent energy threshold of primaries ($E_{low,pri}$, set by "LOCUT T 1.58"), CORSIKA execution time per second of generated lifetime depends only weakly on the energy threshold of primaries ($E_{cutoff,pri}$), which can therefore be further lowered below the recommended value of 600 GeV. Table 2.7 summarizes the execution time and lifetime of a CORSIKA run with 10^5 primaries.

Table 2.7: Execution speed and lifetime of CORSIKA runs

$E_{cutoff,pri}$	600 GeV	500 GeV	432 GeV
execution time, s	1233	1080	866
lifetime, s	0.2014	0.1464	0.1133
ratio (exe/life)	6125	7375	7644

---

[5]String 17 and parts of strings 11-13 contain OMs at depths significantly shallower than the majority in the detector, and are excluded for some types of analyses.

Chapter 3

Muon Propagation through Ice

- Easier done than said -

3.1 Muon Monte Carlo: a new high-precision tool for muon propagation through matter

An accurate simulation of the propagation of muons through large amounts of matter is needed for the analysis of data produced by muon/neutrino underground experiments. A muon may sustain hundreds of interactions before it is detected by the experiment. Since a small uncertainty introduced hundreds of times may lead to sizable errors, requirements on the precision of the muon propagation code are very stringent. A new tool for propagating muon and tau charged leptons through matter that is believed to meet these requirements is presented here. The latest formulae available for the interaction cross sections were used and the reduction of calculational errors to a minimum was the top priority. The tool is a very versatile program written in an object-oriented language environment (Java). It supports many different optimization (parametrization) levels. The

fully parametrized version is as fast or even faster than the counterparts. On the other hand, the slowest version of the program, which does not make use of parameterizations, is fast enough for many tasks if queuing or distributed environments with large numbers of connected computers are used. In this chapter, an overview of the program is given and some results of its application are discussed.

3.2 Introduction

In order to observe atmospheric and cosmic neutrinos with a large underground detector (e.g., AMANDA [12]), one needs to isolate the neutrino signal from the 3-5 orders of magnitude larger signal from the background of atmospheric muons. Methods that do this have been designed and proven viable [24]. In order to prove that these methods work and to derive indirect results such as the spectral index of atmospheric muons, one needs to compare data to the results of the computer simulation. Such a simulation normally contains three parts: propagation of the measured flux of the cosmic particles from the top of the atmosphere down to the surface of the ground (ice, water); propagation of the atmospheric muons from the surface down to and through the detector; and generation of the Cerenkov photons generated by the muons in the vicinity of the detector and their interaction with the detector components. The first part is normally called *generator*, since it generates muon flux at the ground surface; the second is *propagator*; and the third simulates the detector interaction with the passing muons. Mainly two generators were used so far (by AMANDA): basiev [34] and CORSIKA [23]. Results and methods of using CORSIKA as a generator in a neutrino detector (AMANDA-II) were discussed in the previous chapter (see also [15]). Several muon propagation Monte Carlo programs were used with different degrees of success as propagators. Some

are not suited for applications which require the code to propagate muons in a large energy range

(e.g., mudedx, a.k.a. LOH), and the others seem to work in only some of the interesting energy

range ($E > 1$ TeV, propmu, a.k.a. LIP) [35]. Most of the programs use cross section formulae

whose precision has been improved since their time of writing. For some applications, one would

also like to use the code for the propagation of muons that contain $100 - 1000$ interactions along

their track, so the precision of each step should be sufficiently high and the computational errors

should accumulate as slowly as possible. Significant discrepancies between the muon propagation

codes tested in this work were observed, and are believed to be mostly due to algorithm errors (see

Appendix D). This motivated writing of a new computer program (Muon Monte Carlo: MMC [36]),

which minimizes calculational errors, leaving only those uncertainties that come from the imperfect

knowledge of the cross sections.

3.3   Description of the code

The primary design goals of MMC were computational precision and code clarity. The

program is written in Java, since Java is an object-oriented programming language (for best code

readability) and has consistent behavior across many platforms. MMC consists of pieces of code

(classes), each contained in a separate file. These pieces fulfill their separate tasks and are com-

bined in a structured way (Figure 3.1). This simplifies code maintenance and introduction of

changes/corrections to the cross section formulae and is required by our choice of the program-

ming language. It is also very straightforward to "plug" in new cross sections, if necessary. Writing

in an object-oriented language allows several instances of the program to be created and accessed

simultaneously. This is useful for simulating the behavior of the neutrino detectors, where different

conditions apply above, inside, and below the detector.

The code evaluates many cross-section integrals, as well as two tracking integrals. All integral evaluations are done by the Romberg method of the 5th order (by default) [37] with a variable substitution (mostly log-exp). If an upper limit of an integral is an unknown (that depends on a random number), an approximation to that limit is found during normalization integral evaluation, and then refined by the Newton-Raphson method combined with bisection [37].
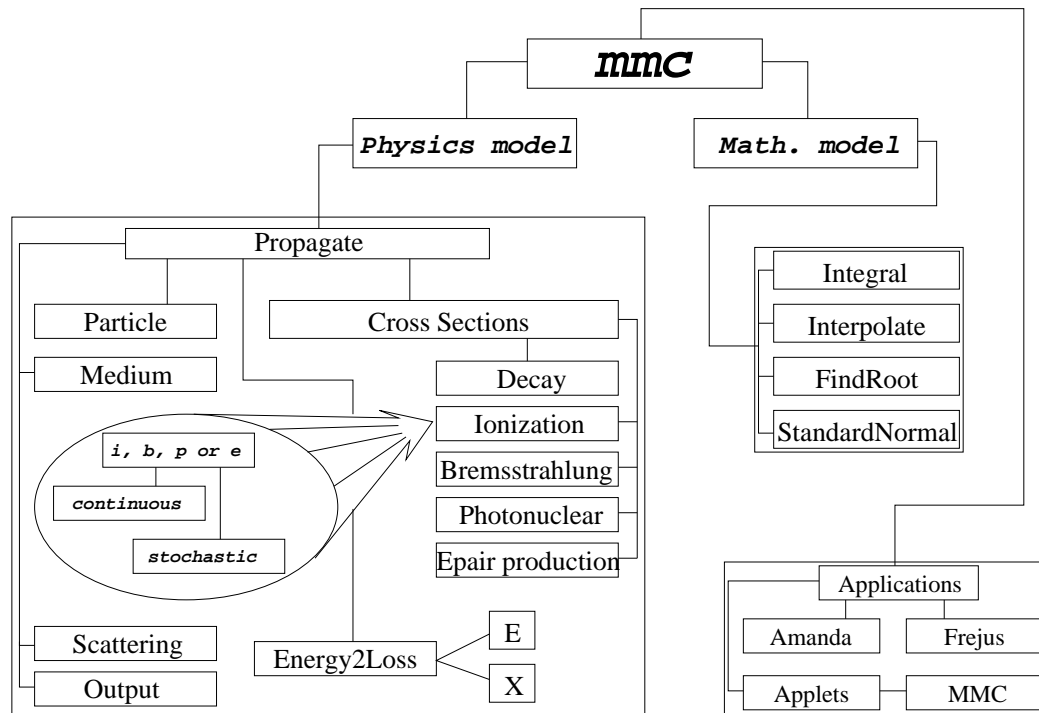
Figure 3.1: MMC structure

Originally, the program was designed to be used in the Massively Parallel Network Computing (SYMPHONY) [38] framework, and therefore computational speed was considered only a secondary issue. However, parametrization and interpolation routines were implemented for all integrals. These are both polynomial and rational function interpolation routines spanned over a vary-

ing number of points (5 by default) [37]. Inverse interpolation is implemented for root finding (i.e.,

when $x(f)$ is interpolated to solve $f(x) = y$). Two-dimensional interpolations are implemented as

two consecutive one-dimensional ones. It is possible to turn parameterizations on or off for each

integral separately at program initialization. The default energy range in which parametrized formu-

lae will work was chosen to be from 105.7 MeV (the muon rest mass) to $E_{big} = 10^{14}$ MeV, and the

program was tested to work with much higher settings of E_{big}. With full optimization (parameteri-

zations) this code is at least as fast or even faster than the other muon propagation codes discussed

in Appendix D.

Generally, as a muon travels through matter, it loses energy due to ionization losses,

bremsstrahlung, photo-nuclear interaction, and pair production. Formulae for the cross sections

were taken from the recent contribution [18] and are summarized in Section 3.10. These formulae

are claimed to be valid to within about 1% in the energy range interesting for this work (up to $\gtrsim$

10 TeV). All of the energy losses have continuous and stochastic components, the division between

which is artificial and is chosen in the program by selecting an energy cut (e_{cut}, also E_{cut}) or a rel-

ative energy loss cut (v_{cut}). In the following, v_{cut} and e_{cut} are considered to be interchangable and

related by $e_{cut} = v_{cut}E$ (even though only one of them is a constant). Ideally, all losses should be

treated stochastically. However, that would bring the number of separate energy loss events to a very

large value, since the probability of such events to occur diverges as $1/E_{lost}$ for the bremsstrahlung

losses, as the lost energy approaches zero, and even faster than that for the other losses. In fact,

the reason this number, while being very large, is not infinite, is the existence of kinematic cutoffs

(larger than some e_0) for all diverging cross sections. A good choice of v_{cut} for the propagation of

atmospheric muons should lie in the range $0.05 - 0.1$ [39] (Section 3.4). For monoenergetic beams

of muons, v_{cut} may have to be chosen to be high as $10^{-3} - 10^{-4}$.

3.3.1 Tracking formulae

Let the continuous part of the energy losses (a sum of all energy losses, integrated from zero to e_{cut}) be described by a function $f(E)$:

$$-\frac{dE}{dx} = f(E).$$

Figure 3.2: Derivation of tracking formulae

The stochastic part of the losses is described by the function $\sigma(E)$, which is a probability for any energy loss event (with lost energy $> e_{cut}$) to occur along a path of 1 cm. Consider the particle path from one interaction to the next consisting of small intervals (Figure 3.2). On each of these small intervals the probability of interaction is $dP(E(x_i)) = \sigma(E(x_i))dx$. It is easy to derive an expression for the final energy after this step as a function of the random number ξ. The probability to completely avoid stochastic processes on an interval $(x_i; x_f)$ and then suffer a catastrophic loss on dx at x_f is

$$(1 - dP(E(x_i))) \cdot ... \cdot (1 - dP(E(x_{f-1}))) \cdot dP(E(x_f))$$

$$= \exp(-dP(E(x_i))) \cdot ... \cdot \exp(-dP(E(x_{f-1}))) \cdot dP(E(x_f))$$

$$= \exp\left(-\int_{E_i}^{E_f} dP(E(x))\right) \cdot dP(E(x_f))$$

$$= d_f \left(-\exp(-\int_{E_i}^{E_f} \frac{\sigma(E)}{-f(E)} \cdot dE) \right) = d(-\xi), \quad \xi \in (0; 1]$$

To find the final energy after each step the above equation is solved for E_f:

$$\int_{E_i}^{E_f} \frac{\sigma(E)}{-f(E)} \cdot dE = -\log(\xi) \quad \text{(energy integral)}.$$

This equation has a solution if

$$\xi > \xi_0 = \exp\left(-\int_{e_{low}}^{E_i} \frac{\sigma(E)}{f(E)} \cdot dE \right).$$

Here e_{low} is a low energy cutoff, below which the muon is considered to be lost. Note that $f(E)$ is always positive due to ionization losses (unless $e_{cut} \approx I(Z)$). The value of $\sigma(E)$ is also always positive because it includes the positive decay probability. If $\xi < \xi_0$, the particle is stopped and its energy is set to e_{low}. The corresponding displacement for all ξ can be found from

$$x_f = x_i - \int_{E_i}^{E_f} \frac{dE}{f(E)} \quad \text{(tracking integral)}.$$

3.3.2   Continuous randomization

It was found that for higher v_{cut} muon spectra are not continuous (Figure 3.3). In fact, there is a large peak (at E_{peak}) that collects all particles that did not suffer stochastic losses followed by the main spectrum distribution separated from the peak by at least the value of $v_{cut} E_{peak}$ (the smallest stochastic loss). The appearance of the peak and its prominence are governed by v_{cut}, co-relation of initial energy and propagation distance, and the binning of the final energy spectrum histogram. In order to be able to approximate the real spectra with even a large v_{cut} and to study the systematic effect at a large v_{cut}, a *continuous randomization* feature was introduced.

For a fixed v_{cut} or e_{cut} a particle is propagated until the algorithm discussed above finds an interaction point, i.e., a point where the particle loses more than the cutoff energy. The average
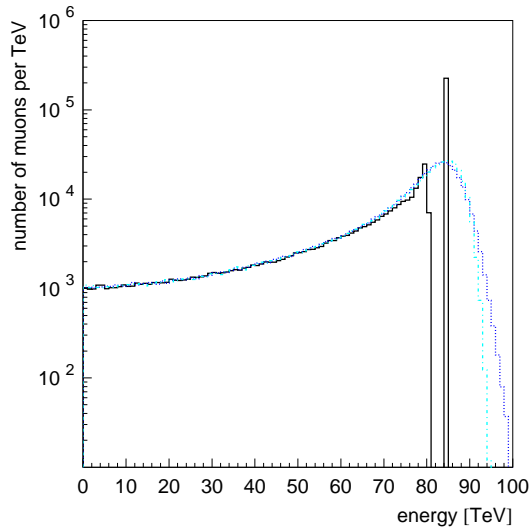
Figure 3.3: Distribution of the final energy of the muons that crossed 300 m of Fréjus Rock with initial energy 100 TeV: $v_{cut} = 0.05$ (solid), $v_{cut} = 10^{-4}$ (dashed-dotted), $v_{cut} = 0.05$ and *cont* option (dotted)
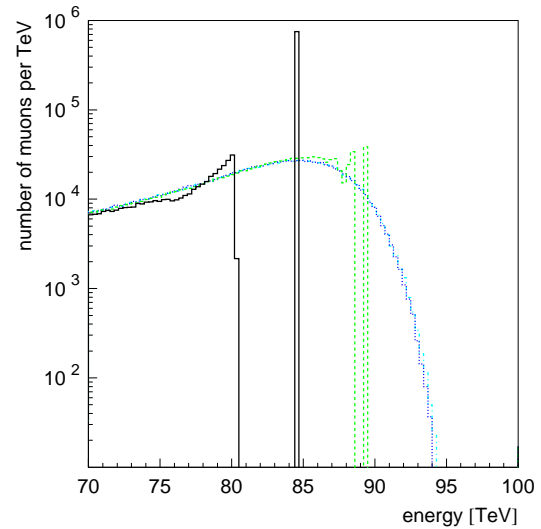
Figure 3.4: A close-up on the Figure 3.3: $v_{cut} = 0.05$ (solid), $v_{cut} = 0.01$ (dashed), $v_{cut} = 10^{-3}$ (dotted), $v_{cut} = 10^{-4}$ (dashed-dotted)
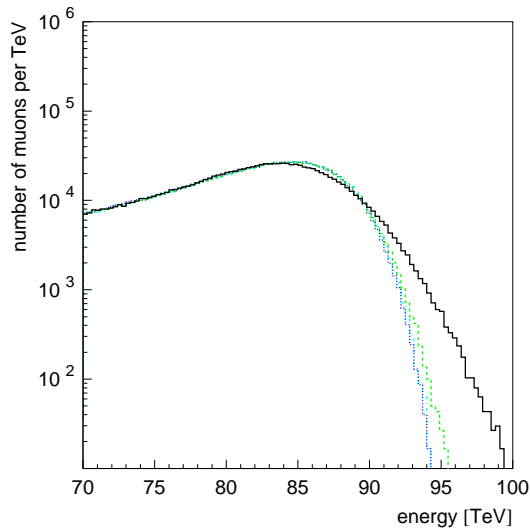
Figure 3.5: Same as in Figure 3.4, but with *cont* option enabled
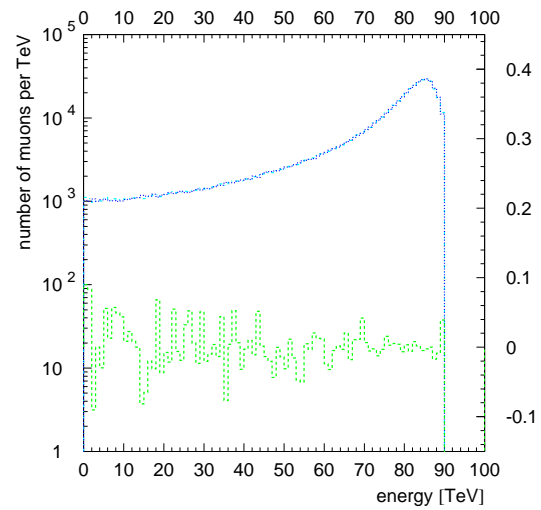
Figure 3.6: Comparison of parametrized (dashed-dotted) with exact (non-parametrized, dotted) versions for $v_{cut} = 0.01$. Also shown is the relative difference of the curves.

value of the energy decrease due to continuous energy losses is evaluated according to the energy integral formula of the previous section. There will be some fluctuations in this energy loss, which are not described by this formula. Let us assume there is a cutoff for all processes at some small $e_0 \ll e_{cut}$. Then the probability $p(e; E)$ for a process with $e_0 < e_{lost} < e_{cut}$ on the distance dx is normalizable to 1. Now choose dx so small that

$$p_0 = \int_{e_0}^{e_{cut}} p(e; E) \, de \cdot dx \ll 1.$$

Then the probability to not have any losses is $1 - p_0$, and the probability to have two or more separate losses is negligible. The standard deviation of the energy loss on dx from the average value

$$< e > = \int_{e_0}^{e_{cut}} e \cdot p(e; E) \, de \cdot dx$$

is then $< (\Delta e)^2 > = < e^2 > - < e >^2$, where

$$< e^2 > = \int_{e_0}^{e_{cut}} e^2 \cdot p(e; E) \, de \cdot dx.$$

If the value of v_{cut} or e_{cut} used for the calculation is sufficiently small, the distance $x_f - x_i$ determined by the energy and tracking integrals is so small that the average energy loss $E_i - E_f$ is also small (as compared to the initial energy E_i). One may therefore assume $p(e; E) \simeq p(e; E_i)$, i.e., the energy loss distributions on the small intervals dx_n that sum up to the $x_f - x_i$, is the same for all intervals. Since the total energy loss $E_i - E_f = \sum e_n$, the central limit theorem can be applied, and the final energy loss distribution will be Gaussian with the average $\Delta E = E_i - E_f$ and width

$$< (\Delta(\Delta E))^2 > = \sum_n \left(< e_n^2 > - < e_n >^2 \right)$$

$$= \sum_n \left[\left(\int_{e_0}^{e_{cut}} e_n^2 \cdot p(e_n; E_i) \, de_n \right) dx_n - \left(\int_{e_0}^{e_{cut}} e_n \cdot p(e_n; E_i) \, de_n \right)^2 dx_n^2 \right]$$

$$\simeq \int_{x_i}^{x_f} dx \cdot \left(\int_{e_0}^{e_{cut}} e^2 \cdot p(e; E(x)) \, de \right) - \int_{x_i}^{x_f} dx \cdot \left(\int_{e_0}^{e_{cut}} e \cdot p(e; E(x)) \, de \right)^2 dx$$

Here E_i was replaced with the average expectation value of energy at x, $E(x)$. As $dx \to 0$, the second term disappears. The lower limit of the integral over e can be replaced with zero, since all of the cross sections diverge slower than $1/e^3$. Then,

$$< (\Delta(\Delta E))^2 > \simeq \int_{x_i}^{x_f} \frac{dE}{-f(E)} \cdot \left(\int_0^{e_{cut}} e^2 \cdot p(e; E) \, de \right).$$

This formula is applicable for small v_{cut}, as seen from the derivation. Energy spectra calculated with *continuous randomization* converge faster than those without (see Figures 3.4 and 3.5).

3.4 Computational and algorithm errors

All cross-section integrals are evaluated to the relative precision of 10^{-6}; the tracking integrals are functions of these, so their precision was set to a larger value of 10^{-5}. To check the precision of interpolation routines, results of running with parameterizations enabled were compared to those with parameterizations disabled. Figure 3.7 shows relative energy losses for ice due to different mechanisms. Decay energy loss is shown here only for comparison and is evaluated by multiplying the probability of decay by the energy of the particle. In the region below 1 GeV bremsstrahlung energy loss has a double cutoff structure. This is due to a difference in the kinematic restrictions for muon interaction with oxygen and hydrogen atoms. A cutoff (for any process) is a complicated structure to parametrize and with only a few parametrization grid points in the cutoff region, interpolation errors $(e_{pa} - e_{np})/e_{pa}$ may become quite high, reaching 100% right below the cutoff, where the interpolation routines give non-zero values, whereas the exact values are zero. But since the energy losses due to either bremsstrahlung, photonuclear process, or pair production are

very small near the cutoff in comparison to the sum of all losses (mostly ionization energy loss), this large relative error results in a much smaller increase of the relative error of the total energy losses (Figure 3.8). Because of that, parametrization errors never exceed $10^{-4} - 10^{-3}$, for the most part being even much smaller ($10^{-6} - 10^{-5}$), as one can estimate from the plot. These errors are much smaller than the uncertainties in the formulae for the cross sections. Now the question arises whether this precision is sufficient to propagate muons with hundreds of interactions along their way. Figure 3.6 is one of the examples that demonstrate that it is sufficient: the final energy distribution did not change after enabling parametrizations. Moreover, different orders of the interpolation algorithm (**g**, corresponding to the number of the grid points over which interpolation is done) were tested (Figure 3.9) and results of propagation with different **g** compared with each other (Figure 3.10). The default value of **g** was chosen to be 5, but can be changed to other acceptable values $3 \leq$ **g** ≤ 6 at the run time.
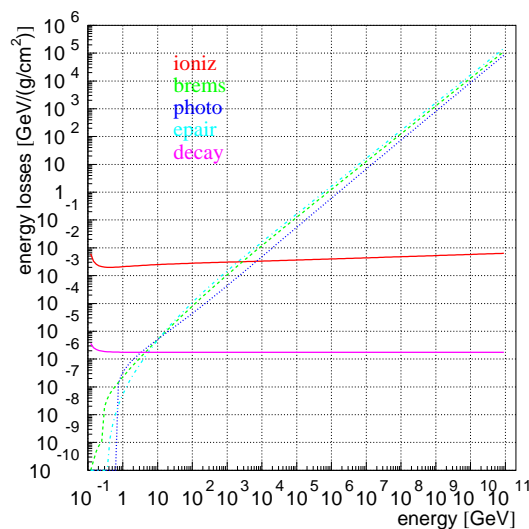
Figure 3.7: Ioniz (upper solid curve), brems (dashed), photo (dotted), epair (dashed-dotted) and decay (lower solid curve) losses in ice
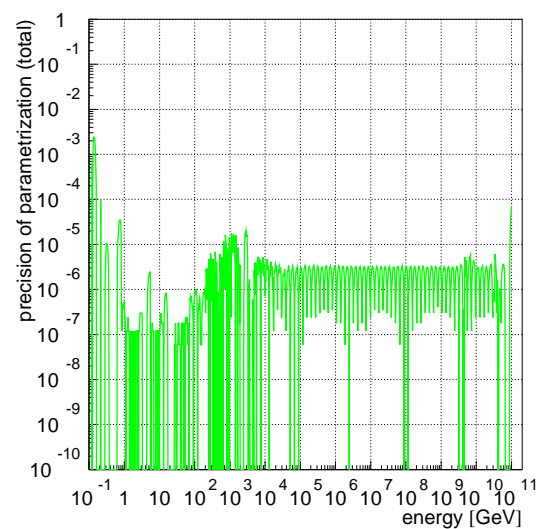
Figure 3.8: Interpolation precision $(e_{pa} - e_{np})/e_{pa}$
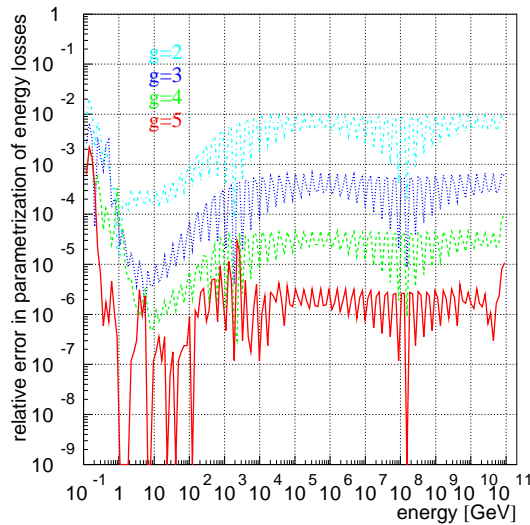
Figure 3.9: Interpolation precision for different orders of the interpolation algorithm
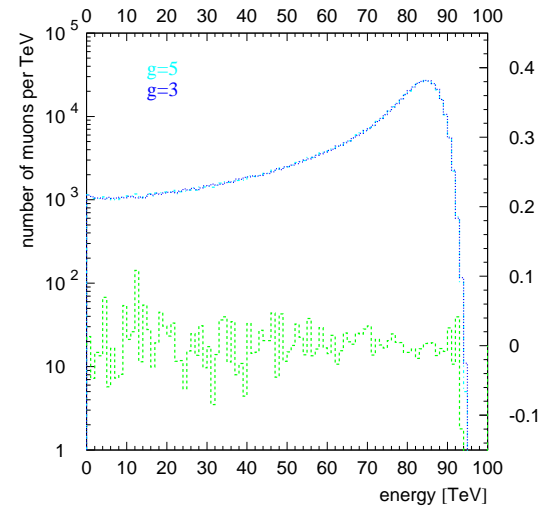
Figure 3.10: Comparison of the result of the propagation for different orders of the interpolation algorithm

MMC has a low energy cutoff e_{low} below which the muon is considered to be lost. By default it is equal to the mass of the muon, but can be changed to any higher value. This cutoff enters the calculation in several places, most notably in the initial evaluation of the energy integral. To determine the random number ξ_0 below which the particle is considered stopped, the energy integral is first evaluated from E_i to e_{low}. It is also used in the parametrization of the energy and tracking integrals, since they are evaluated from this value to E_i and E_f, and then the interpolated value for E_f is subtracted from that for E_i. Figure 3.11 demonstrates the independence of MMC from the value of e_{low}. For the curve with $e_{low} = m_\mu$ integrals are evaluated in the range 105.7 MeV − 100 TeV, i.e., over six orders of magnitude, and they are as precise as those calculated for the curve with e_{low}=10 TeV, with integrals being evaluated over only one order of magnitude.

Figure 3.12 demonstrates the spectra of secondaries (delta electrons, bremsstrahlung photons, excited nuclei, and electron pairs) produced by the muon, whose energy is kept constant at 10
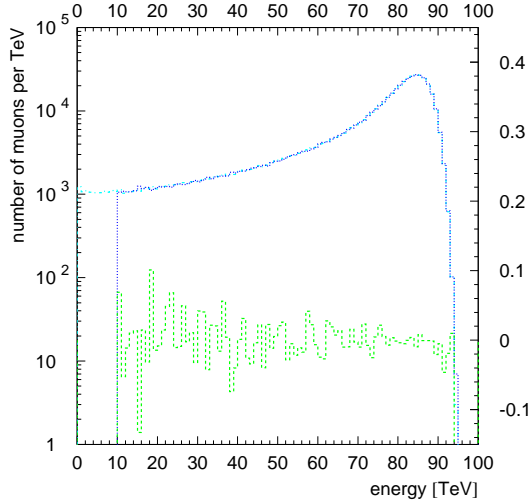
Figure 3.11: Comparison of $e_{low} = m_\mu$ (dotted-dashed) with e_{low}=10 TeV (dotted). Also shown is the relative difference of the curves.
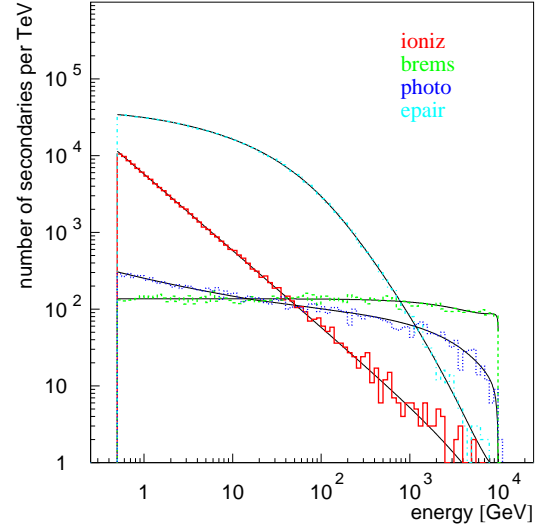
Figure 3.12: Ioniz (upper solid curve), brems (dashed), photo (dotted), epair (dashed-dotted) spectra for E_μ=10 TeV in the Fréjus rock

TeV. The thin lines superimposed on the histograms are the probability functions (roughly cross sections) used in the calculation. They have been corrected to fit the logarithmically binned histograms (multiplied by the size of the bin which is proportional to the abscissa, i.e., the energy). While the agreement is trivial from the Monte Carlo point of view, it demonstrates that the computational algorithm is correct.

Figure 3.13 shows the relative deviation of the average final energy of the $4 \cdot 10^6$ 1 TeV and 100 TeV muons propagated through 100 m of Fréjus Rock[1] with the abscissa setting for v_{cut}, from the final energy obtained with $v_{cut} = 1$. Just like in [39] the distance was chosen small enough so that only a negligible number of muons stop, while large enough so that the muon suffers a large number of stochastic losses (> 10 for $v_{cut} \leq 10^{-3}$). All points should agree with the result for $v_{cut} = 1$, since it should be equal to the integral of all energy losses, and averaging over the energy

[1]A medium with properties similar to that of standard rock (see Table C.2) used for data analysis in the Fréjus experiment [40].

losses for $v_{cut} < 1$ is evaluating such an integral with the Monte Carlo method. There is a visible systematic shift $\lesssim (1 - 2) \cdot 10^{-4}$ (similar for other muon energies), which can be considered as another measure of the algorithm accuracy [39].
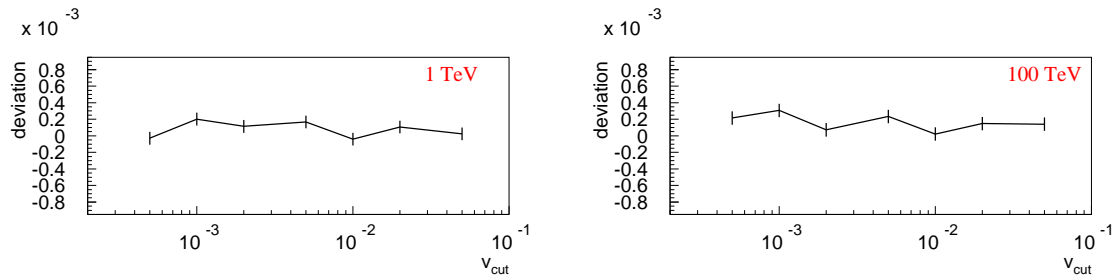
Figure 3.13: Algorithm errors (average energy loss)
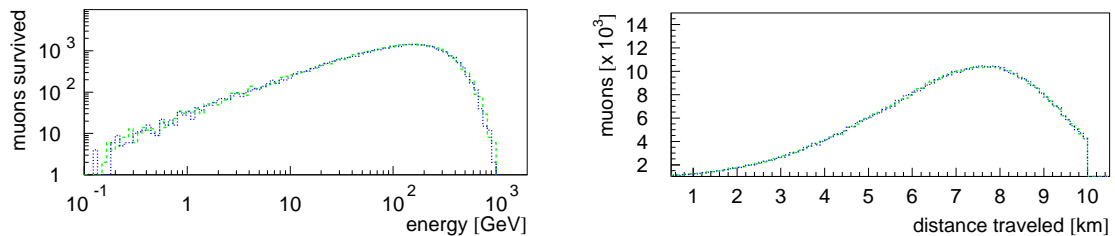
Figure 3.14: 10^6 muons with energy 9 TeV propagated through 10 km of water: regular (dashed) vs. *cont* (dotted)

In the case when almost all muons stop before passing the requested distance (see Figure 3.14), even small algorithm errors may substantially affect survival probabilities. Table 3.1 summarizes the survival probabilities for a monochromatic muon beam of 10^6 muons with three initial energies (1 TeV, 9 TeV, and 10^6 TeV) going through three distances (3 km, 10 km, and 40 km) in water. One should note that these numbers are very sensitive to the cross sections used in the calculation; e.g., for 10^9 GeV muons propagating through 40 km the rates decrease 30% when the default photonuclear cross section is replaced with the ZEUS parametrization (case number four from Section 3.10.3). However, the same set of formulae was used throughout the calculation. The errors of

the values in the table are statistical and are $\lesssim \pm 0.001$. The survival probabilities converge on the

Table 3.1: Survival probabilities

v_{cut}	cont	1 TeV 3 km	9 TeV 10 km	10^6 TeV 40 km
0.2	no	0	0	0.153
0.2	yes	0.010	0.057	0.177
0.05	no	0	0.035	0.143
0.05	yes	0.045	0.039	0.139
0.01	no	0.030	0.037	0.142
0.01	yes	0.034	0.037	0.139
10^{-3}	no	0.034	0.037	0.140
10^{-3}	yes	0.034	0.037	0.135

final value for $v_{cut} \lesssim 0.01$ in the first two columns. Using the *cont* option helped the convergence in

the first column. However, the *cont* values departed from regular values more in the third column.

The relative deviation (3.5%) can be used as an estimate of the *continuous randomization* algorithm

precision (not calculational errors) in this case. One should note, however, that with the number of

interactions $\gtrsim 10^3$ the *continuous randomization* approximation formula was applied $\gtrsim 10^3$ times.

It explains why the value of *cont* version for $v_{cut} = 0.01$ is closer to the converged value of the

regular version than for $v_{cut} = 10^{-3}$.

3.5   Tau propagation

Taus can also be propagated with MMC. It is recommended that the ALLM parametriza-

tion (Section 3.10.8) be selected for photonuclear cross section. Tau propagation is quite different

from muon propagation because the tau lifetime is 7 orders of magnitude shorter than the muon life-

time. While muon decay can be neglected in most cases of muon propagation, it is the main process

to be accounted for in the tau propagation. Figures 3.15 and 3.16 compare tau energy losses with
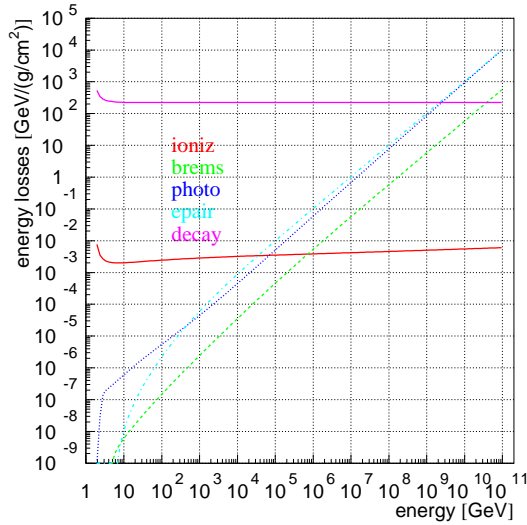
Figure 3.15: Tau energy losses in Fréjus Rock
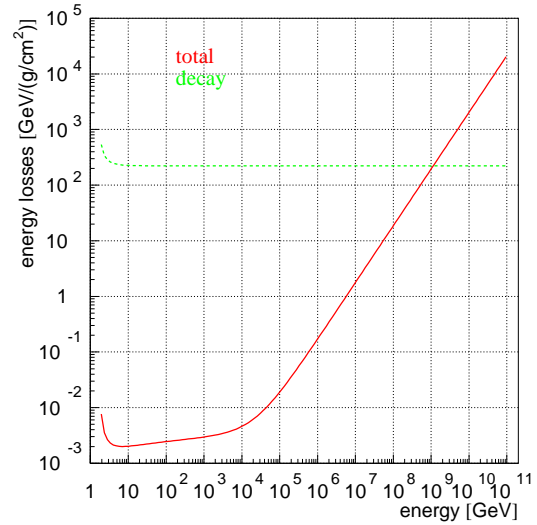
Figure 3.16: Sum of tau energy losses in Fréjus Rock
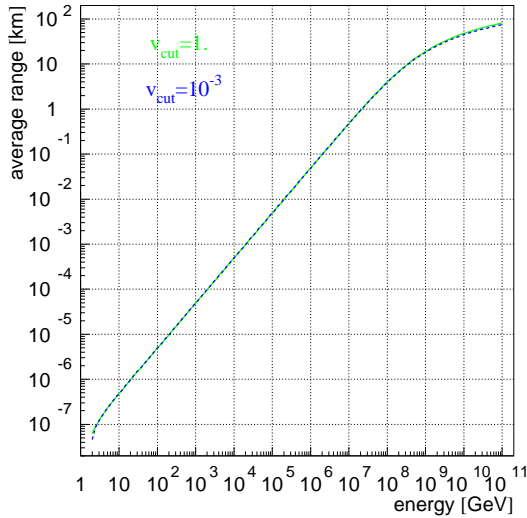
Figure 3.17: Average range of taus propagated through Fréjus Rock
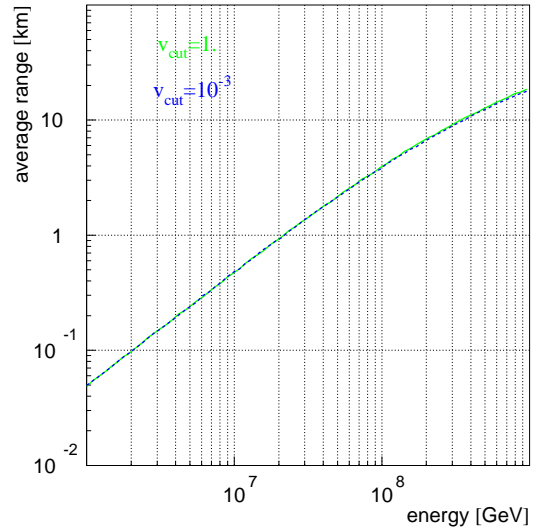
Figure 3.18: Same as in Figure 3.17 for tau energies $10^6 - 10^9$ GeV

losses caused by tau decay (given by $E_\tau/(\rho v_\tau \tau) = m_\tau/(\rho v_\tau \tau_0)$; this is the energy per mwe deposited by decaying taus in a beam propagating though a medium with density ρ). Figures 3.17 and 3.18 compare the average range of taus propagated through Fréjus Rock with $v_{cut} = 1$ (completely continuously) and $v_{cut} = 10^{-3}$ (detailed stochastic treatment). Both treatments produce almost

identical results. Therefore, tau propagation can be treated continuously for all energies unless one needs to obtain spectra of the secondaries created along the tau track.

3.6 Comparison with other propagation codes

Several propagation codes have been compared with MMC. Where possible MMC settings were changed to match those of the other codes. Figures 3.19 and 3.20 compare the results of muon propagation through 300 m of Fréjus Rock with MMC and MUM [39] ($v_{cut} = 10^{-3}$, ZEUS parametrization of the photonuclear cross section).
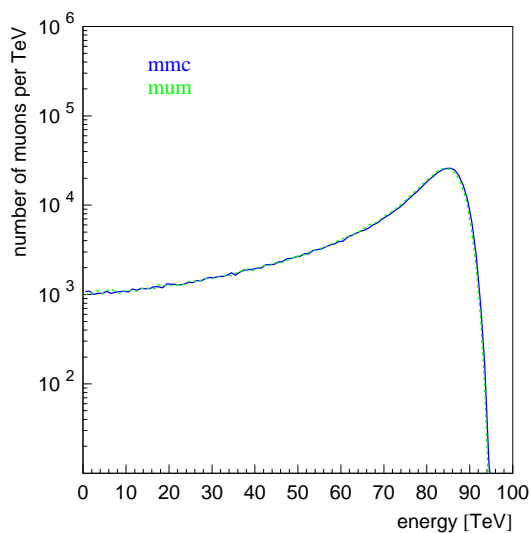
Figure 3.19: Comparison of results of muon propagation through 300 m of Fréjus Rock with MMC and MUM
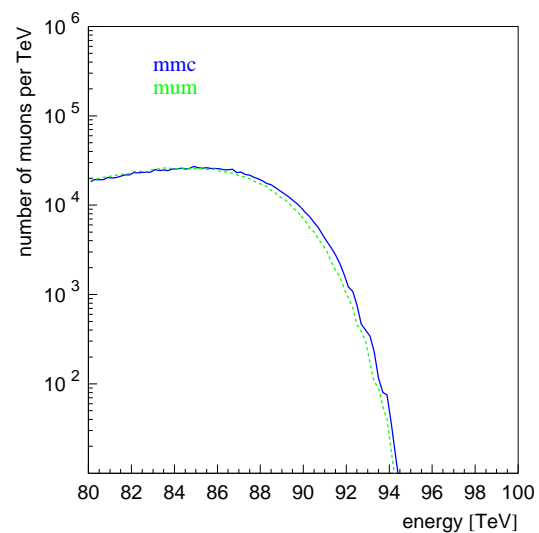
Figure 3.20: Close-up on the end of the distribution in Figure 3.19

Survival probabilities of Table 3.1 were compared with results from [39] in Table 3.2. Survival probabilities are strongly correlated with the distribution of the highest-energy muons in an originally monoenergetic beam. This, in turn, is very sensitive to the algorithm errors and the cross-section implementation used for the calculation.

Table 3.2: Survival probabilities of MMC compared to other codes

v_{cut}	propagation code	1 TeV 3 km	9 TeV 10 km	10^6 TeV 40 km
10^{-3}	MMC (default)	0.034	0.037	0.140
10^{-3}	MMC (ZEUS)	0.034	0.037	0.090
10^{-3}	MUM	0.029	0.030	0.078
10^{-3}	MUSIC	0.033	0.031	0.084
10^{-3}	PROPMU	0.19	0.048	0.044

A detailed comparison between spectra of secondaries produced with MMC, MUM, LOH, and LIP is given in the Appendix D. A definite improvement of MMC over the other codes can be seen in the precision of description of spectra of secondaries and the range of energies over which the propagation code works.

3.7 Energy losses in ice and rock, some general results

The code was incorporated into the Monte Carlo chains of two detectors: Fréjus [40, 41] and AMANDA [35] (also this work). In this section some general results are presented.

The plot of energy losses was fitted to the function $dE/dx = a + bE$ (Figure 3.21). The first two formulae for the photonuclear cross section (Section 3.10.3) can be fitted the best, all others lead to energy losses deviating more at higher energies from this simple linear formula; therefore the numbers given were evaluated using the first photonuclear cross section formula. In order to choose low and high energy limits correctly (to cover the maximum possible range of energies that could be comfortably fitted with a line), a χ^2 plot was generated and analyzed (Figure 3.22). The green curve corresponds to the χ^2 of the fit with a fixed upper bound and a varying lower bound on the fitted energy range. Correspondingly, the blue curve describes the χ^2 of the fit with a fixed lower bound and a varying upper bound. The χ^2 at low energies goes down sharply, then plateaus
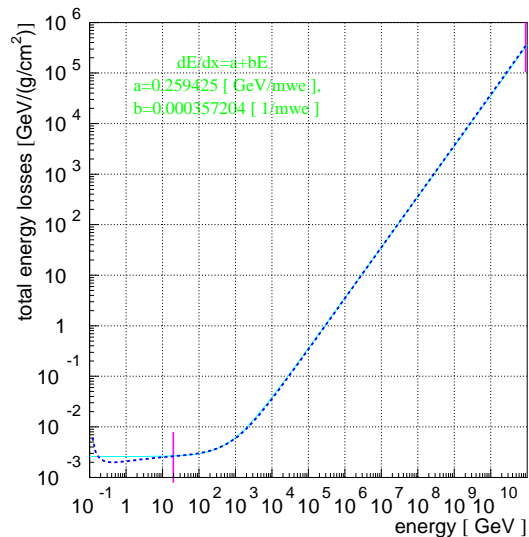
Figure 3.21: Fit to the energy losses in ice
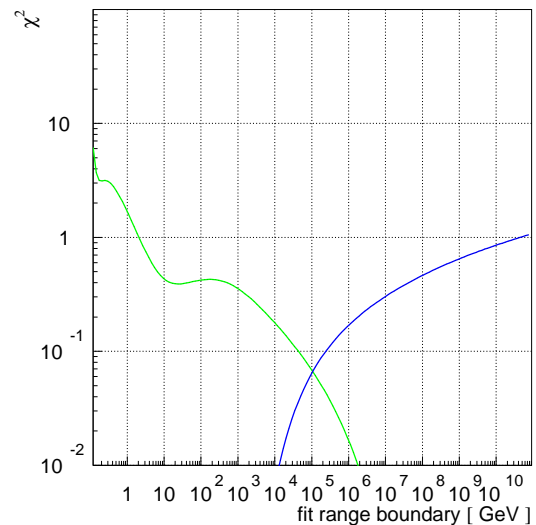
Figure 3.22: χ^2 plot for energy losses in ice

at around 10 GeV. This corresponds to the point where the linear approximation starts to work. For the high energy boundaries, χ^2 rises monotonically. This means that a linear approximation, though valid, has to describe a growing energy range. An interval of energies from 20 GeV to 10^{11} GeV is chosen for the fit. Table 3.3 summarizes the found fits to a and b; the errors in the evaluation of a

Table 3.3: Fits to a and b for continuous losses (average energy losses)

medium	$a, \frac{\text{GeV}}{\text{mwe}}$	$b, \frac{10^{-3}}{\text{mwe}}$	av. dev.	max. dev.
ice	0.259	0.357	3.7%	6.6%
fr. rock	0.231	0.429	3.0%	5.1%

and b are in the last digit of the given number. However, if the lower energy boundary of the fitted region is raised and/or the upper energy boundary is lowered, each by an order of magnitude, a and b change by about 1%.

To investigate the effect of stochastic processes, muons with energies $105.7\,\text{MeV}-10^{11}$ GeV were propagated to the point of their disappearance. The value of $v_{cut} = 5 \cdot 10^{-3}$ was used

in this calculation; using the the *continuous randomization* option did not change the final numbers. The average final distance (range) for each energy was fitted to the solution of the energy loss equation $dE/dx = a + bE$:

$$x_f = \log(1 + E_i \cdot b/a)/b$$

(Figure 3.23). The same analysis of the χ^2 plot as above was done in this case (Figure 3.24). A region of initial energies from 20 GeV to 10^{11} GeV was chosen for the fit. Table 3.4 summarizes the results of these fits.

Table 3.4: Fits to a and b for stochastic losses (average range estimation)

medium	a, $\frac{\text{GeV}}{\text{mwe}}$	b, $\frac{10^{-3}}{\text{mwe}}$	av. dev.
ice	0.268	0.470	3.0%
fréjus rock	0.218	0.520	2.8%
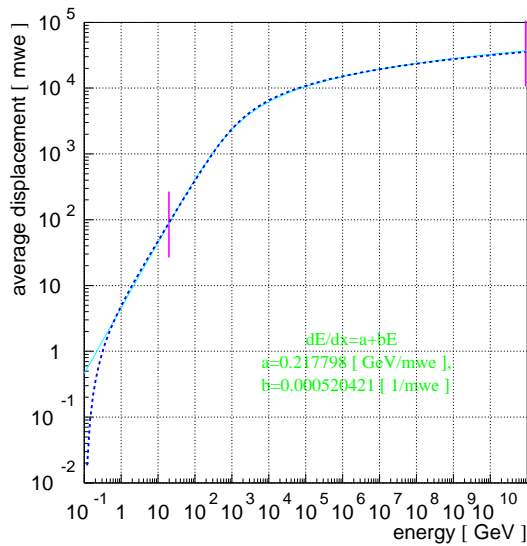
Figure 3.23: Fit to the average range in Fréjus rock
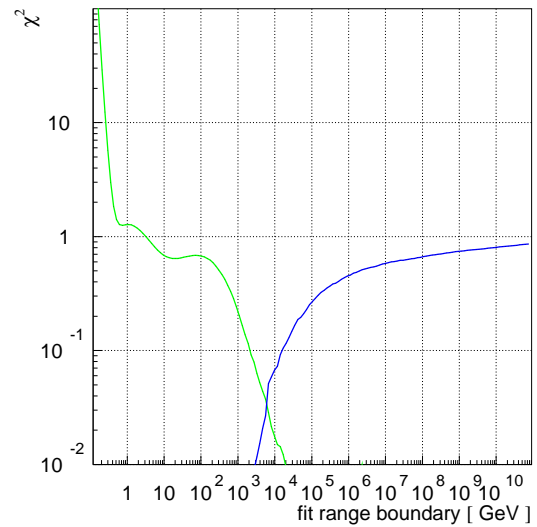
Figure 3.24: χ^2 plot for average range in Fréjus rock

As the energy of the muon increases, it suffers more stochastic losses before it is lost[2]

---

[2]As considered by the algorithm, here: stopped.
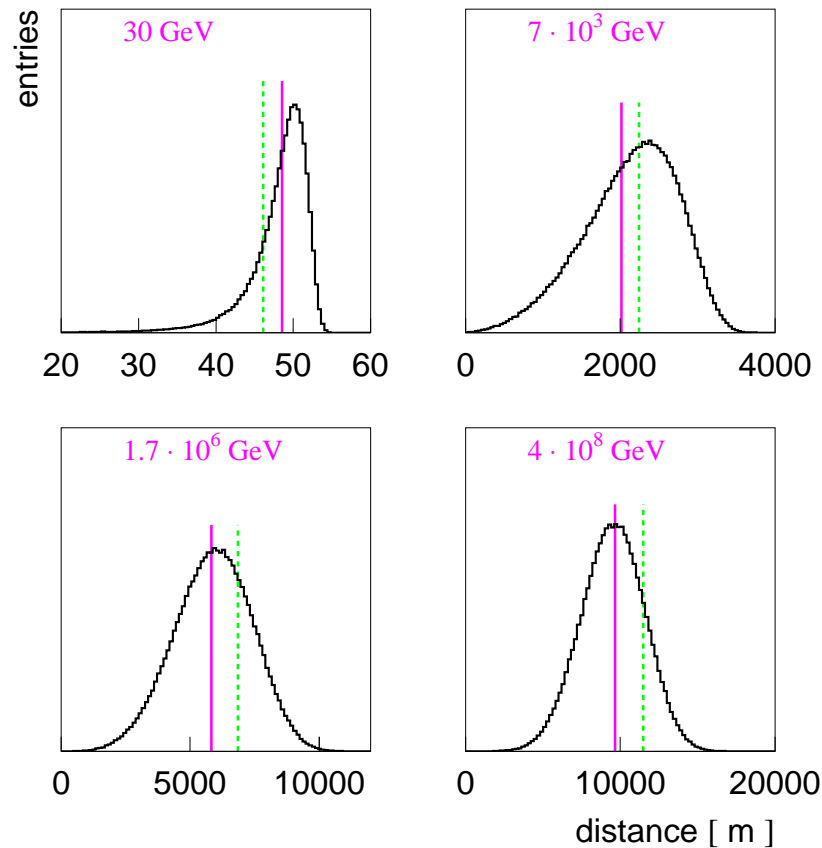
Figure 3.25: Range distributions in Fréjus rock: solid line designates the value of the range evaluated with the second table (continuous and stochastic losses) and the broken line shows the range evaluated with the first table (continuous losses only).

and the range distribution becomes more Gaussian-like (Figure 3.25). It is also shown in the figure (vertical lines) that the inclusion of stochastic processes makes the muons on average travel a shorter distance.

3.8   MMC implementation for AMANDA-II

Most light observed by AMANDA-II is produced by muons passing through a cylinder with radius 400 and length 800 meters around the detector (see Section 2.7 for discussion). Inside this cylinder, the Cherenkov radiation from the muon and all secondary showers along its track

with energies below 500 MeV (a somewhat loose convention) are estimated together. In addition to light produced by such a "dressed" muon, all secondary showers with energies above 500 MeV produced in the cylinder create their own Cherenkov radiation, which is considered separately for each secondary. So in the active region of the detector muons are propagated with $E_{cut} = 500$ MeV, creating secondaries on the way. This is shown as region 2 in the Figure 3.26.
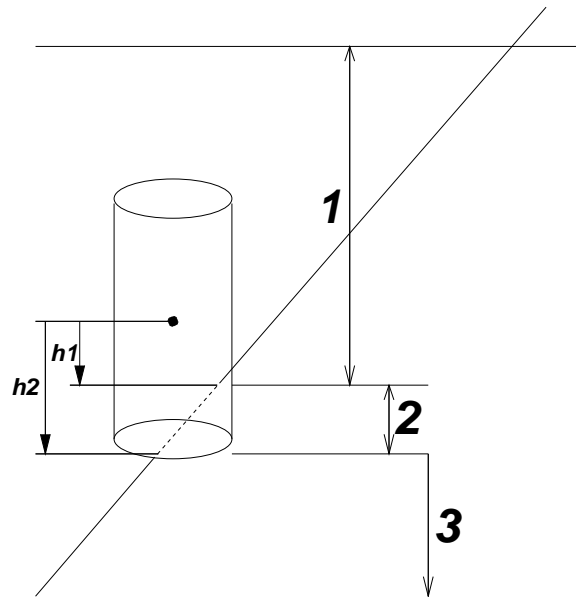
Figure 3.26: 3 regions of propagation defined for AMANDA-II simulation

In region 1, which is where the muon is propagated from the Earth's surface (or from under the detector) to the point of intersection of its track with the detector cylinder, muons should be propagated as fast as possible with the best accuracy. For downgoing muons, values of $v_{cut} = 0.05$ with the *continuous randomization* option enabled were found to work best. These values should also work for muons propagated from points which are sufficiently far from the detector. For muons created in the vicinity of the detector, values of $v_{cut} = 0.01$ with *cont* or even $v_{cut} = 0.001$ without *cont* should be used.

In region 3, which is where the muon exits the detector cylinder, it is propagated in one step ($v_{cut} = 1.0$, no *cont*) to the point of its disappearance, thus only resulting in an estimate of its average range.

It is possible to define multiple concentric media to describe both ice and rock below the ice, which is important for the study of the muons which might be created in either medium in or around the detector and then propagated toward it.

Although the ALLM parametrization of the photonuclear cross section was chosen to be the default for the simulation of AMANDA-II, other cross sections were also tested. No significant changes in the overall data rate or the number of channels (N_{ch}) distribution (important for the background muon analysis of this work) were found between 5 different parameterizations described in Section 3.10.3. This is to be expected since for the background muons (most of which have energies of 0.5-10 TeV on the surface) all photonuclear cross section parameterizations are very close to each other (see Figure 3.27). Also the effects of the Molière scattering and LPM-related effects (Section 3.10.7) can be completely ignored (although they have been left on for the default settings of the simulation).

3.9   Conclusions

A very versatile, clearly coded, and easy-to-use muon propagation Monte Carlo program (MMC) is presented. It is capable of propagating muon and tau leptons of energies from 105.7 MeV (muon rest mass, higher for tau) to 10^{11} GeV (or higher), which should be sufficient for the use as propagator in the simulations of the modern neutrino detectors. A very straightforward error control model is implemented, which results in computational errors being much smaller than

uncertainties in the formulae used for evaluation of cross sections. It is very easy to "plug in" cross sections, modify them, or test their performance. The program was extended on many occasions to include new formulae or effects. MMC propagates particles in three dimensions and takes into account Molière scattering on the atomic centers, which could be considered as the zeroth order approximation to true muon scattering since bremsstrahlung and pair production are effects that appear on top of such scattering. A more advanced angular dependence of the cross sections can be implemented at a later date, if necessary.

The MMC program was successfully incorporated into and used in the Monte Carlo chains of the AMANDA and Fréjus experiments. It is distributed at [36] in the hope that the combination of precision, code clarity, speed, and stability will make this program a useful tool in the research connected with high energy particles propagating through matter.

Also, a calculation of coefficients in the energy loss formula $dE/dx = a + bE$ and a similar formula for average range is presented for continuous (for energy loss) and stochastic (for average range calculation) energy loss treatments. The calculated coefficients apply in the energy range from 20 GeV to 10^{11} GeV with an average deviation from the linear formula of 3.7% and maximum of 6.6%.

3.10   Formulae

This section summarizes cross-section formulae used in MMC. In the formulae below, E is the energy of the incident muon, while $\nu = vE$ is the energy of the secondary particle: knock-on electron for ionization, photon for bremsstrahlung, virtual photon for photonuclear process, and electron pair for the pair production. As usual, $\beta = v/c$ and $\gamma = \left(1 - \beta^2\right)^{-1/2}$; also μ is muon

mass, $m = m_e$ is electron mass, and M is proton mass. Please refer to Appendix C for values of any constants appearing below. Most of the formulae in Sections 3.10.1−3.10.4 are taken directly from [18].

3.10.1 Ionization

A standard Bethe-Bloch equation given in [42] was modified for muon and tau charged leptons (massive particles with spin 1/2 different from electron) following the procedure outlined in [43]. The result is given below:

$$-\frac{dE}{dx} = Kz^2\frac{Z}{A\beta^2}\left[\frac{1}{2}\ln\left(\frac{2m_e\beta^2\gamma^2\nu_{upper}}{I(Z)^2}\right) - \frac{\beta^2}{2}\left(1 + \frac{\nu_{upper}}{\nu_{max}}\right) + \frac{1}{2}\left(\frac{\nu_{upper}}{2E(1 + 1/\gamma)}\right)^2 - \frac{\delta}{2}\right]$$

$$\text{where} \quad \nu_{max} = \frac{2m_e(\gamma^2 - 1)}{1 + 2\gamma\frac{m_e}{\mu} + \left(\frac{m_e}{\mu}\right)^2} \quad \text{and} \quad \nu_{upper} = \min(\nu_{cut}, \nu_{max}).$$

The density correction δ is computed as for nonconductors:

$$\delta = 0, \quad \text{if } X < X_0$$

$$\delta = 2(\ln 10)X + C + a(X_1 - X)^m, \quad \text{if } X_0 \leq X < X_1$$

$$\delta = 2(\ln 10)X + C, \quad \text{if } X \geq X_1 \quad \text{where} \quad X = \log_{10}(\beta\gamma)$$

$$\frac{d^2N}{d\nu dx} = \frac{1}{2}Kz^2\frac{Z}{A}\frac{1}{\beta^2}\frac{1}{\nu^2}\left[1 - \beta^2\frac{\nu}{\nu_{max}} + \frac{1}{2}\left(\frac{\nu}{E(1 + 1/\gamma)}\right)^2\right].$$

This formula, integrated from $\nu_{min} = \frac{1}{2m_e} \cdot \left(\frac{I(Z)}{\beta\gamma}\right)^2$ to ν_{upper}, gives the expression for energy loss above, less the density correction and β^2 terms (plus two more terms which vanish if $\nu_{min} \ll \nu_{upper}$).

3.10.2 Bremsstrahlung

According to [44], the bremsstrahlung cross section may be represented by the sum of an elastic component (σ_{el}, discussed in [45, 46]) and two inelastic components ($\Delta\sigma_{a,n}^{in}$),

$$\sigma = \sigma_{el} + \Delta\sigma_a^{in} + \Delta\sigma_n^{in}.$$

Elastic Bremsstrahlung:
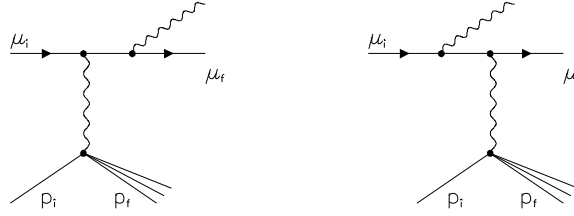
$$\sigma_{el}(E, v) = \frac{\alpha}{v}\left(2Z\frac{m}{\mu}r_e\right)^2\left(\frac{4}{3} - \frac{4}{3}v + v^2\right)\left[\ln\left[\frac{\mu}{\delta}\right] - \frac{1}{2} - \Delta_a^{el} - \Delta_n^{el}\right],$$

$$\text{where}\quad \delta \approx \frac{\mu^2\omega}{2E(E-\omega)},$$

is the minimum momentum transfer. The formfactors (atomic Δ_a^{el} and nuclear Δ_n^{el}) are

$$\Delta_a^{el}(\delta) = \ln\left[1 + \frac{1}{\delta\sqrt{e}BZ^{-1/3}/m}\right]$$

$$\Delta_n^{el}(\delta) = \ln\left[\frac{D_n}{1 + \delta(D_n\sqrt{e} - 2)/\mu}\right]; \qquad D_n = 1.54A^{0.27}.$$

Inelastic Bremsstrahlung:

The effect of nucleus excitation can be evaluated as

$$\Delta_n^{in} = \frac{1}{Z}\Delta_n^{el};\ (Z \neq 1).$$

Bremsstrahlung on the atomic electrons can be described by the diagrams below; e-diagram is included with ionization losses (because of its sharp $1/v^2$ energy loss spectrum), as

described in [47]:

$$\Delta \frac{d^2 N}{d\nu dx} = \left(\frac{d^2 N}{d\nu dx} \right)_{I_0} \cdot \frac{\alpha}{2\pi} (a(2b + c) - b^2)$$

$$a = \log(1 + 2\nu/m_e), \quad b = \log((1 - \nu/\nu_{max})/(1 - \nu/E)),$$

$$c = \log((2\gamma(1 - \nu/E)m_e)/(m_\mu \nu/E)).$$

The maximum energy lost by a muon is the same as in the pure ionization (knock-on) energy losses. The minimum energy is taken as $\nu_{min} = I(Z)$. In the above formula ν is the energy lost by the muon, i.e., the sum of energies transferred to both electron and photon. On the output all of this energy is assigned to the electron.

μ diagrams
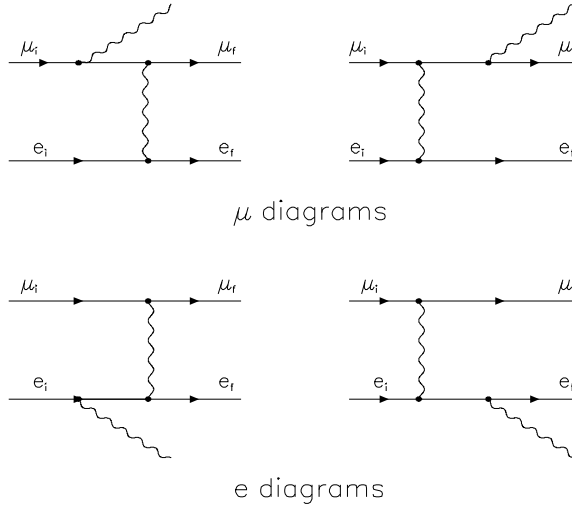
e diagrams

The contribution of the μ-diagram (included with bremsstrahlung) is discussed in [44]:

$$\Delta \sigma_a^{in}(E, v) \approx \frac{\alpha}{v} \left(2Z \frac{m}{\mu} r_e \right)^2 \left(\frac{4}{3} - \frac{4}{3}v + v^2 \right) \Delta_a^{in}$$

$$\Delta_a^{in} \approx \frac{1}{Z} \tilde{\Phi}_a^{in}(\delta) \quad \text{with} \quad \tilde{\Phi}_a^{in}(\delta) = \ln \left[\frac{\mu/\delta}{\delta \mu/m^2 + \sqrt{e}} \right] - \ln \left[1 + \frac{m}{\delta \sqrt{e} B' Z^{-2/3}} \right]$$

B'=1429 for $Z \geq 2$ and B'=446 for Z=1.

The maximum energy transferred to the photon is

$$v_{max} = \frac{m(E - \mu)}{E(E - p + m)}.$$

On the output all of the energy lost by a muon is assigned to the bremsstrahlung photon.

3.10.3 Photonuclear interactions
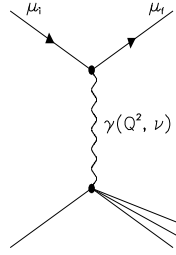
Th photonuclear cross section is used as parametrized in [48]:

$$
\begin{aligned}
\frac{d\sigma}{dv} &= \frac{\alpha}{2\pi} A\sigma_{\gamma N} v \left\{ 0.75 G(x) \left[\kappa \ln\left(1 + \frac{m_1^2}{t}\right) - \frac{\kappa m_1^2}{m_1^2 + t} - \frac{2\mu^2}{t} \right] + \right. \\
&+\left. 0.25 \left[\kappa \ln\left(1 + \frac{m_2^2}{t}\right) - \frac{2\mu^2}{t} \right] + \frac{\mu^2}{2t}\left[0.75 G(x) \frac{m_1^2}{m_1^2 + t} + 0.25 \frac{m_2^2}{t} \ln\left(1 + \frac{t}{m_2^2}\right) \right] \right\},
\end{aligned}
$$

where $\quad t = Q_{max}^2 = \dfrac{\mu^2 v^2}{1 - v}$, $\quad \kappa = 1 - \dfrac{2}{v} + \dfrac{2}{v^2}$, $\quad m_1^2 = 0.54\,\text{GeV}^2$, and $\quad m_2^2 = 1.8\,\text{GeV}^2$.

Nucleon shadowing is taken care of by

$$\sigma_{\gamma A}(\nu) = A\sigma_{\gamma N}(\nu)\{0.75 G(x) + 0.25\}$$

$$\text{with } G(x) = \frac{3}{x^3}\left(\frac{x^2}{2} - 1 + e^{-x}(1 + x)\right), \quad \text{for } Z \neq 1, \text{ and } G(x) = 1 \text{ for Z=1}$$

$$x = Rn\sigma_{\rho N} \simeq 0.00282 A^{\frac{1}{3}} \sigma_{\gamma N}(\nu).$$

Several parametrization schemes for the photon-nucleon cross section are implemented. The first is

$$\sigma_{\gamma N}(\nu) = 96.1 + \frac{82}{\sqrt{\nu}}, \quad \text{for } \nu \leq 17 \text{ GeV}$$

$$\sigma_{\gamma N}(\nu) = 114.3 + 1.647 \ln^2[0.0213\nu]\ \mu\text{b}, \quad \text{for } \nu \in [17, 200 \text{ GeV}]\ [48]$$

$$\sigma_{\gamma N}(\nu) = 49.2 + 11.1 \ln[\nu] + 151.8/\sqrt{\nu}\ \mu\text{b}, \quad \text{above } 200 \text{ GeV } [49].$$

The second is based on the table parametrization of [50] below 17 GeV. Since the second formula from above is valid for energies up to 10^6 GeV, it is taken to describe the whole energy range alone as the third case. Formula [51]

$$\sigma_{\gamma N}(\nu) = 63.5 s^{0.097} + 145 s^{-0.5} \ \mu\text{b} \quad \text{with} \quad s = 2M\nu$$

can also be used in the whole energy range, representing the fourth case (see Figure 3.27). Finally, the ALLM parametrization (discussed in Section 3.10.8) can be enabled. It does not rely on the assumption that the virtual photon can be considered as real and involves integration over the square of the photon 4-momentum (Q^2).

Integration limits used for the photonuclear cross section are (kinematic limits for Q^2 are used for the ALLM cross section)

$$m_\pi + \frac{m_\pi^2}{2M} \quad < \quad \nu < E - \frac{M}{2} \cdot \left(1 + \frac{m_\mu^2}{M^2} \right)$$

$$\frac{m_\mu^2 \nu^2}{EE'} - \frac{m_\mu^4}{2EE'} \quad < \quad Q^2 < 2M(\nu - m_\pi) - m_\pi^2 \ , \quad E' = E - \nu.$$

3.10.4 Electron pair production

Two out of four diagrams describing pair production are shown below. These describe the dominant "electron" term. The other two have the muon interacting with the atom and represent the "muon" term. The cross section formulae used here were first derived in [52, 53, 54].
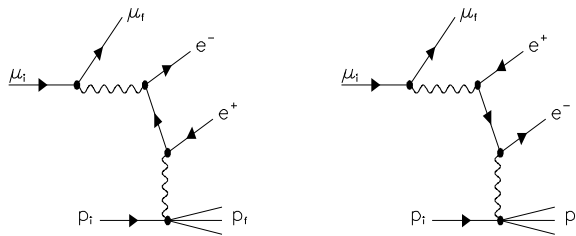
$$\frac{d\sigma(E,v,\rho)}{dvd\rho} = \frac{2}{3\pi}Z(Z+\zeta)(\alpha r_e)^2\frac{1-v}{v}\left(\Phi_e + \frac{m^2}{\mu^2}\Phi_\mu\right)$$

$$v = (\epsilon_+ + \epsilon_-)/E, \quad \rho = (\epsilon_+ - \epsilon_-)/E$$

$$\Phi_e = \left\{[(2+\rho^2)(1+\beta) + \xi(3+\rho^2)]\ln\left(1+\frac{1}{\xi}\right) + \frac{1-\rho^2-\beta}{1+\xi} - (3+\rho^2)\right\}L_e$$

$$\Phi_\mu = \left\{\left[(1+\rho^2)\left(1+\frac{3}{2}\beta\right) - \frac{1}{\xi}(1+2\beta)(1-\rho^2)\right]\ln(1+\xi) + \right.$$

$$\left. + \quad \frac{\xi(1-\rho^2-\beta)}{1+\xi} + (1+2\beta)(1-\rho^2)\right\}L_\mu$$

$$L_e = \ln\left(\frac{BZ^{-1/3}\sqrt{(1+\xi)(1+Y_e)}}{1+\frac{2m\sqrt{e}BZ^{-1/3}(1+\xi)(1+Y_e)}{Ev(1-\rho^2)}}\right) - \frac{1}{2}\ln\left[1+\left(\frac{3m}{2\mu}Z^{1/3}\right)^2(1+\xi)(1+Y_e)\right]$$

$$L_\mu = \ln\left(\frac{\frac{2}{3}\frac{\mu}{m}BZ^{-2/3}}{1+\frac{2m\sqrt{e}BZ^{-1/3}(1+\xi)(1+Y_\mu)}{Ev(1-\rho^2)}}\right)$$

$$Y_e = \frac{5-\rho^2+4\beta(1+\rho^2)}{2(1+3\beta)\ln(3+1/\xi) - \rho^2 - 2\beta(2-\rho^2)}$$

$$Y_\mu = \frac{4+\rho^2+3\beta(1+\rho^2)}{(1+\rho^2)(3/2+2\beta)\ln(3+\xi) + 1 - \frac{3}{2}\rho^2}$$

$$\beta = \frac{v^2}{2(1-v)}, \quad \xi = \left(\frac{\mu v}{2m}\right)^2\frac{1-\rho^2}{1-v}$$

$$\zeta_{loss}^{pair}(E,Z) \sim \frac{0.073\ln\left(\frac{E/\mu}{1+\gamma_1 Z^{2/3}E/\mu}\right) - 0.26}{0.058\ln\left(\frac{E/\mu}{1+\gamma_2 Z^{1/3}E/\mu}\right) - 0.14}$$

$$\gamma_1 = 1.95\ 10^{-5} \quad \text{and} \quad \gamma_2 = 5.3\ 10^{-5} \quad \text{for} \quad Z \neq 1$$

$$\gamma_1 = 4.4\ 10^{-5} \quad \text{and} \quad \gamma_2 = 4.8\ 10^{-5} \quad \text{for} \quad Z = 1.$$

Integration limits for this cross section are

$$\frac{4m}{E} = v_{min} \leq v \leq v_{max} = 1 - \frac{3\sqrt{e}}{4}\frac{\mu}{E}Z^{1/3}$$

$$0 \leq |\rho| \leq \rho_{max} = \sqrt{1-\frac{4m}{Ev}}\left[1-\frac{6\mu^2}{E^2(1-v)}\right]$$

Muon pair production is discussed in detail in [55] and is not considered by MMC. Its cross section is estimated to be $\sim 2 \cdot 10^4$ times smaller than the direct electron pair production cross section discussed above.

3.10.5   Muon decay

Muon decay probability is calculated according to

$$\frac{dN}{dx} = \frac{1}{\gamma\beta c\tau}.$$

The energy of the outgoing electron is evaluated as

$$\nu_e = \gamma\left(\nu_{rest} + \beta\sqrt{\nu_{rest}^2 - m_e^2}\cos(\theta)\right).$$

The value of $\cos(\theta)$ is distributed uniformly on $(-1, 1)$ and ν_{rest} is determined at random from the distribution

$$\frac{dN}{dx} = \frac{G^2\mu^5}{192\pi^3}(3 - 2x)x^2, \quad x = \frac{\nu}{\nu_{max}} \quad \text{with} \quad \nu_{min} = m_e \quad \text{and} \quad \nu_{max} = \frac{\mu^2 + m_e^2}{2\mu}.$$

3.10.6   Molière scattering

After passing through a distance x, the angular distribution is assumed Gaussian with a width $\sqrt{2}\theta_0$ [42]:

$$\theta_0 = \frac{13.6\,MeV}{\beta cp}z\sqrt{x/X_0}\left[1 + 0.038\ln(x/X_0)\right]$$

$$X_0 \quad \text{is evaluated as} \quad X_0 = \left[\frac{\sigma_{brems}(E_{big})}{E_{big}}\right]^{-1} \quad \text{for} \quad E_{big} \approx 10^{20}\text{eV}.$$

Deviations in two directions perpendicular to the muon track are independent, but for each direction the exit angle and lateral deviation are correlated:

$$y_{plane} = z_1 x\theta_0/\sqrt{12} + z_2 x\theta_0/2 \quad \text{and} \quad \theta_{plane} = z_2\theta_0$$
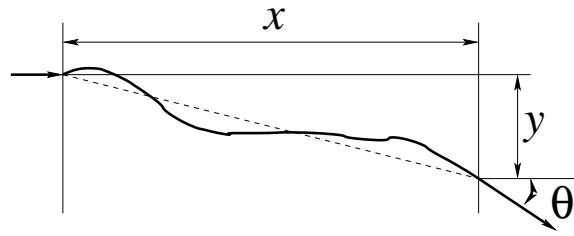
for independent standard Gaussian random variables (z_1, z_2). A more precise treatment should take

the finite size of the nucleus into account as described in [56]. See Figure 3.31 for an example of

Molière scattering of a high energy muon.

3.10.7 Landau-Pomeranchuk-Migdal and Ter-Mikaelian effects

These affect bremsstrahlung and pair production. See Figure 3.30 for the combined effect

in ice and Fréjus rock.

LPM suppression of the bremsstrahlung cross section:

The bremsstrahlung cross section is modified as follows [57, 58, 59]:

$$\frac{4}{3}(1 - v) + v^2 \rightarrow \frac{\xi(s)}{3}\left(v^2 G(s) + 2[1 + (1 - v)^2]\phi(s)\right).$$

The regions of the following expressions for $\phi(s)$ and $G(s)$ were chosen to represent the best continuous approximation to the actual functions:

$$\phi(s) = 1 - \exp\left(-6s\left[1 + (3 - \pi)s\right] + \frac{s^3}{0.623 + 0.796s + 0.658s^2}\right) \quad \text{for} \quad s < 1.54954$$

$$\phi(s) = 1 - 0.012/s^4 \quad \text{for} \quad s \geq 1.54954$$

$$\psi(s) = 1 - \exp\left(-4s - \frac{8s^2}{1 + 3.936s + 4.97s^2 - 0.05s^3 + 7.50s^4}\right)$$

$$G(s) = 3\psi(s) - 2\phi(s) \quad \text{for} \quad s < 0.710390$$

$$G(s) = 36s^2/(36s^2 + 1) \quad \text{for} \quad 0.710390 \leq s < 0.904912$$

$$G(s) = 1 - 0.022/s^4 \quad \text{for} \quad s \geq 0.904912.$$

Here the SEB scheme [60] is employed for evaluation of $\phi(s)$, $\psi(s)$, and $\xi(s)$ below:

$$\xi(s') = 2 \quad \text{for} \quad s' < s_1$$

$$\xi(s') = 1 + h - \frac{0.08(1 - h)[1 - (1 - h)^2]}{\ln s_1} \quad \text{for} \quad s_1 \leq s' < 1$$

$$\xi(s') = 1 \quad \text{for} \quad s' \geq 1$$

$$E_{LPM} = \frac{\alpha(\mu c^2)^2 X_0}{4\pi\hbar c}.$$

X_0 is the same as in Section 3.10.6. Here are the rest of the definitions:

$$s = \frac{s'}{\sqrt{\xi}} \quad s_1 = \sqrt{2}\frac{Z^{1/3}D_n}{B}\frac{m_e}{\mu} \quad s' = \sqrt{\frac{E_{LPM}v}{8E(1 - v)}} \quad h = \frac{\ln s'}{\ln s_1}.$$

Dielectric (Longitudinal) suppression effect:

In addition to the above change of the bremsstrahlung cross section, s is replaced by $\Gamma \cdot s$ and functions $\xi(s)$, $\phi(s)$, and $G(s)$ are scaled as [59]

$$\xi(s) \rightarrow \xi(\Gamma s) \quad \phi(s) \rightarrow \phi(\Gamma s)/\Gamma \quad G(s) \rightarrow G(\Gamma s)/\Gamma^2.$$

Therefore the first formula in the previous section is modified as

$$\frac{4}{3}(1-v)+v^2 \rightarrow \frac{\xi(\Gamma s)}{3}\left(v^2\frac{G(\Gamma s)}{\Gamma^2}+2[1+(1-v)^2]\frac{\phi(\Gamma s)}{\Gamma}\right).$$

$$\Gamma \quad \text{is defined as} \quad \Gamma = 1+\gamma^2\left(\frac{\hbar\omega_p}{vE}\right)^2,$$

where $\omega_p = \sqrt{4\pi NZe^2/m}$ is the plasma frequency of the medium and vE is the photon energy.

The dielectric suppression affects only processes with small photon transfer energy, therefore it is

not directly applicable to the direct pair production suppression.

LPM suppression of the direct pair production cross section:

Φ_e from the pair production cross section is modified as follows [59, 61]:

$$\Phi_e \rightarrow \left((1+\beta)(A+[1+\rho^2]B)+\beta(C+[1+\rho^2]D)+(1-\rho^2)E\right)\cdot L_e$$

$$s = \frac{1}{4}\sqrt{\frac{E_{LPM}}{E_\mu}\frac{1}{v(1-\rho^2)}}.$$

The E_{LPM} energy definition is different than in the bremsstrahlung case:

$$E_{LPM} = \frac{\mu^4}{2\pi n\alpha^2\sum Z^2 L} \quad \text{where} \quad L = \ln(3.25BZ^{-1/3}).$$

Functions $A(s,\xi)$, $B(s,\xi)$, $C(s,\xi)$, and $D(s,\xi)$ are based on the approximation formulae

$$\Phi(s) = \frac{6s}{6s+1} \quad \text{and} \quad G(s) = \frac{(6s)^2}{(6s)^2+1}$$

and are given below:

$$A(s,x) = \frac{G}{2}(1+2Gx)\ln\frac{36s^2(1+x)^2+1}{36s^2x^2}-G+6Gs\left(1+\frac{36s^2-1}{36s^2+1}x\right)\left(\arctan(6s[x+1])-\frac{\pi}{2}\right)$$

$$B(s,x) = \Phi(1+\Phi x)\ln\frac{6s(1+x)+1}{6sx}-\Phi$$

$$C(s,x) = -G^2 x \ln \frac{36s^2(1+x)^2 + 1}{36s^2x^2} + G - \frac{G^2(36s^2 - 1)}{6s}x\left(\arctan(6s[x+1]) - \frac{\pi}{2}\right)$$

$$D(s,x) = \Phi - \Phi^2 x \ln \frac{6s(1+x)+1}{6sx}$$

$$E(s,x) = -6s\left(\arctan(6s[x+1]) - \frac{\pi}{2}\right).$$

3.10.8 The Abramowicz Levin Levy Maor (ALLM) parametrization of the photonuclear cross section

The ALLM formula is based on the parametrization [62, 63, 64]

$$\frac{d\sigma(v,Q^2)}{dvdQ^2} = \frac{4\pi\alpha^2}{Q^4}\frac{F_2}{v}\left[1 - v - \frac{Mxv}{2E} + \left(1 - \frac{2\mu^2}{Q^2}\right)\frac{v^2(1+4M^2x^2/Q^2)}{2(1+R))}\right]$$

$$x = \frac{Q^2}{2MEv}.$$

The limits of integration over Q^2 are given in the section for photonuclear cross section.

$$F_2 = a(Z + (A-Z)P)F_2^p \quad \text{Here,} \quad a(A,x,Q^2) \simeq a(A,x)$$

$$a(A,x) = A^{-0.1} \quad \text{for} \quad x < 0.0014$$

$$a(A,x) = A^{0.069\log_{10}x + 0.097} \quad \text{for} \quad 0.0014 \leq x < 0.04$$

$$a(A,x) = 1 \quad \text{for} \quad x \geq 0.04$$

$$F_2^p(x,Q^2) = \frac{Q^2}{Q^2 + m_0^2}(F_2^P + F_2^R)$$

$$F_2^i(x,Q^2) = c_i x_i^{a_i}(1-x)^{b_i} \quad \text{for} \quad i = P, R$$

$$\text{For} \quad f = c_R, a_R, b_R, b_P \qquad f(t) = f_1 + f_2 t^{f_3}$$

$$\text{For} \quad g = c_P, a_P \qquad g(t) = g_1 + (g_1 - g_2)\left[\frac{1}{1+t^{g_3}} - 1\right]$$

$$t = \ln \frac{\ln \frac{Q^2 + Q_0^2}{\Lambda^2}}{\ln \frac{Q_0^2}{\Lambda^2}}$$

$$x_i = \frac{Q^2 + m_i^2}{Q^2 + m_i^2 + W^2 - M^2} \quad \text{for} \quad i = P, R,$$

where W is the invariant mass of the nucleus plus virtual photon [65]: $W^2 = M^2 + 2MEv - Q^2$.

Figure 3.28 compares ALLM-parametrized cross section with formulae of Bezrukov and Bugaev from Section 3.10.3.

The quantity $R(x, Q^2)$ is not very well known, although it has been measured for high x ($x > 0.1$) [66] and modeled for small x ($10^{-7} < x < 0.1$, $0.01\ \text{GeV}^2 < Q^2 < 50\ \text{GeV}^2$) [67]. It is of the order $\sim 0.1 - 0.3$ and even smaller for small Q^2 (behaves as $O(Q^2)$). In Figure 3.29 three photonuclear energy loss curves for R=0, 0.3, and 0.5 are shown. The difference between the curves never exceeds 7%. In the absence of a convenient parametrization for R at the moment, it is set to zero in MMC.
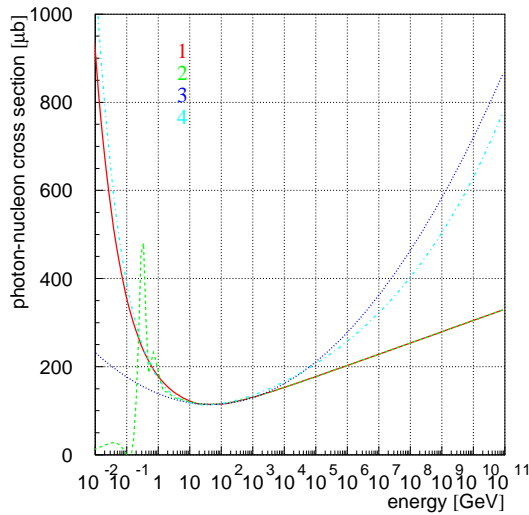
Figure 3.27: Photon-nucleon cross sections, as described in the text (Bezrukov Bugaev parametrization): 1 (solid), 2 (dashed), 3 (dotted), 4(dashed-dotted)
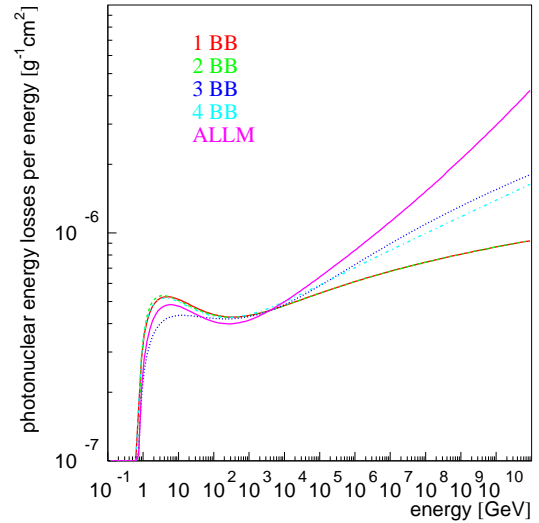
Figure 3.28: Photonuclear energy losses (divided by energy), according to different formulae. Designations are the same as in Figure 3.27, higher solid line is for ALLM parametrization
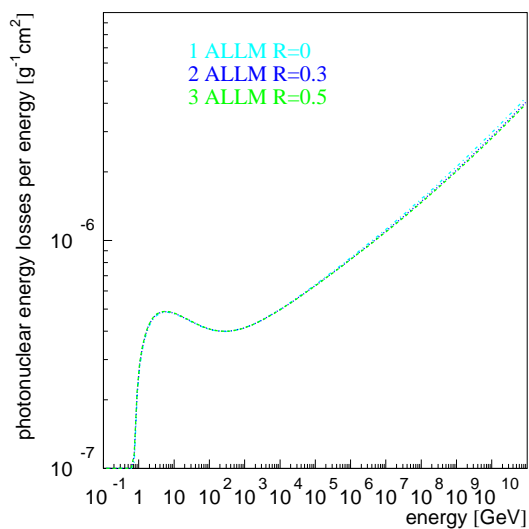
Figure 3.29: Comparison of ALLM energy loss (divided by energy) for R=0 (dashed-dotted), R=0.3 (dotted), R=0.5 (dashed)
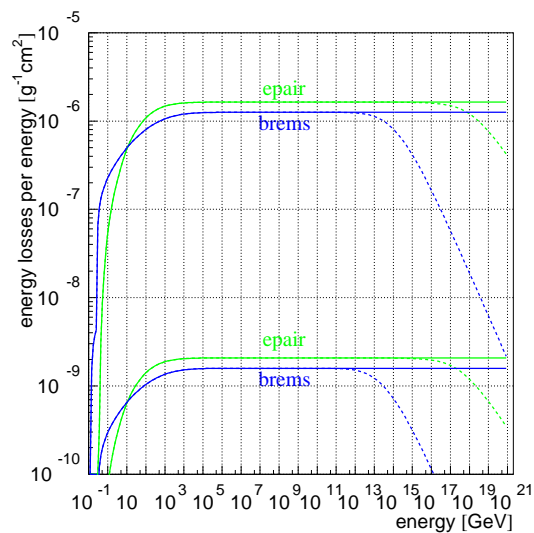
Figure 3.30: LPM effect in ice (higher plots) and Fréjus rock (lower plots, multiplied by 10^{-3})
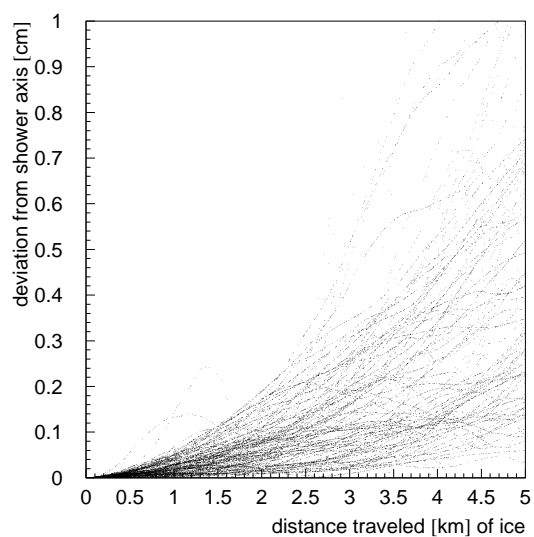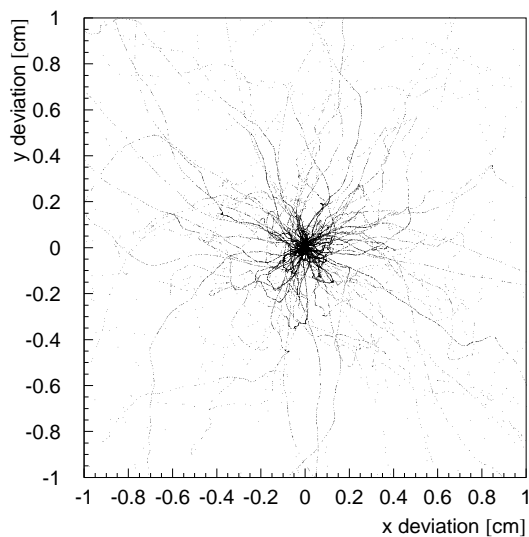
Figure 3.31: Molière scattering of one hundred 10 TeV muons going straight down through ice

Chapter 4

Cosmic Ray Energy Spectrum

Measurement with AMANDA

- Please make yourselves uncomfortable -

4.1   Muon energy loss in the AMANDA-II detector

This section starts with the description of a simple model of the distribution of the number

of hit channels (N_{ch}) observed in AMANDA-II.

For a muon track going through the detector, the number of OMs within the cylinder of

radius R centered on the track is counted (Figure 4.1). The resulting number of OMs less than

a distance R away from the track is averaged over several thousand "representative" muon tracks

going through a grid of points with -100 m $< x, y < 100$ m in the $z = 0$ plane with zenith angles

$10° \leq \theta < 70°$ and azimuth angles $0° \leq \phi < 360°$. The resulting $N(R)$ and $\frac{dN(R)}{dr}$ distributions

are shown in Figure 4.2. An "average" muon has most of the detector OMs within 200 m of its
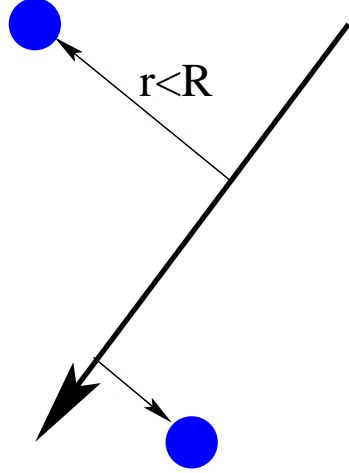
Figure 4.1: Counting OMs around the muon track
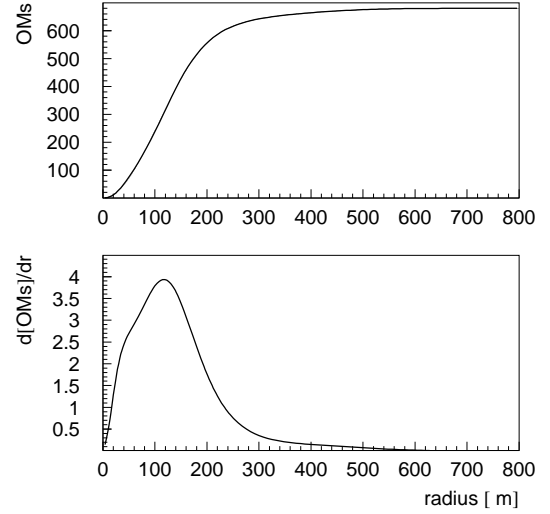
Figure 4.2: OM counts for an "average" muon track

track.

The probability to see a photon at a distance r from its origin (sufficiently large so that the photon suffers at least a few scatterings) at time t is [68, 69]

$$p(r, t) = \frac{1}{(4\pi D t)^{3/2}} \exp\left\{ -\frac{r^2}{4Dt} - \frac{c_i t}{\lambda_a} \right\}.$$

Here $D = \frac{c_i \lambda_{eff}}{3}$ with $\lambda_{eff} = \frac{\lambda_{scat}}{1 - \tau}$ and $\tau = <\cos(\theta_{scat})>$,

where λ_a is the absorption length and $c_i = c_{\text{vac}}/n$ is the speed of light in the ice. The probability to see the photon pass through a sphere of radius R_{OM} located at distance r, integrated over time, is

$$p(r) = \pi R_{OM}^2 \cdot \frac{c_i}{4} \cdot \frac{1}{4\pi D r} e^{-\frac{r}{\lambda_{prop}}}, \text{ where } \lambda_{prop} = \sqrt{\frac{\lambda_a \lambda_{eff}}{3}}.$$

Introducing the OM sensitivity $s = \frac{1}{2} \cdot efficiency$[1], the probability to record the photon at distance r is

$$P(r) = s \cdot \frac{3R_{OM}^2}{16\lambda_{eff}} \cdot \frac{1}{r} e^{-\frac{r}{\lambda_{prop}}}.$$

[1] The value of $\frac{1}{2}$ represents the ability of an OM to see photons arriving to only half of its surface.

This is only valid for $r \gg \lambda_{eff}$ (diffusive approximation). In the opposite case of very small r, scattering is negligible, and one obviously has

$$P(r) = s \cdot \frac{\pi R_{OM}^2}{4\pi r^2} e^{-\frac{r}{\lambda_a}}.$$

In the simplified model that follows, both functions are stitched together and λ_a is assumed $\sim \lambda_{prop}$.

A more precise analytical treatment is possible assuming the hit probability is determined by the following functional form of the photon arrival time distribution (pandel function: [70]):

$$p(t_{res}) = \frac{1}{N(d)} \frac{\tau^{-(d/\lambda)} \cdot t_{res}^{(d/\lambda - 1)}}{\Gamma(d/\lambda)} \cdot e^{-\left(t_{res} \cdot \left(\frac{1}{\tau} + \frac{c_i}{\lambda_a} \right) + \frac{d}{\lambda_a} \right)}, \quad \text{with}$$

$$N(d) = e^{-d/\lambda_a} \cdot \left(1 + \frac{\tau \cdot c_i}{\lambda_a} \right)^{-d/\lambda}.$$

The best values of free parameters τ, λ, and the absorption length λ_a which fit AMANDA-II delay probabilities are shown below:

$$\tau = 557 \text{ ns} \quad \lambda = 33.3 \text{ m} \quad \lambda_a = 98 \text{ m}.$$

This formula gives the distribution of the residual time t_{res}, which is the difference of the arrival time of the scattered photon and the time for a photon not deflected during its propagation (a direct photon). The distance d between muon track and location of the optical module can be replaced with the effective distance d_{eff} which depends on the orientation of the OM to result in a better description of data. For a full AMANDA-II simulation a different approach based on tabulated probability functions (PTD, [71]) is used. It was found to have insufficient accuracy due to the layered structure of the optical properties of ice at AMANDA-II depths (Figure 4.3). A better description, which was recently developed (PHOTONICS [21]), can correctly account for all features of ice measured at the location of the detector. It was not used for the analysis in this work, however, since it requires significantly larger computer resources to achieve the required statistics of the simulated data.
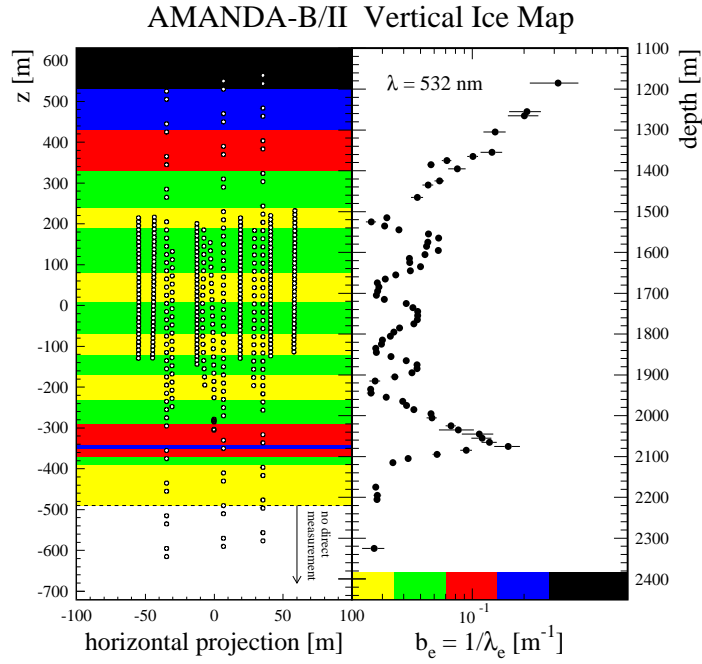
Figure 4.3: Layered optical properties of ice at the location of the AMANDA-II detector

A muon passing through the detector deposits an amount of energy proportional to its average energy while inside the detector. Most of this energy is eventually passed to photons which are then detected with the probability functions given above. In the following it is assumed that the number of photons produced by the muon and all secondary showers along its path is proportional to its energy: $N_{phot} = E/E_0$. This is valid for muons with sufficiently large energies as seen from the following. The number of Cherenkov photons produced by a muon is [72]

$$\frac{dN_c}{dl\,d\lambda} = 2\pi\alpha \sin^2\Theta_c \frac{1}{\lambda^2}.$$

Here α is the fine structure constant. Although the number of Cherenkov photons generated by a muon itself is mostly independent of its energy (proportional to its track length, though), the secondary showers left by the muon increase its *effective* track length by an amount proportional to

their energy

$$l_{eff} = \frac{E}{\text{GeV}} \begin{cases} 4.371 & \text{for electromagnetic shower} \\[2mm] 3.501 & \text{for hadronic shower .} \end{cases}$$

The total energy of secondaries left by the muon inside the detector volume is proportional to the

muon energy (see Figures D.29 and D.30) when the muon energy is sufficiently high, therefore the

total number of the Cherenkov photons in this case is also proportional to the muon energy inside

the detector.

Summing up the photon hits inside the detector, the muon with energy E should produce

an event with on average $N(E)$ hit OMs:

$$N(E) = \int_{+0}^{\infty} \left(1 - (1 - P(r))^{E/E_0}\right) \frac{dN(r)}{dr} dr$$

$$\approx \int_{+0}^{\infty} \left(1 - e^{-P(r) \cdot E/E_0}\right) \frac{dN(r)}{dr} dr.$$

The N_{ch} distribution is then given by

$$d\Phi \approx \Phi_0 \left(\frac{E}{E_0}\right)^{-(\gamma+1)} dE = \Phi_0 \left(\frac{E(N)}{E_0}\right)^{-(\gamma+1)} \frac{dN}{dN/dE} = P(N)dN,$$

$$\text{where} \quad \frac{dN}{dE} = \int_{+0}^{\infty} \frac{P(r)}{E_0} e^{-P(r) \cdot E/E_0} \frac{dN(r)}{dr} dr.$$

In the above, the muon flux is assumed to have a power law spectrum with exponent $-(\gamma + 1)$. For

high enough energy, muons obey this energy spectrum at the surface, according to the formula [5]

$$\frac{dN}{dE} = 0.14 \text{ cm}^{-2}\text{sr}^{-1}\text{s}^{-1}\text{GeV}^{-1} \cdot A \cdot \left(\frac{E_\mu}{\text{GeV}}\right)^{-\gamma} \cdot \left(\frac{1}{1 + \frac{1.1E_\mu \cos\theta}{115 \text{ GeV}}} + \frac{0.054}{1 + \frac{1.1E_\mu \cos\theta}{850 \text{ GeV}}}\right).$$

According to the muon energy loss approximation (see Section 3.7),

$$\frac{dE}{dx} = a + b \cdot E \quad \text{with } a = 0.259\frac{\text{GeV}}{\text{mwe}}, b = 0.357\frac{10^{-3}}{\text{mwe}}$$

$$\Rightarrow E_f = E_i \cdot e^{-bx} - \frac{a}{b}(1 - e^{-bx}),$$
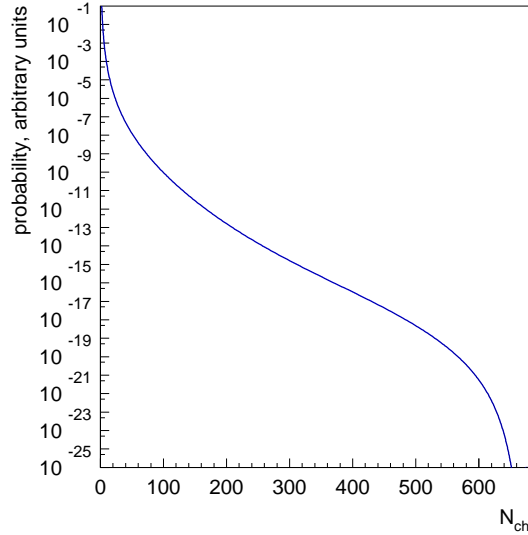
Figure 4.4: Model of N_{ch} distribution

i.e., $E_f \approx E_i$ for high enough initial energy. As the energy of the muon drops below 1 TeV, the muon energy spectrum is no longer a power law with $-(\gamma + 1)$ exponent. However, for this work it is only important that the energy spectrum of muons at the location of the detector is falling with a slope which depends on γ.

Since $P(r)$ comes in the combination $P(r)/E_0$, the only effect of the sensitivity s of the OMs is on the overall normalization of the N_{ch} distribution. By changing E_0 to compensate for changes in s we simply change the region of energies which the detector can see. The resulting N_{ch} distribution for $s = 0.17$, $\lambda_{eff} = 100$ m, $\lambda_{prop} = 35$ m, $\gamma = 2.76$, and $E_0 = 200$ MeV is shown in Figure 4.4.

Since λ_{prop} is known with limited precision, it would be interesting to find a quantity which depends strongly on the spectral index γ and normalization Φ_0, but less so on λ_{prop}. The next section discusses some features of the N_{ch} distribution which appear to have this quality.

4.2 A model of N_{ch} distribution

From Section 4.1,

$$N(E_\mu) \approx \int_{+0}^\infty \left(1 - e^{-P(r) \cdot P_{ph}(E_{loss}(E_\mu))}\right) \frac{dN(r)}{dr} dr.$$

For small N_{ch}, e.g., small $P_{ph}(E_{loss}(E_\mu))$,

$$N(E_\mu) \approx \int_{+0}^\infty P(r) \cdot P_{ph}(E_{loss}(E_\mu)) \frac{dN(r)}{dr} dr.$$

Assume that the OM depth density ρ

$$\int_{h_1}^{h_2} \rho dh = \int_{+0}^\infty P(r) \frac{dN(r)}{dr} dr$$

is constant with depth h. Introducing the depth h dependence of the muon energy E_μ, for a cylindrical detector located between depths h_1 and h_2 and a muon track going vertically down,

$$N = \int_{h_1}^{h_2} E_{loss}(h; E_\mu) \rho dh.$$

Here $P_{ph}(E)$ is assumed proportional to E, and the coefficient of proportionality is included in ρ.

Let E_μ be the muon energy at the surface. Then, solving the muon energy loss approximation equation $dE/dx = a + bE$ between $E_i = E(0)$ and $E_f = E(h)$,

$$\frac{dE}{dx}(h) = a + bE_f = (a + bE_i) \cdot e^{-bh}.$$

Therefore,

$$N = (a + bE_i) \int_{h_1}^{h_2} e^{-bh} \rho dh.$$

Depending on whether the muon stops inside the detector (at h, determined by $e^{bh} = 1 + bE_i/a$) or goes through (see Figure 4.5), one gets two solutions:
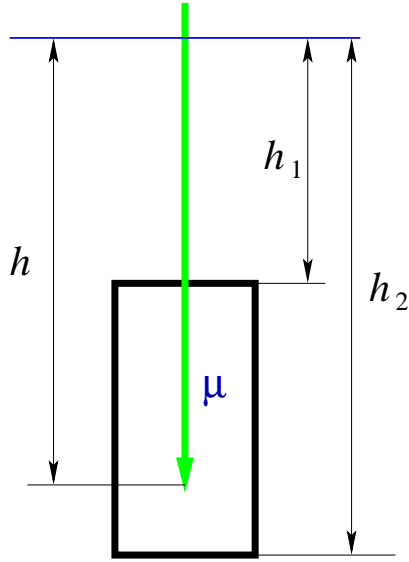
Figure 4.5: Simple model diagram: muon propagating straight down
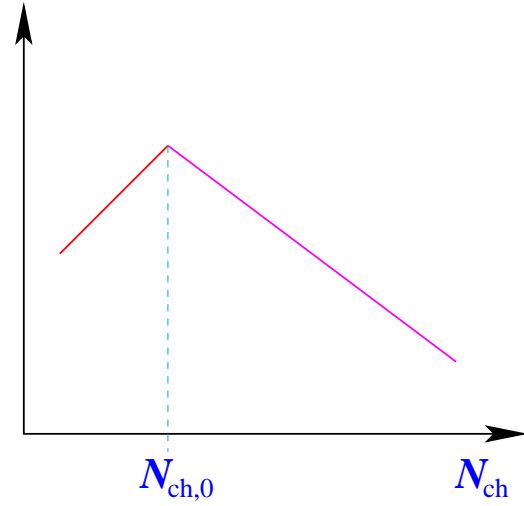
Figure 4.6: Observed break in the N_{ch} distribution

$$N = (a + bE_i) \cdot \frac{\rho}{b} \cdot \begin{cases} e^{-bh_1} - e^{-bh_2}, & (1) \\ \\ e^{-bh_1} - \frac{1}{1+\frac{bE_i}{a}}, & (2) \end{cases}$$

$$N = \begin{cases} (a + bE_i) \cdot \frac{\rho}{b}(e^{-bh_1} - e^{-bh_2}) & = (a + bE_i) \cdot A \\ \\ (a + bE_i) \cdot \frac{\rho}{b}e^{-bh_1} - \frac{\rho a}{b} & = (a + bE_i) \cdot B - C. \end{cases}$$

Therefore, for a muon spectrum of $\Phi = \Phi_0 \cdot E^{-\gamma}$ at the surface,

$$\Phi = \Phi_0 \cdot \begin{cases} \left(\frac{N-aA}{bA}\right)^{-\gamma} \\ \\ \left(\frac{N+C-aB}{bB}\right)^{-\gamma} \end{cases} \Rightarrow N \cdot (\log\Phi)' = \begin{cases} \frac{-\gamma N}{N-aA} \\ \\ \frac{-\gamma N}{N+C-aB}. \end{cases}$$

A change in slope occurs at $N_{ch,0}$ corresponding to $E_{i,0} = (e^{bh} - 1) \cdot a/b$ (Figure 4.6), which depends only on the geometrical configuration of the detector. Therefore, the number of events with N_{ch} above $N_{ch,0}$ can be used to get the total flux above $E_{i,0}$, i.e., to find the normaliza-

Figure 4.7: Muon energy loss inside the detector cylinder
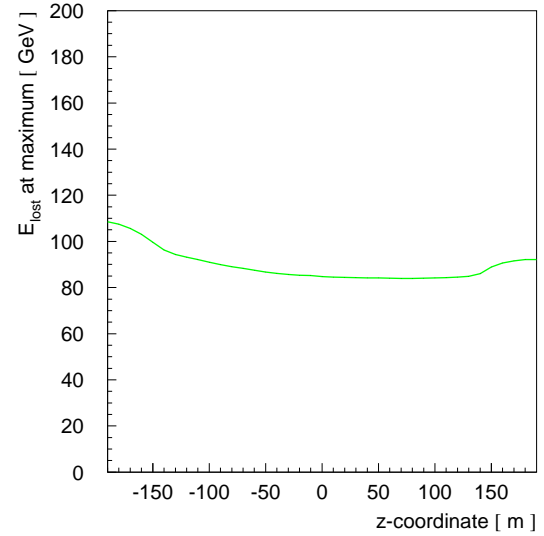
Figure 4.8: Muon energy loss for muons with $E_i = E_{i,0}$, which pass through depth z

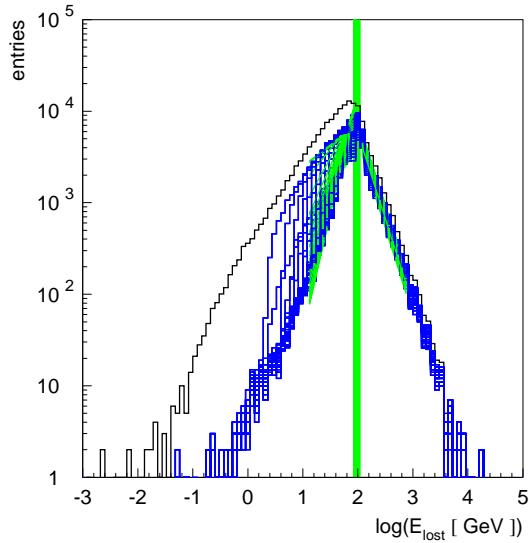tion constant Φ_0.

At this N_{ch} the slope $N \cdot (\log \Phi)'$ (to the right or left) is proportional to γ. It can also be seen that it does not depend on the OM sensitivities or ice properties, since ρ cancels out.

To evaluate the energy loss per event in the detector, a Monte Carlo chain consisting of only CORSIKA and MMC was run. The detector was assumed to have a radius of 125 meters and a length of 400 meters. A "-user" option was used to record muon energy when entering and leaving (if leaving) the active volume of the detector, which allowed the calculation of the total energy deposited by all muons in the event inside the active volume of the detector. From the discussion above, this energy is proportional to N_{ch}.

For each layer[2] inside the detector (z-coordinates -200 through 200), the energy lost by muons is histogrammed if at least one muon from the bundle reaches that layer. The distributions are found to follow the broken spectrum described above, and the maxima (corresponding to the

---

[2]Here: 40 equally spaced horizontal planes.

Figure 4.9: Results of the fits to the normalization depth profiles
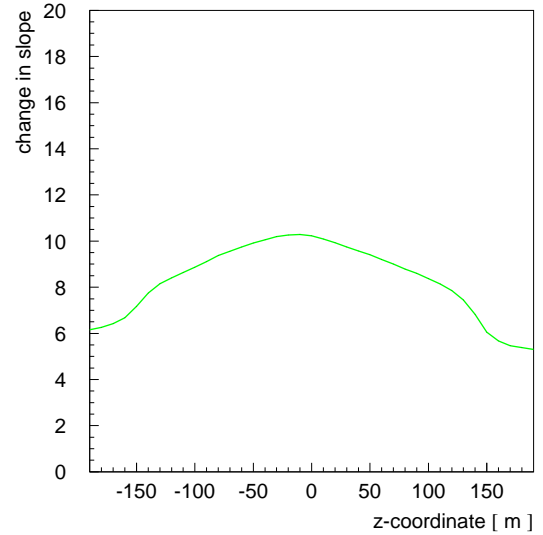
Figure 4.10: Results of the fits to the slope depth profiles
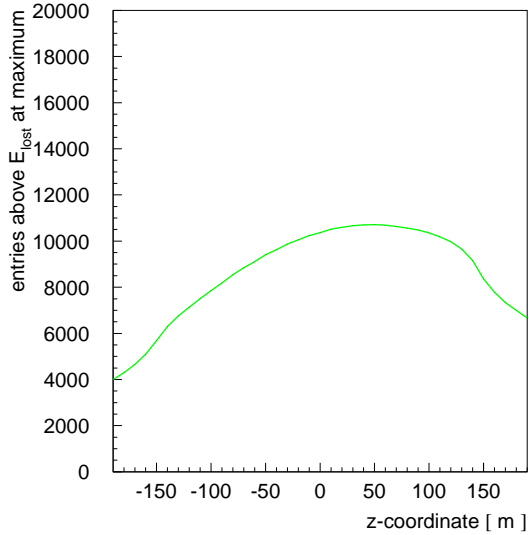
break point) are denoted by green lines (Figure 4.7). The energy for muons reaching a given z-coordinate corresponding to the breaking point $E_{lost,0}$ in the distribution of $N_{ch} \propto E_{lost}$ depends weakly on the depth and is roughly 85-90 GeV (Figure 4.8). The model predicts depth profiles of the normalization and slope change as shown in Figures 4.9 and 4.10. The energy of a typical muon losing energy $E_{lost,0}$ inside the active volume of the detector is about 1 TeV (Figure 4.11), and the energy of a typical primary creating such a muon is about 14 TeV (Figure 4.12).

Figure 4.13 shows muon energy lost inside the detector cylinder. The features of the full Monte Carlo simulation can be explained by muons going through different parts of the detector at different angles.

Consider muons going straight down through the center of the detector (blue histogram in Figure 4.13). When their energy is less than $\sim$ 100 GeV, muons stop inside the detector and the energy loss is equal to the energy of the muons at the top of the detector (as seen from Figure 4.14). As the muon energies increase, they start going through the detector and lose only a part of their

Figure 4.11: Average energy of the muons at the surface

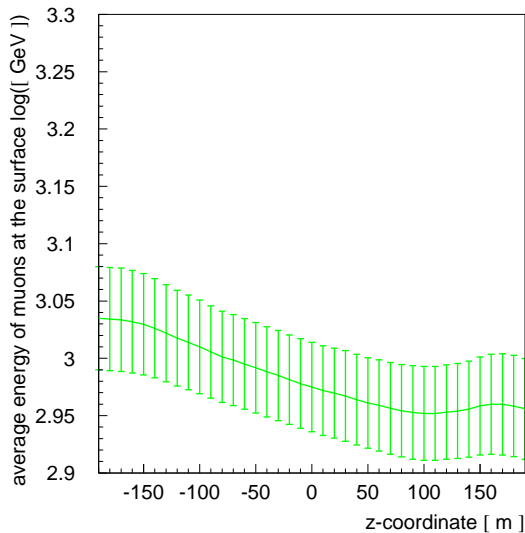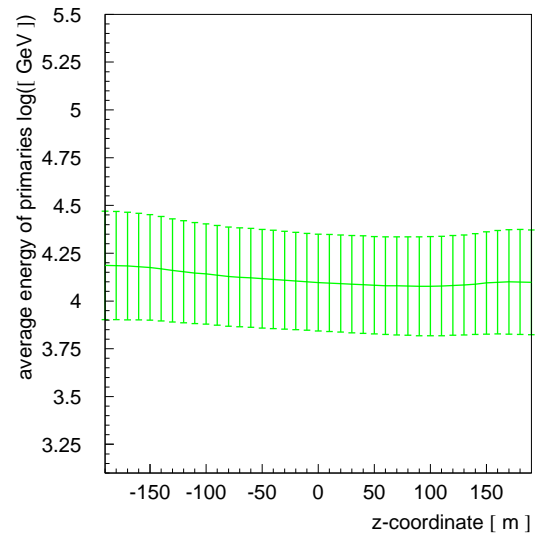Figure 4.12: Average energy of primaries

energy. Up to some ~ 500 GeV, muon energy losses are mostly continuous (ionization losses) and are therefore independent of the energy of the muon at the top of the detector. For the same reason the muon energy losses at these energies are very deterministic (almost no stochastic part) so that the energy lost inside the detector is well defined, which explains why the peak is so sharp. This peak is the focus of the first method described below. As the muon energy increases beyond ~ 1 TeV, its energy losses become proportional to its energy, and the slope of the distribution increases, creating the *upturn* which is used by the second method.

Once muons coming from all directions and at different distances away from the detector center are included in the simulation, the peak becomes quite a bit broader. The double-peak structure visible in the black histogram in Figure 4.13 is an artifact of the cylindrical geometry used for this model. The real detector consists of OMs and some volume around them which is only roughly cylindrical. This substantially smoothens the observed N_{ch} distribution.

The described mechanism for the *upturn* feature is not the only reason for the upturn

Figure 4.13: Muon energy loss inside the detector cylinder

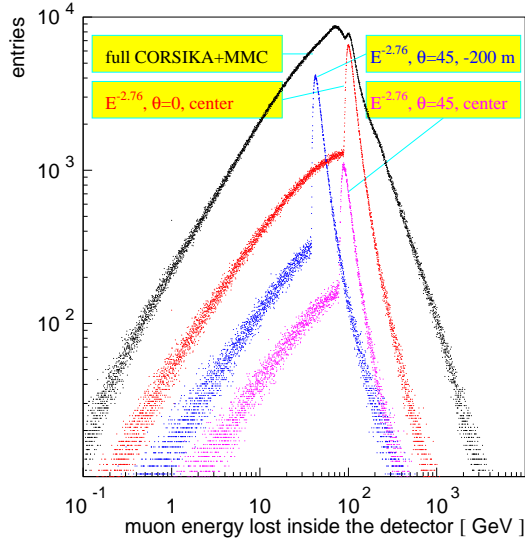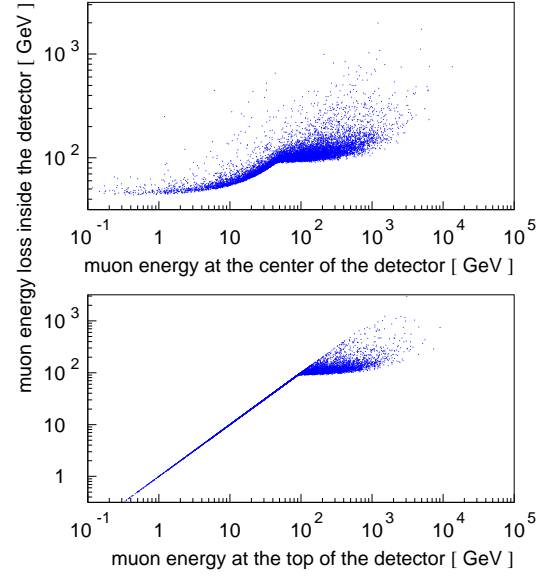Figure 4.14: Muon energy lost inside the detector cylinder vs. muon energy at the center and top of the detector

observed in the N_{ch} distribution in data (also in the simple model described in Section 4.1, Figure 4.4). Other reasons include the change in the OM counts for the typical muon track (Figure 4.2) and the change in the behavior of the photon propagation probability (Figure 4.1). For a range of parameters compatible with AMANDA-II settings and measured ice properties it is nevertheless possible to use the *upturn* for an estimate of the spectral index γ in a way which depends only weakly on these parameters. Figure 4.15 shows simulated N_{ch} distributions (for the model described in Section 4.1) for six values of γ from 2.0 to 3.0. For each value of γ, 14 plots for λ_{prop} varying from 24 to 50 m are shown in different colors. All curves were fitted between the yellow lines with $\exp(p_1 + p_2 \cdot N_{ch}) + \exp(p_3 + p_4 \cdot N_{ch})$. A quantity $\log(\exp(p_3)/\exp(p_1)) = p_3 - p_1$ describing the slope change rate at the *upturn* point was found to depend weakly on λ_{prop} while changing significantly with γ (Figure 4.16).

In the model of N_{ch} distribution discussed in Section 4.1 (and Figure 4.4) several sim-
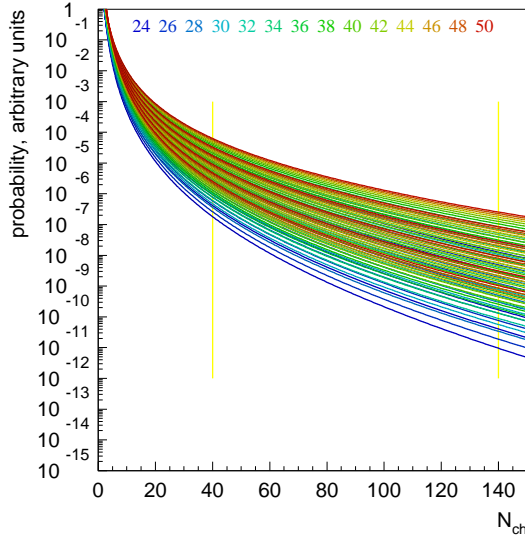
Figure 4.15: N_{ch} distribution for γ from 2.0 to 3.0 and λ_{prop} from 24 to 50
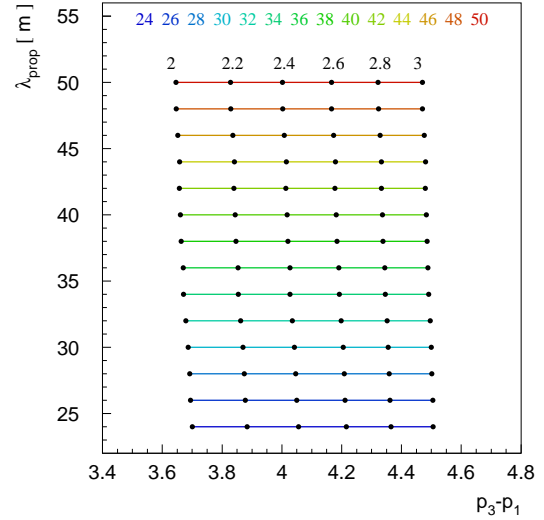
Figure 4.16: Results of the fits to the N_{ch} distributions

plifications were made. First, the number of OMs $N(R)$ within a distance R of the muon track was assumed the same for all OMs. Scattering and absorption lengths and OM sensitivities were assumed to be constant throughout the detector. A muon is assumed to go through the detector without changing its energy. Only the average N_{ch} was evaluated for each muon energy. All these simplifications can be removed by doing the detailed detector simulation (Monte Carlo using AMASIM [17]), which is what is done in the following discussion. Different ice property and OM sensitivity parameter sets which vary these parameters around their measured values were used (see Appendix E.1).

4.3 Noise cleaning and OM efficiency

Signals from all optical modules are corrected by subtracting noise from signal and adding muons passing through the depth of each OM which are not recorded by it, i.e., "muon signal" =
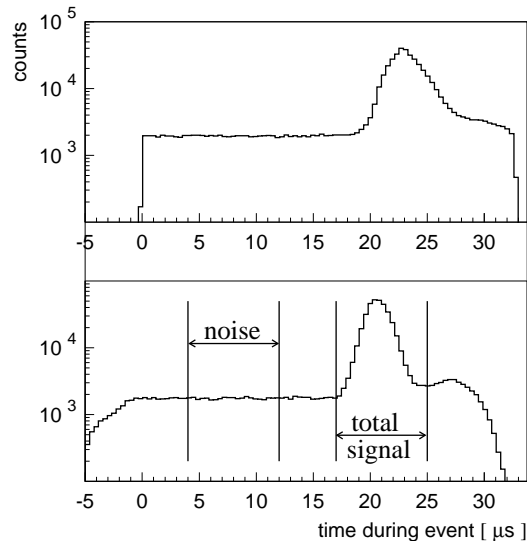
Figure 4.17: Selecting time windows using uncalibrated (top) and calibrated (bottom) data
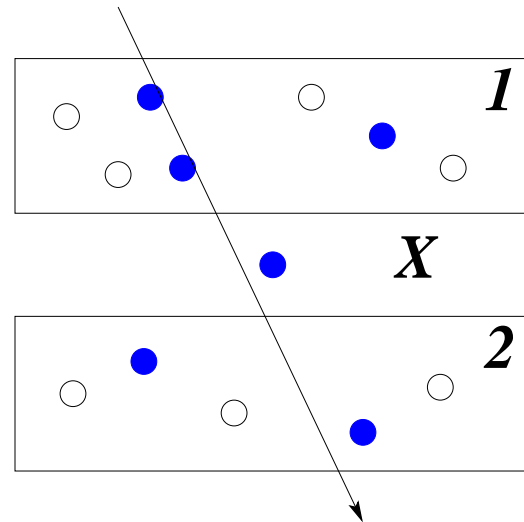
Figure 4.18: Layered construction for efficiency determination

signal − noise + missed signal.

With the current data-taking setup in AMANDA-II it is possible to evaluate the noise distribution in the detector independently from the signal. One simply needs to select hits during some time window before the trigger fires (and the majority of muon-related hits come in). In Figure 4.17 two windows are selected: one for noise and another for "total signal" = signal + noise.

The width of the window is chosen so as to contain most of the signal. Each OM is counted if it has been hit at least once. Therefore for the following analysis afterpulses coming from the signal are counted as signal, and those coming from noise are counted as noise. Consequently, the window can be selected to be very large (up to 16 μs). However, with the larger window noise hits will occur in almost every event, so the noise subtraction algorithm will not work (or lose precision and require substantially larger statistics). On the plot in Figure 4.17 two hit time distributions are shown: one for uncalibrated data (containing times of signal arrival at the surface)

and another for time-calibrated data (which contains signal times at the location of OMs). It appears that the muon hits form a peak, which is more compact when the data are calibrated. The acceptable choice of the signal and noise windows was found to be 8000 ns when used with a calibrated file.

In the following, events are counted as 1 if there was at least one hit in the corresponding window. For each OM, the probability to have noise during the noise window in N_{all} events is evaluated as $P_n = \frac{N_{noise}}{N_{all}}$. The probability to have any signal (muon signal or noise) during the signal window is $P_t = \frac{N_{tot.\ sig.}}{N_{all}}$. The probability to have at least one muon signal during the signal window is then $P_s = \frac{N_{muon\ sig.}}{N_{all}}$. Since these events are uncorrelated, the probability to have neither noise nor muon signal during the signal window is equal to $1 - P_t = (1 - P_s) \cdot (1 - P_n)$, i.e., $P_s = 1 - \frac{1-P_t}{1-P_n}$, and $N_{muon\ sig.} = P_s \cdot N_{all}$.

Let us designate the "efficiency" of an OM as the ratio of the number of muon signals the OM recorded to the total number of muons which crossed the depth at which this OM is located and caused the detector to trigger. If the efficiency of the OM at $z = h$ were known, the signal from this OM could be used to compute the number of muons which passed the depth $z = h$ and were recorded by the detector. To determine the efficiency of OM "X," the simple construction shown in Figure 4.18 is used. If the muon was seen in a layer above OM "X" (shown as "1") and in a layer below (shown as "2"), then it must have passed through the depth of the OM "X." Let us denote by 1 and 2 the number of events in which there was muon signal in the layer above (1) and below (2) OM "X", respectively. Correspondingly, X denotes the number of events in which OM "X" had muon signal. Then the efficiency of OM "X" is determined as

$$\frac{X \cap (1 \cap 2)}{1 \cap 2}$$
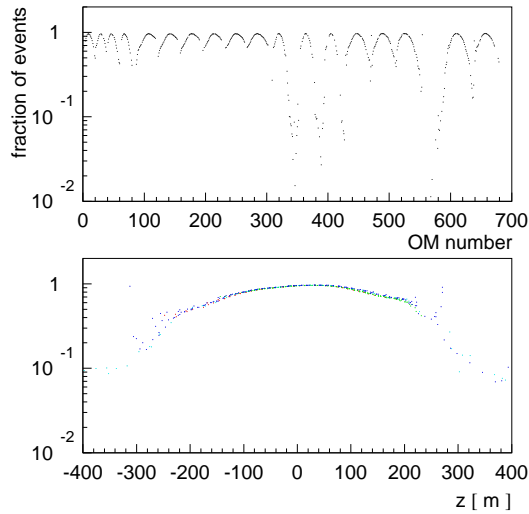
Number of muons seen inside the detector as a function of depth

Figure 4.19: efficiency-governed signal   Figure 4.20: "mean field" calculation
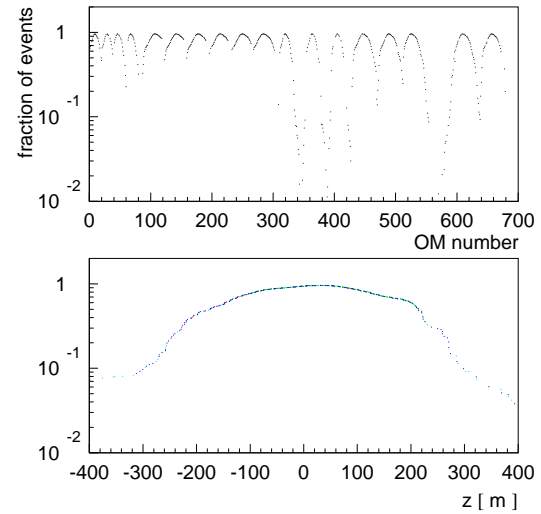
and the number of muons which passed through the depth of OM "X" can be estimated as

$$X \cdot \frac{1 \cap 2}{X \cap (1 \cap 2)}$$

and is shown in Figure 4.19 as a function of OM number and depth.

To estimate the quantities $1 \cap 2$ and $X \cap (1 \cap 2)$, the following relations were used:

$$1 \cup 2 = 1 + 2 - 1 \cap 2 \quad \Rightarrow \quad 1 \cap 2 = 1 + 2 - 1 \cup 2$$

$$X \cap (1 \cap 2) = 1 + 2 + X - 1 \cup 2 - 1 \cup X - 2 \cup X + 1 \cup 2 \cup X.$$

Since the noise subtraction algorithm works not only for single OMs, but also for unions of OMs, the quantities 1, 2, X, $1 \cup 2$, $1 \cup X$, $2 \cup X$, and $1 \cup 2 \cup X$ are estimated for signal and noise time windows, and then subtracted from each other using the noise subtraction formula to get these quantities for the "pure" muon signal.

In Figure 4.19 the numbers of muons show slight variations from one OM to the next

(most of the variation is between different strings). This is due to the fact that the efficiency, estimated with the above method, is only valid for muons with energy high enough to be seen in both layers 1 and 2. In order to get the total muon counts one has to interpolate this value for the lower energy muons, which are seen in the layer 1, but not 2.

It is possible to avoid this interpolation. Denote by $P(S)$ the total number of muons which pass through the layer containing the set S of OMs. Then obviously,

$$P(X \cap (1 \cap 2)) = P(1 \cap 2) \quad \Rightarrow$$

$$P(1) + P(2) - P(1 \cap 2) = P(1) + P(2) + P(X) - P(1 \cup 2)$$

$$-P(1 \cup X) - P(2 \cup X) + P(1 \cup 2 \cup X) \quad \Rightarrow$$

$$P(X) = P(1 \cup X) + P(2 \cup X) - P(1 \cup 2 \cup X).$$

Sets $1 \cup X$, $2 \cup X$, and $1 \cup 2 \cup X$ can be chosen very large so that

$$P(1 \cup X) \approx 1 \cup X$$

$$P(2 \cup X) \approx 2 \cup X$$

$$P(1 \cup 2 \cup X) \approx 1 \cup 2 \cup X.$$

If the sets 1 and 2 are chosen such as to extend to the very top and bottom of the detector, then the last relation is exact: all muons which trigger the detector will show up in at least one of 1, 2, or X. The quantity $P(X)$ is then the number of muons which pass through the depth of OM "X" and trigger the detector. The sensitivity of OM "X" can now be evaluated as $X/P(X)$, but it is of
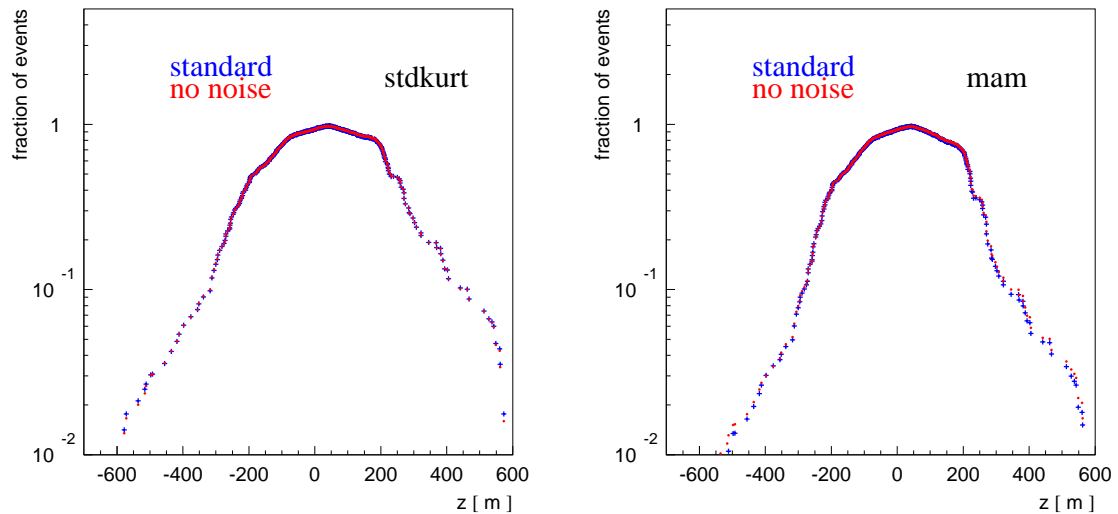
Figure 4.21:

Comparison of Monte Carlo samples with and without noise

secondary interest. Figure 4.20 shows the number of muons passing though the depths of detector

OMs vs. OM number and vs. depth, evaluated using the second method.

For simulated data it is possible to eliminate noise by removing those hits. Curves pro-

duced by applying the algorithm to the simulated data with and without noise follow each other

closely (Figure 4.21), so the noise subtraction method works well, as expected.

To estimate the range of depths for which the algorithm works, it has been applied to the

same simulated data samples with height of sets 1 and 2 fixed at $100 - 800$ meters. As mentioned

above, the thicker the layers 1 and 2, the more precise is the method. As seen from Figure 4.22, all

curves for set sizes of $300 - 800$ meters follow each other closely, i.e., acceptable choices of set

1 and 2 heights are above 300 meters, with the 200 meter choice being quite good, too. Therefore

the algorithm can be applied at depths 300 meters away from the detector top and bottom, i.e., the

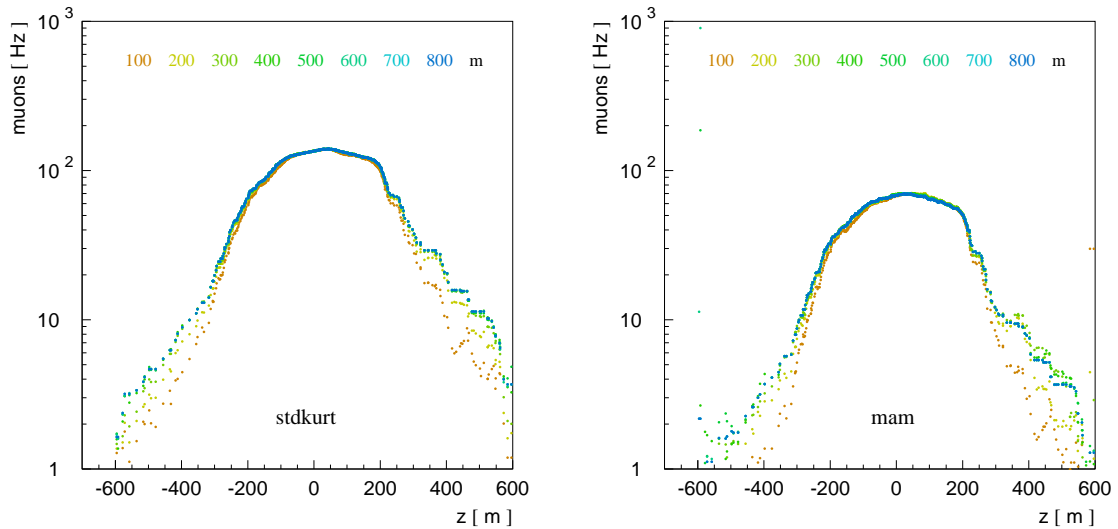layers at z-coordinates of $\pm 100 - 200$ meters.

Figure 4.22:

Results for different layer sizes

The algorithm was applied to different subsets of data, requiring the number of channels hit to be at least 20 to 120 (see Figure 4.23). Then for each layer (at z in the range of $\pm 100 - 200$ meters), the corresponding N_{ch} distributions were calculated. Figure 4.24 shows muon-signal depth profiles for N_{ch} equal to $27 - 40$. The lower plot is only made for muons coming down at zenith angles of less than $30°$ from the z-axis. Since about half of the observed muons come from this direction (see Figure 2.4) the two plots are very similar, although the curve corresponding to $N_{ch} = 40$ in the lower plot does look flatter in the applicable region ($|z| < 100$ m). This is expected since all muons which enter the detector at the top with sufficiently high N_{ch} will exit at the bottom (i.e., there are no muons going at shallow angles through just the middle of the detector). At lower N_{ch} (27 or above) the number of observed muons rises with z, which is consistent with muons stopping inside the detector before reaching the bottom.
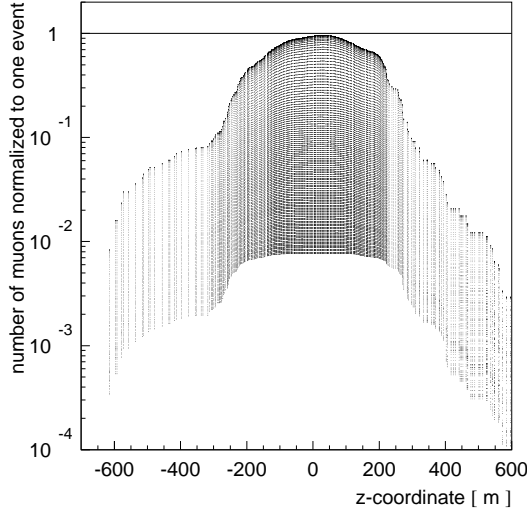
Profiles of the number of muons seen at all depths inside the detector

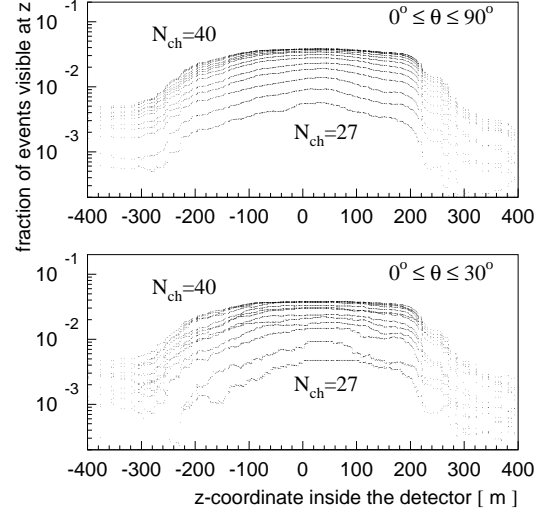Figure 4.23: for $N_{ch} \geq 20 - 120$ Figure 4.24: with fixed $N_{ch} = 27 - 40$

4.4 Fits to N_{ch} distribution

To study the features of the N_{ch} distributions they were fitted with the following functions. In the first method it is important to know the location of the maximum and slope of the $\log(N_{ch})$ distribution, so it was fitted with

$$f(x) = (e^{p_1 + p_2 \cdot x}) \cdot \frac{1 - \text{erf}(\frac{p_3 - x}{p_4})}{2}, \quad \text{where } x = \log_{10}(N_{ch})$$

(see Figure 4.25). For the second method it is important to find the location of the *upturn* feature (here located at $N_{ch} = N_{ms}$; ms stands for the point of maximum slope change) and evaluate quantities $Slope(N_{ms}) = -\frac{1}{f(N_{ch})} \cdot \frac{df(N_{ch})}{dN_{ch}}$ and normalization $Events = \int_{N_{ms}}^{N_{max}} f(x)dx$ at $N_{ch} = N_{ms}$. The N_{ch} distribution for data can be fitted with either $e^{p_1 + p_2 \cdot x} + e^{p_3 + p_4 \cdot x}$ (Figure 4.27) or

$$f(x) = (e^{p_1 + p_2 \cdot x} + e^{p_3 + p_4 \cdot x}) \cdot \frac{1 - \text{erf}(\frac{p_5 - x}{p_6})}{2}$$

(Figure 4.28). The second fit describes the behavior of N_{ch} distribution at low N_{ch} better and makes the fit independent of the small variations in the location of the fit region boundaries. As seen from
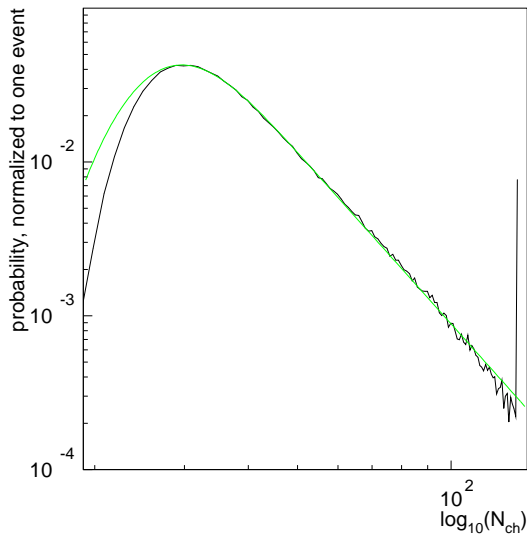
Figure 4.25: Fit to the N_{ch} distribution for small N_{ch}. Green smooth lines are fits to the jagged black histograms.
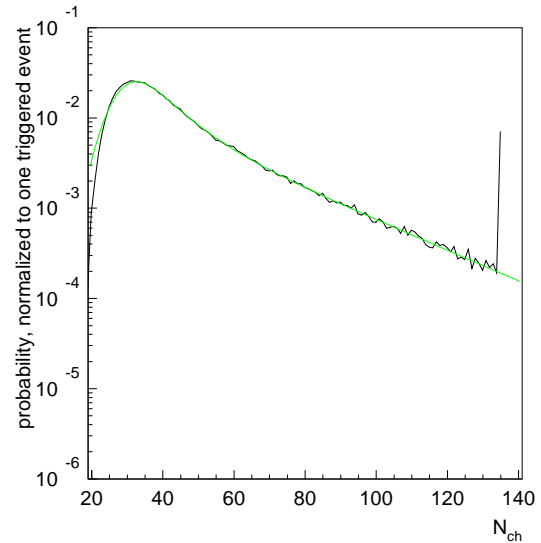
Figure 4.26: Fit to the N_{ch} distribution for OM 1. Green smooth lines are fits to the jagged black histograms.

Figure 4.29 both fits give equivalent results, since the behavior of the fits at and after the $N_{ch} = N_{ms}$ point is identical. The green dashed lines in the first 4 plots are the 4-parameter fits, and the blue solid lines are 6-parameter fits. In the last two plots both lines are for a 6-parameter fit, but the lines are computed using different numerical procedures. The fits can be done for the N_{ch} distribution associated with a layer of a particular optical module, e.g., OM 1, as seen in Figure 4.26.

4.5   Noise subtraction

The signal window contains on average four noise hits. The exponential fits can be easily adjusted to account for this. Consider an exponential distribution $P(n) = e^{a+b \cdot n}$ with parameters a and b, which are slowly varying functions of n, to which Poisson noise $\frac{\lambda^n}{n!} e^{-\lambda}$ (with $\lambda \approx 4$) is
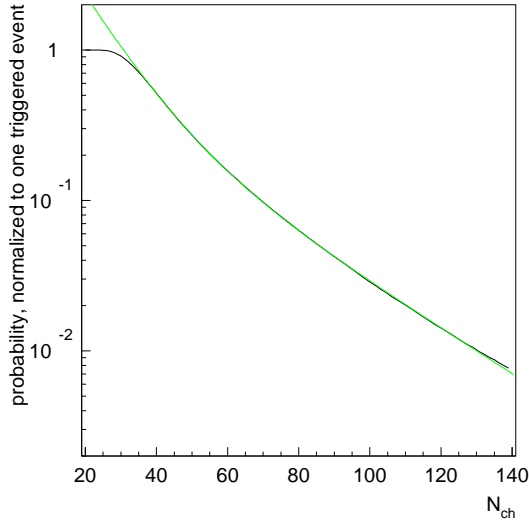
Figure 4.27: 4-parameter fit to N_{ch} distribution. Green smooth lines are fits to the jagged black histograms.
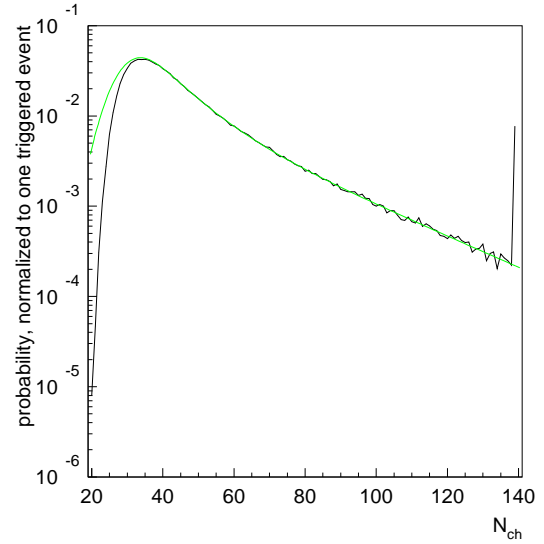
Figure 4.28: 6-parameter fit to N_{ch} distribution. Green smooth lines are fits to the jagged black histograms.

added. Then the total distribution is

$$P_{tot}(n) = \sum_{k=0}^{n} e^{a+b\cdot(n-k)} \frac{\lambda^k}{k!} e^{-\lambda}$$

$$= e^{a+b\cdot n} \sum_{k=0}^{n} \frac{(\lambda \cdot e^{-b})^k}{k!} e^{-\lambda \cdot e^{-b}} \frac{e^{-\lambda}}{e^{-\lambda \cdot e^{-b}}}$$

$$\approx e^{a+b\cdot n} e^{\lambda \cdot e^{-b} - \lambda} \sum_{k=0}^{\infty} \frac{\lambda'^k}{k!} e^{-\lambda'},$$

where $\lambda' = \lambda \cdot e^{-b}$ and n is sufficiently high ($n \gtrsim 40$). So,

$$P_{tot}(n) = e^{a'+b\cdot n} \quad \text{with} \quad a' = a + \lambda(e^{-b} - 1),$$

i.e., for the exponential fit the noise correction includes adding $\lambda(1 - e^{-b}) \approx -\lambda b$ (since $b \approx 0.1 \ll 1$) to the fitted value of a. For slowly varying a and b this correction varies from one point to another.

However,

$$P_{tot}(n) = e^{a'+b\cdot n} = e^{a-\lambda b+b\cdot n} = e^{a+b\cdot(n-\lambda)} = P(n - \lambda).$$

Therefore, it is sufficient to shift the fit by λ to accommodate the noise correction.
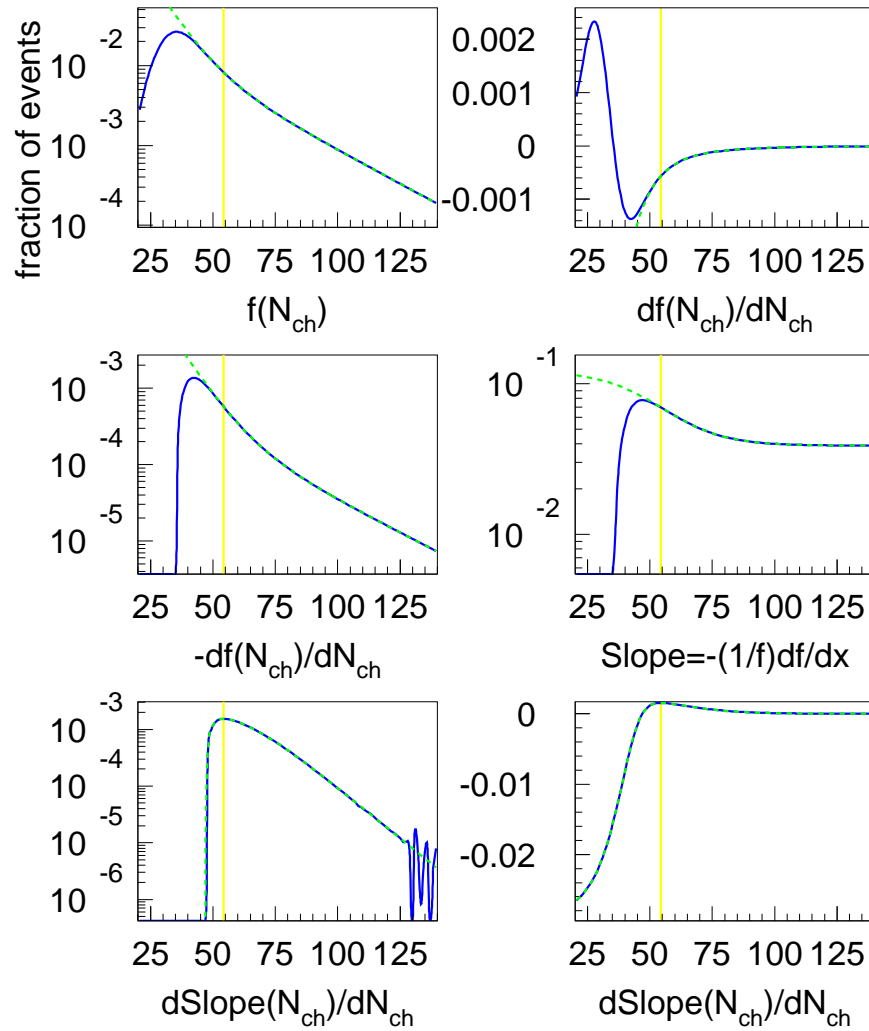
Figure 4.29: Point of maximum slope change rate (N_{ms})

4.6 Fits at smaller N_{ch}, the first method

- If it's not one problem, it's two -

The value of p_1 determines the N_{ch} normalization ($N_{ch} \propto \exp(p_1)$), and p_2 correlates with spectral index (since it determines the slope of the N_{ch} distribution). Figures 4.30-4.33 show depth profiles of the fit parameters p_1 through p_4. The simulated data are shown in different colors for different spectral indices ($2.56 - 2.96$), and the data are shown in black. The Monte Carlo data simulated with different ice parameters should lie close together for each spectral index to reduce the systematic errors caused by ice parameter uncertainties. Figures 4.30 and 4.31 do show some resolving power of the method, but it seems to be rather poor.

Compare Figures 4.30-4.31 with the prediction of the simple model of Section 4.2, Figures 4.9 and 4.10. Note that Figure 4.31 shows a change in slope, the slope after the maximum being taken with the minus sign, which is why the behavior of Figure 4.31 is inverted relative to that of Figure 4.10.

The maximum is broader for the data simulated with the full detector Monte Carlo than that just estimated from the muon energy loss plots of Section 4.2. The main reason for this is the stochastic nature of the OM signal: even if the muon energy lost in the vicinity of a certain OM were precisely known, the signal in that OM would follow a distribution which can be rather broad. Also, the OMs are not spread uniformly over the cylinder around the detector, but are located at a fixed set of points and can only see the signal from the photons emitted in some vicinity of those points. The N_{ch} distribution appears to have a fixed slope only to the left of the maximum, therefore the function fit to it was designed to only fit the location of the maximum and slope to the right of the maximum.

Nevertheless it appears that p_3 is correlated with both p_1 and p_2 and this can be used to bring the curves in the p_1 and p_2 plots closer together for each spectral index correction. Figures 4.34 and 4.36 show the correlation of p_1 and p_2 with p_3. Each plot shows seven sets of simulated data for five spectral indices. The data sets are shown in blue. Each set consists of points representing fits to N_{ch} at layers with -10 m $< z < 10$ m. The data are shown for the default detector configuration and several modified configurations (as described in Appendix E.2).

Two families of empirical parabolas were fitted to the p_1 vs. p_3 and p_2 vs. p_3 plots (Figures 4.34 and 4.36). Each simulated or real data point has a parabola associated with it (which goes through it). Minimum values of such parabolas define functions $f(p_1)$ and $f(p_2)$. As seen on Figures 4.35 and 4.37, the separation between simulated data curves corresponding to different values of spectral index is much better, i.e., the resolving power of the method is much improved.

Simulated data points at every z-layer in Figures 4.35 and 4.37 correspond to one of the spectral index corrections: $\gamma = 2.76 + (\gamma\text{-correction}) = 2.76 + 0.1 \cdot (0, \pm 1, \pm 2)$. These point groups are plotted vs. their respective spectral index correction (in units of 0.1), and linear functions are fitted through them (Figures 4.38 and 4.40). These functions are used to convert values at each z-layer to the "spectral index correction" units (again, multiplied by 10 for convenience). The resulting flattened plots are shown on Figures 4.39 and 4.41.
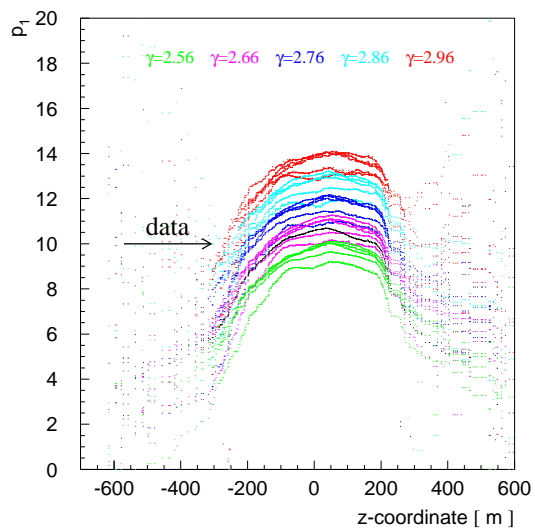
Figure 4.30: Fits to p_1
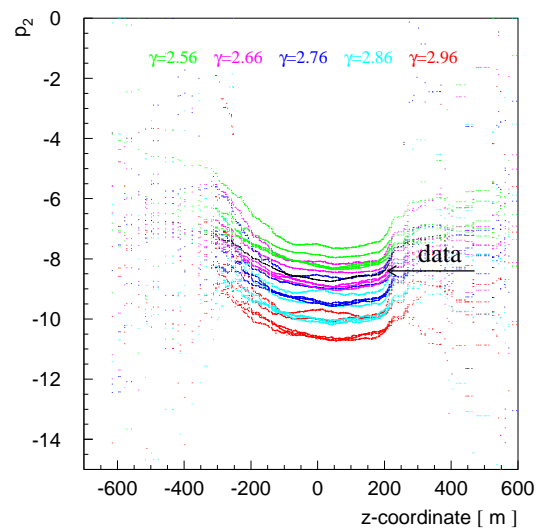
Figure 4.31: Fits to p_2
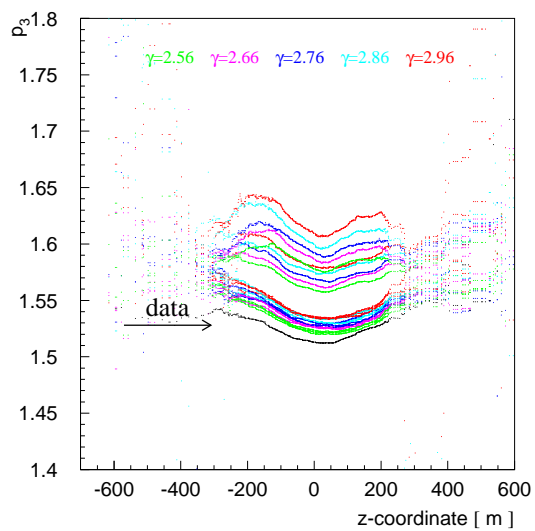
Figure 4.32: Fits to p_3
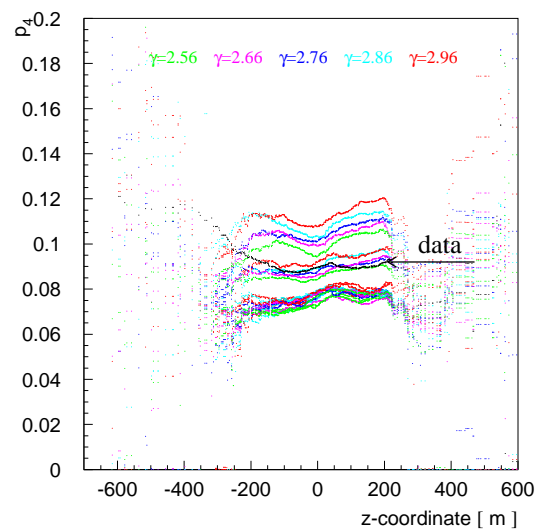
Figure 4.33: Fits to p_4
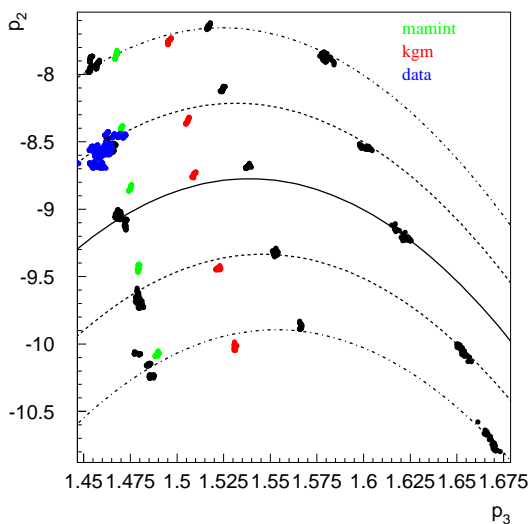
Figure 4.34: Correlation of p_2 with p_3
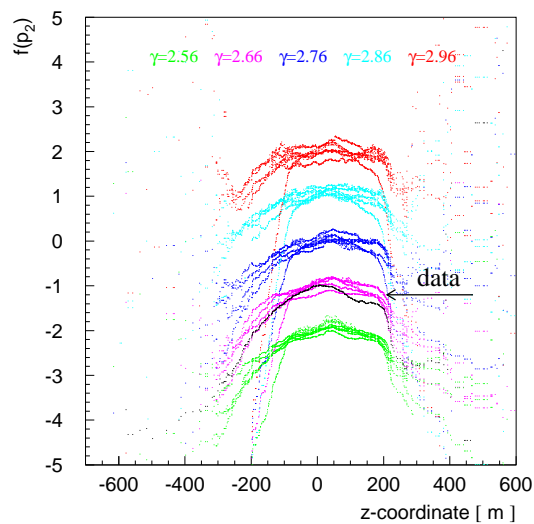
Figure 4.35: Spectral index separation
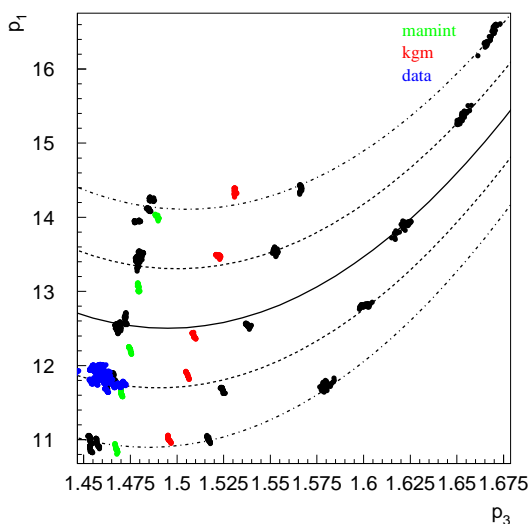
Figure 4.36: Correlation of p_1 with p_3
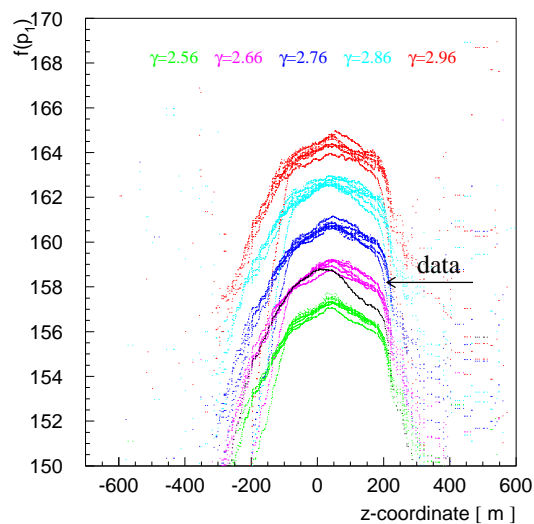
Figure 4.37: Normalization separation
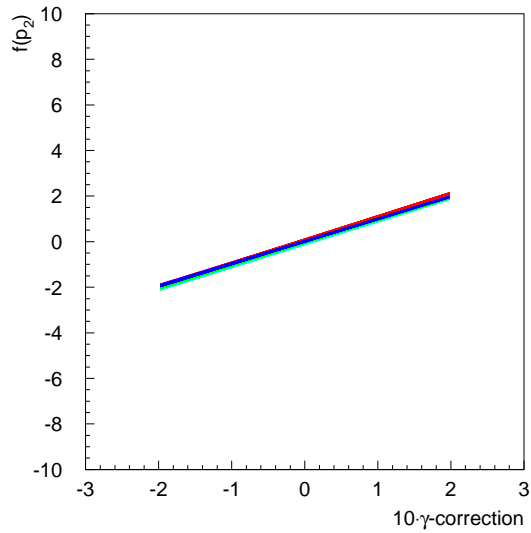
Figure 4.38: Spectral index correction: conversion function
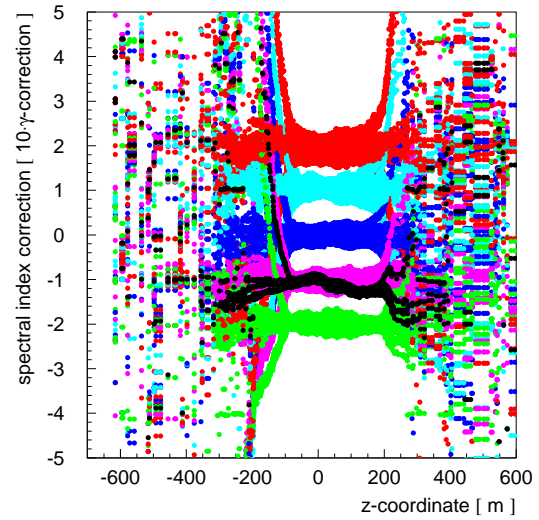
Figure 4.39: Spectral index correction: converted plots
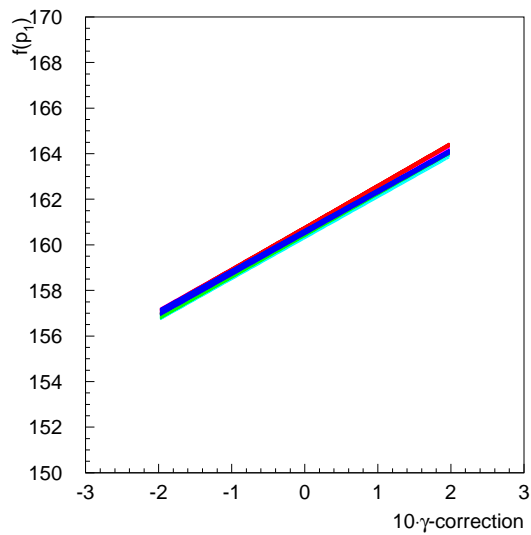
Figure 4.40: Normalization correction: conversion function
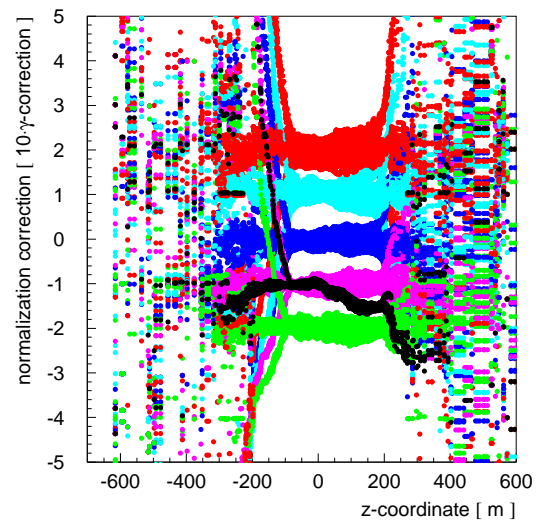
Figure 4.41: Normalization correction: converted plots
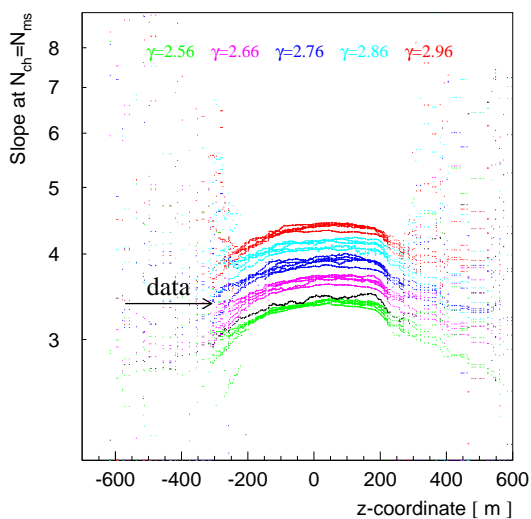
Figure 4.42: Slope of N_{ch} at N_{ms} for all events
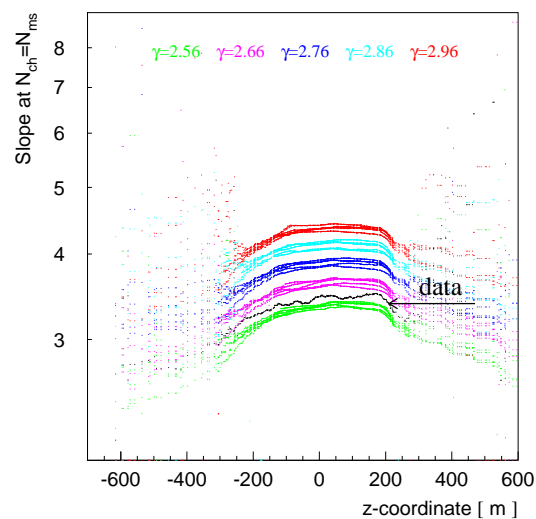
Figure 4.43: Slope of N_{ch} at N_{ms}, no noise events
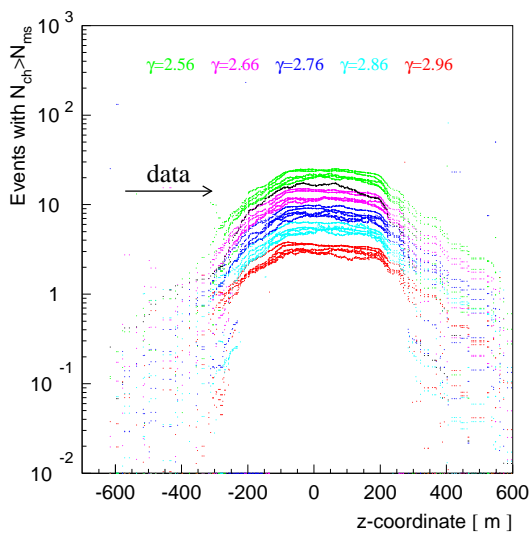
Figure 4.44: Number of events above N_{ms} for all events
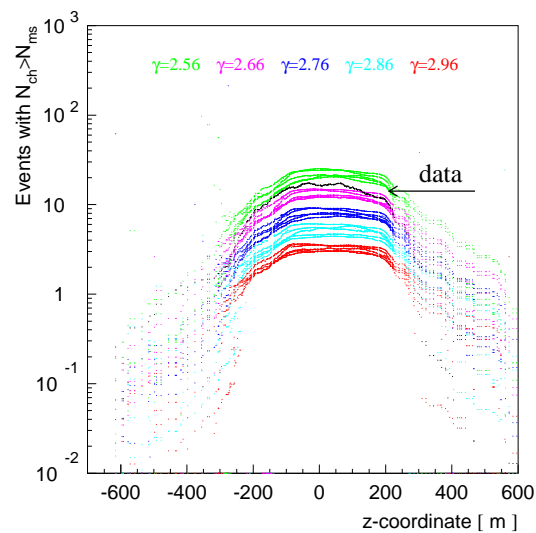
Figure 4.45: Number of events above N_{ms}, no noise events

4.7 Fits at higher N_{ch}, the second method

Figures 4.42-4.45 show the result of using the second method. One can clearly see that all ice models form groups well separated for different spectral index corrections. No extra parameter correlation correction was done (although these plots have also been converted to the "spectral index correction" coordinates). The data are shown in black and fall between the simulated data curves for $\gamma = 2.56$ and $\gamma = 2.66$. Also, plots with simulated data without noise hits are shown to demonstrate the power of the noise subtraction algorithm.

4.8 Results

The next subsections summarize the results of the application of the algorithms described in this section to year 2000 data collected by AMANDA-II. Five samples of data (each one 10 files long, or about 2 hours in detector time) from different seasons were analyzed: days 55, 91, 183, 275, and 298. Results were compared to Monte Carlo samples simulated for the same days (with atmosphere profiles taken from [28], as described in Section 2.2). The average of the resulting cosmic ray spectral index and normalization is calculated for final results, and the variance is taken as the uncertainty in our description or the atmospheric profile ("atm" below).

Each of the following four subsections contains four plots. The first one shows the result of analysis applied to the Monte Carlo samples (five of which were used for the fits employed by the algorithms; the two that were not used are *mamint* and *kgm*). The resolving power of the method is shown by the stability of the corrections found for each of the simulated data samples (they correspond to $0, \pm 1, \pm 2$ in the units of spectral index correction times 10 and should lie close to these values). The variance of all seven models around their default value is taken as the systematic

error caused by uncertainty in our knowledge of the ice parameters ("ice" below).

The second plot shows corrections found for different high-energy interaction models (these were calculated with only *mamint* and *kgm* ice models). The third plot shows corrections for different seasons, which were compared with data from different seasons to obtain the "atm" uncertainty as described above. Finally, the fourth plot shows the stability of the results with respect to the detector configuration changes (see Appendix E.2). The variance of points in this plot is taken as the detector configuration error (*conf* below).

When converting the points on the plots to the results listed in the following subsections please note that most of the Monte Carlo data points ware simulated for an October 1 atmosphere, while all of the data shown on the plots are for day 55 (March 27). As seen from the third plot in each set, an additional "seasonal" correction of $0.04 - 0.05$ needs to be applied to the results in the spectral index correction coordinates in order to match the March atmosphere of the data with the October atmosphere of the simulated data.

4.8.1 Results: 1st method, spectral index correction

Results are shown in Figures 4.46-4.49. For QGSJET, day 55,

$$\gamma = 2.76(\text{H}) - 0.063 \pm 0.007(\text{ice}) \pm 0.014(\text{atm}) \pm 0.009(\text{conf}) = 2.70 \pm 0.02.$$

4.8.2 Results: 1st method, normalization correction

Results are shown in Figures 4.50-4.53. For QGSJET,

$$\Phi_0 = 0.1057(\text{H}) \cdot 10^{\log_{10}(e) \cdot 1.75(\text{conversion slope}) \cdot (-0.001 \pm 0.009(\text{ice}) \pm 0.023(\text{atm}) \pm 0.029(\text{conf}))},$$

$$\Phi_0 = 0.1057(\text{H}) - 0.000 \pm 0.002(\text{ice}) \pm 0.004(\text{atm}) \pm 0.006(\text{conf}) = 0.106 \pm 0.007.$$

4.8.3 Results: 2nd method, spectral index correction

Results are shown in Figures 4.54-4.57. For QGSJET,

$$\gamma = 2.76(\text{H}) - 0.162 \pm 0.017(\text{ice}) \pm 0.016(\text{atm}) \pm 0.006(\text{conf}) = 2.60 \pm 0.02.$$

4.8.4 Results: 2nd method, normalization correction

Results are shown in Figures 4.58-4.61. For QGSJET,

$$\Phi_0 = 0.1057(\text{H}) \cdot 10^{-0.19(\text{conversion slope}) \cdot (0.43 \pm 0.17(\text{ice}) \pm 0.13(\text{atm}) \pm 0.16(\text{conf}))},$$

$$\Phi_0 = 0.1057(\text{H}) - 0.018 \pm 0.006(\text{ice}) \pm 0.005(\text{atm}) \pm 0.006(\text{conf}) = 0.088 \pm 0.010.$$
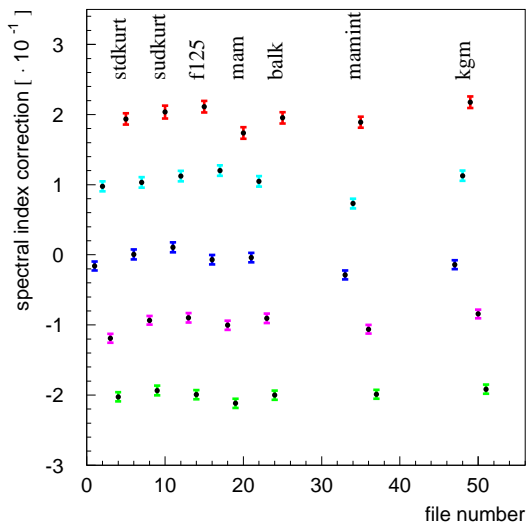
Spectral index correction by 1st method

Figure 4.46: different ice models   Figure 4.47: different interaction models
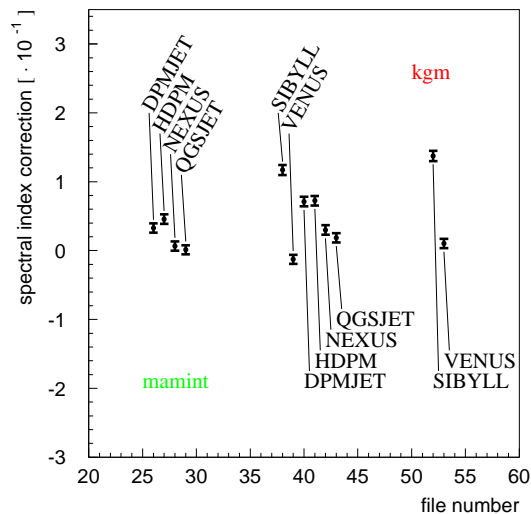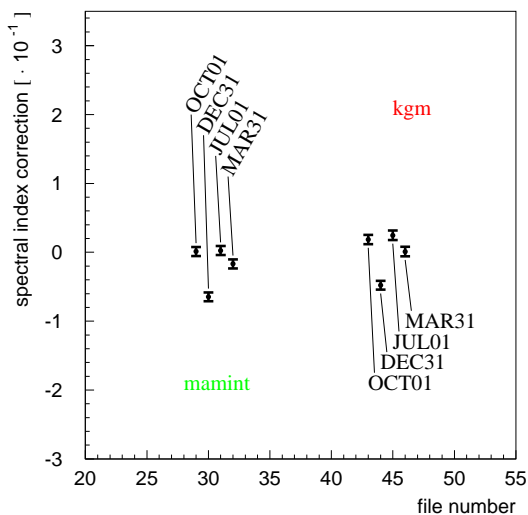
Spectral index correction by 1st method

Figure 4.48: different seasons   Figure 4.49: different detector configurations
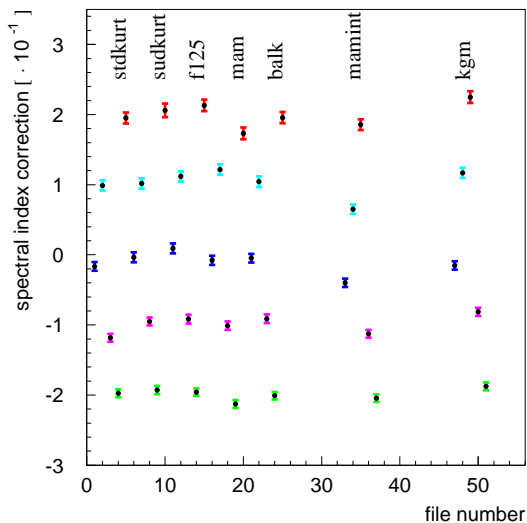
Normalization correction by 1st method

Figure 4.50: different ice models
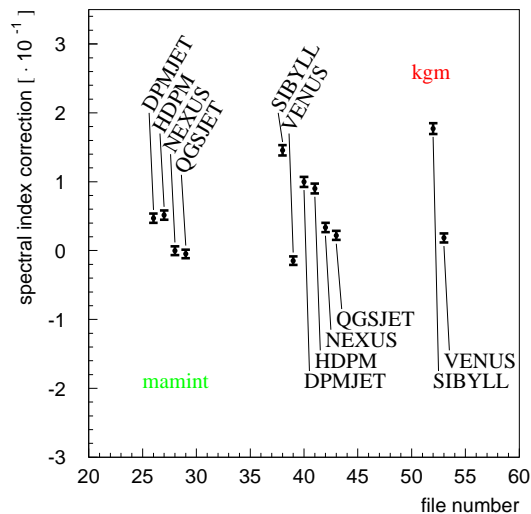
Figure 4.51: different interaction models
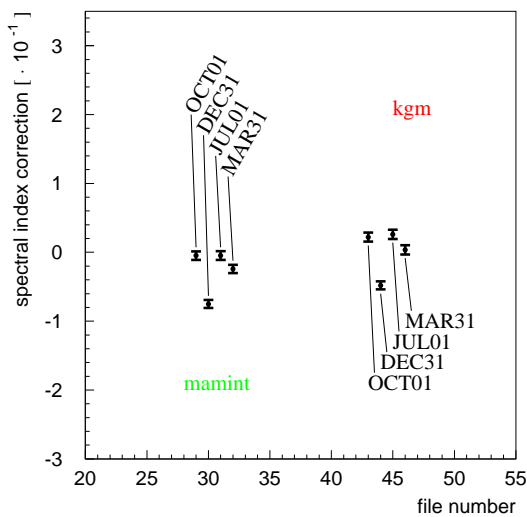
Normalization correction by 1st method

Figure 4.52: different seasons
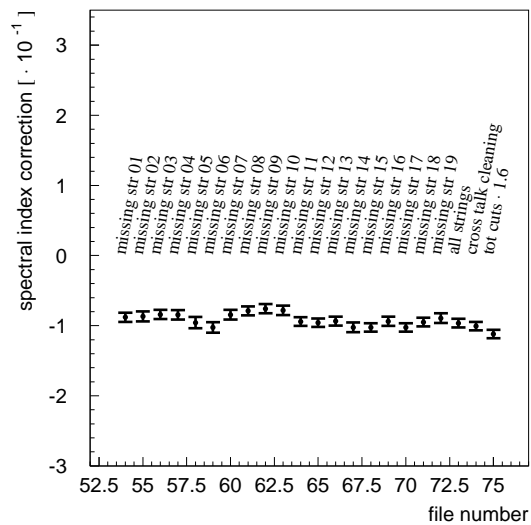
Figure 4.53: different detector configurations
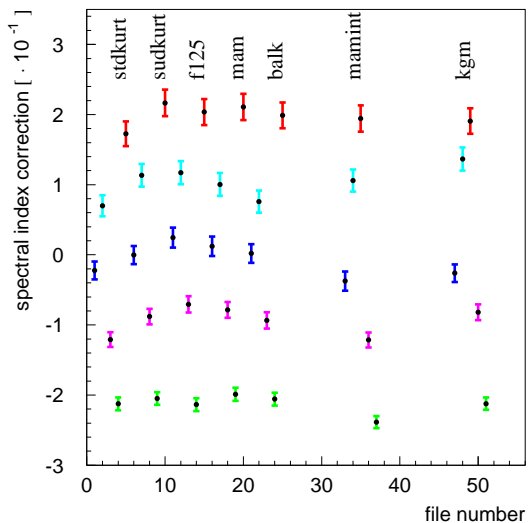
Spectral index correction by 2nd method

Figure 4.54: different ice models
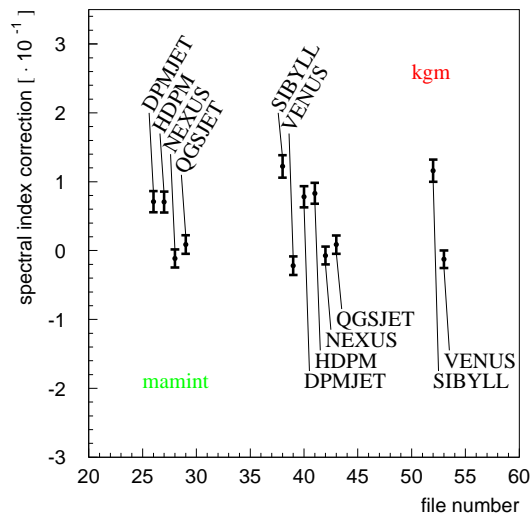
Figure 4.55: different interaction models
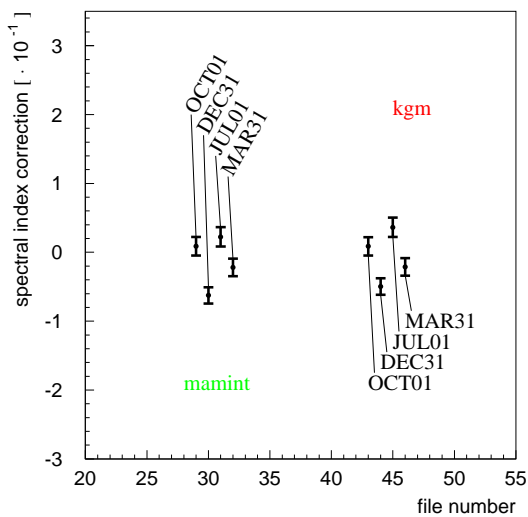
Spectral index correction by 2nd method

Figure 4.56: different seasons
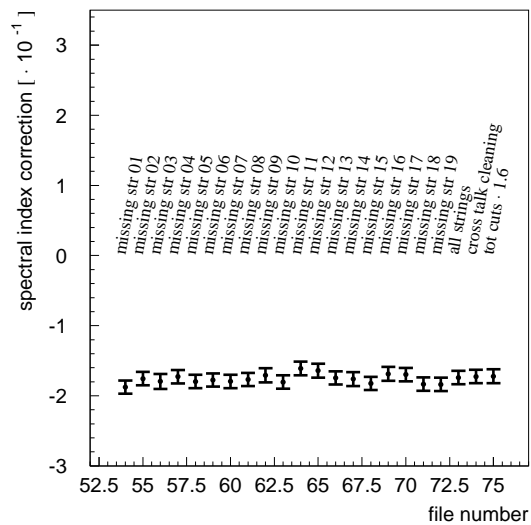
Figure 4.57: different detector configurations
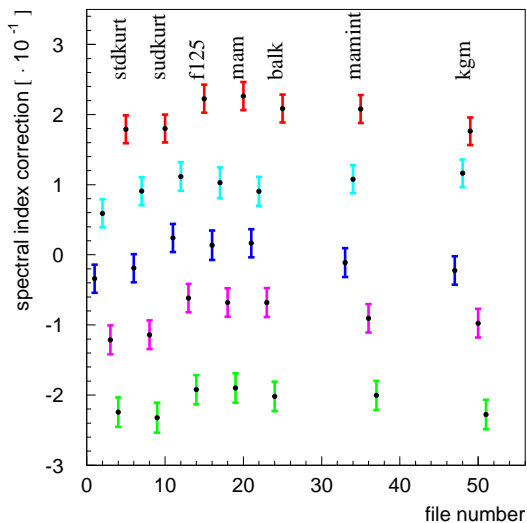
Normalization correction by 2nd method

Figure 4.58: different ice models
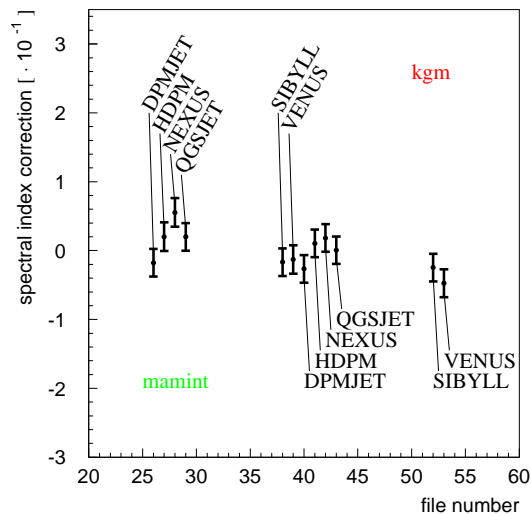
Figure 4.59: different interaction models
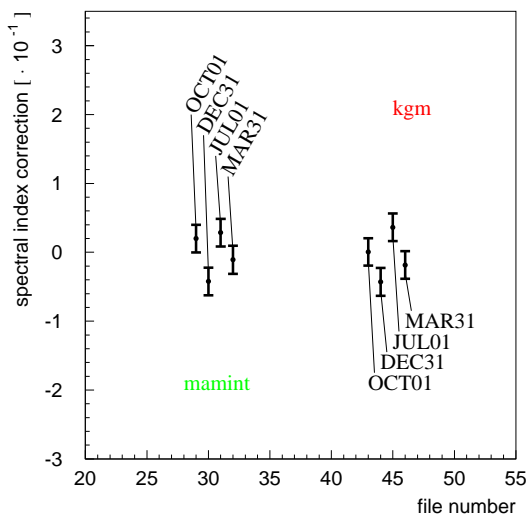
Normalization correction by 2nd method

Figure 4.60: different seasons
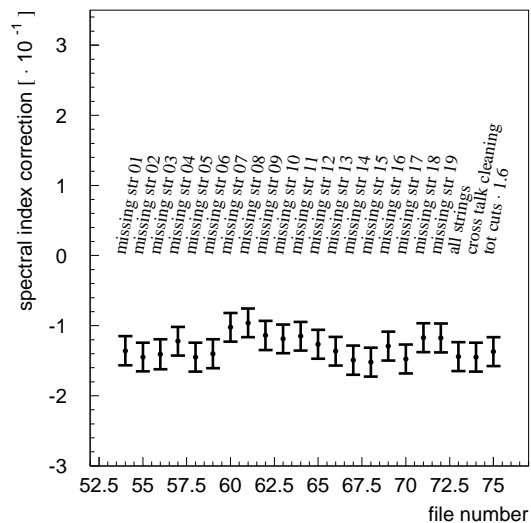
Figure 4.61: different detector configurations

Chapter 5

Results

- From inception to deception in less than 100 pages -

5.1 Results of cosmic ray flux measurement

As seen from Section 4.8, the dependence of the developed method on ice parameters or detector configuration is very weak. Cosmic ray flux corrections for both spectral index and normalization are obtained. For QGSGET,

$$\gamma = 2.76(\text{H}) - 0.063 \pm 0.007(\text{ice}) \pm 0.014(\text{atm}) \pm 0.009(\text{conf}) = 2.70 \pm 0.02,$$

$$\Phi_0 = 0.1057(\text{H}) + 0.000 \pm 0.002(\text{ice}) \pm 0.004(\text{atm}) \pm 0.006(\text{conf}) = 0.106 \pm 0.007.$$

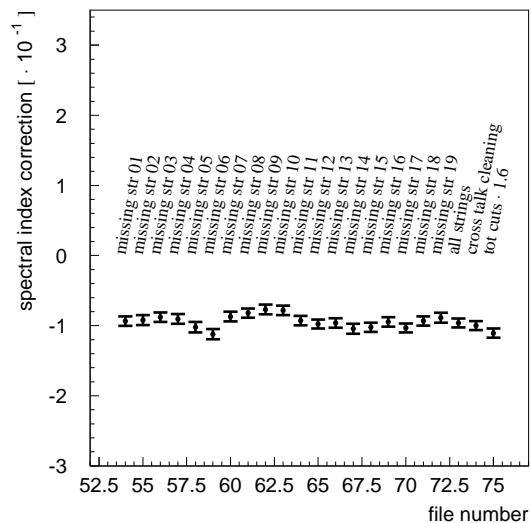Please note that the corrections above should be applied to all components of the cosmic rays, from H to Fe, as used in the simulation (starting with the values in A.1); here only the values for the H component are shown.

Figure 5.3 shows integrated cosmic ray spectrum functions calculated using the values of γ and Φ_0 presented in Figures 5.1 and 5.2. As seen from Figure 5.4, the minimum variance between
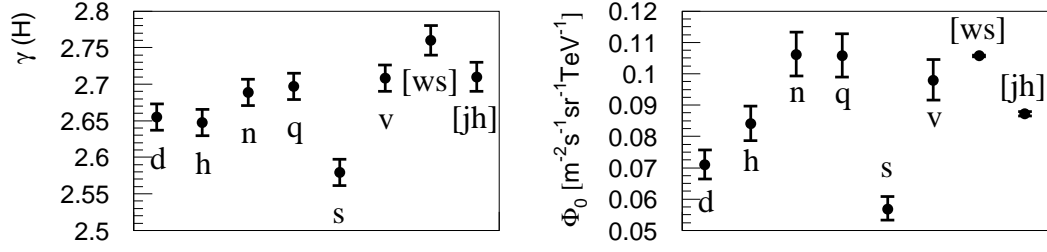
Figure 5.1: Results of the 1st method
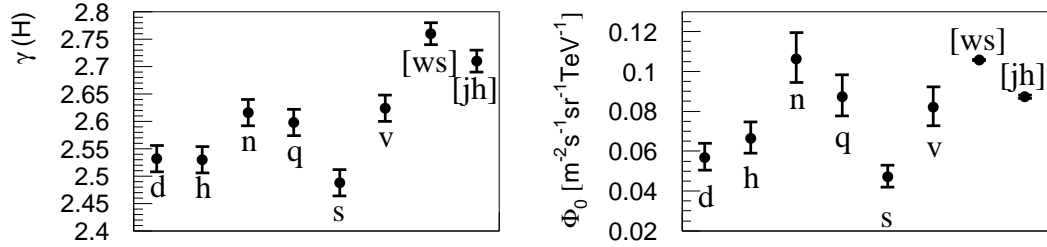
Figure 5.2: Results of the 2nd method

Shown are results for high-energy models (left to right): DPMJET, HDPM, NEXUS, QGSJET,

SIBYLL, VENUS, and also values from references [1] (Wiebel-Sooth) and [13] (Jörg Hörandel)
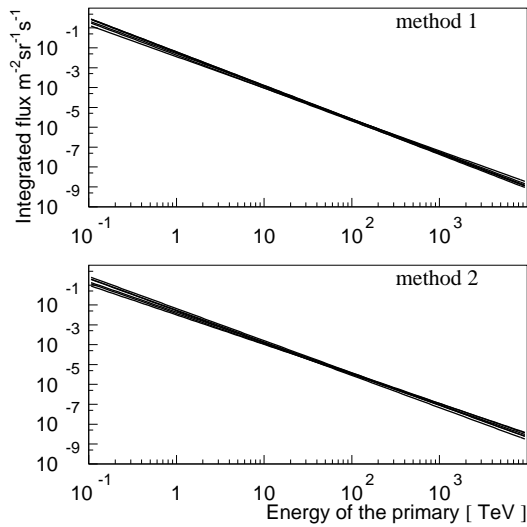
Figure 5.3: Cosmic ray spectrum, as determined in this work
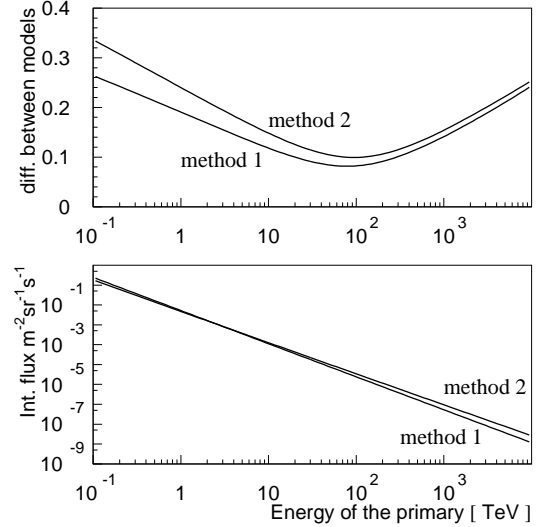
Figure 5.4: Variance between different high energy models

high-energy interaction models is achieved at ~ 100 TeV, which is one order of magnitude above

the energy of maximum AMANDA-II sensitivity to primaries (see Section 5.3, still quite sensitive,

though, as seen from Figure 5.15). Also, the average spectra obtained with method 1 and 2 are

shown.

5.2   Muon flux calculation

To calculate the muon flux at the ice surface the spectral index and normalization summa-

rized in the previous section were fed to a CORSIKA simulation and the results were fitted with the

Gaisser formula [5]

$$
\frac{dN}{dE} = 0.14 \text{ cm}^{-2}\text{sr}^{-1}\text{s}^{-1}\text{GeV}^{-1} \cdot A \cdot \left(\frac{E_\mu}{\text{GeV}}\right)^{-\gamma} \cdot \left(\frac{1}{1 + \frac{1.1 E_\mu \cos\theta}{115 \text{ GeV}}} + \frac{0.054}{1 + \frac{1.1 E_\mu \cos\theta}{850 \text{ GeV}}}\right)
$$

in the range of zenith angles $0° < \theta < 70°$ (to avoid θ transformation at large zenith angles, [73]).

The fits work very well, and the majority of results show $\chi_\nu^2 \approx 1$. Results are summarized in Table

5.1. Figures 5.5-5.7 show some of the fits used for the results in this table. Figure 5.8 also shows a

fit to the muon spectrum with only the maximum energy muon taken from each event (not shown in

Table 5.1).

Table 5.1: Muon energy spectrum results

$10^3 - 10^5$ TeV energy range				$600 - 6 \cdot 10^4$ TeV energy range			
int. model	A	γ	χ_ν^2	int. model	A	γ	χ_ν^2
qgsjet	0.613	2.662	1.08	qgsjet	0.612	2.662	1.24
sibyll	0.237	2.530	1.21	sibyll	0.230	2.525	2.42
hdpm	0.397	2.602	1.05	hdpm	0.416	2.608	1.08
venus	0.640	2.671	1.09	venus	0.635	2.670	1.15
dpmjet	0.373	2.598	1.00	dpmjet	0.365	2.595	1.03
nexus	0.602	2.660	1.05	nexus	0.595	2.659	1.08
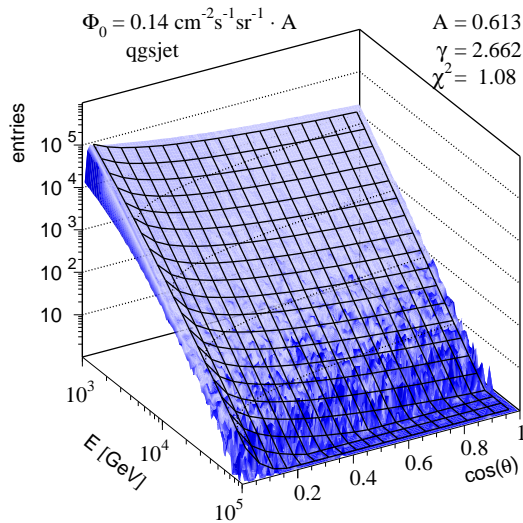
Fits to muon spectra at the surface

Figure 5.5: QGSJET model, $1 - 100$ TeV
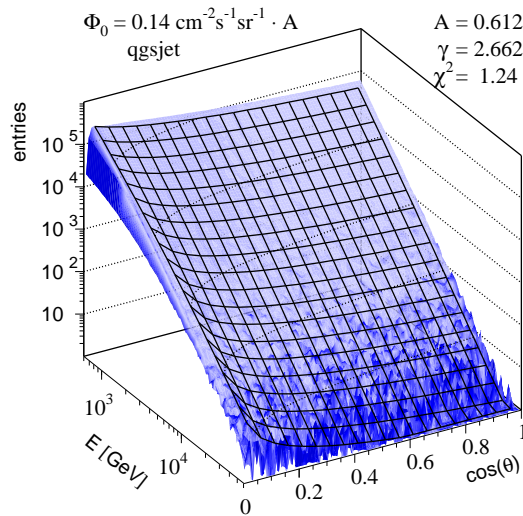
Figure 5.6: QGSJET model, $0.6 - 60$ TeV
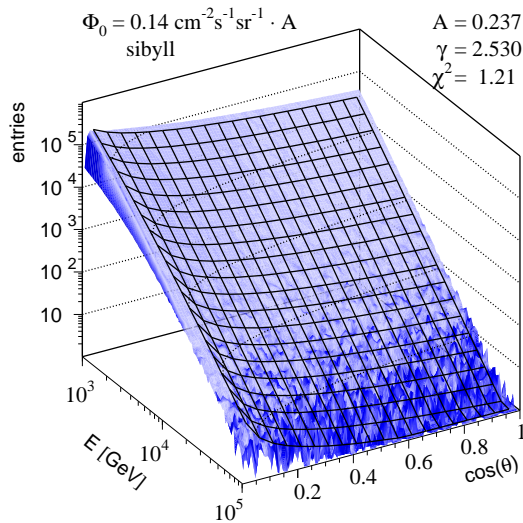
Fits to muon spectra at the surface

Figure 5.7: SIBYLL model, $1 - 100$ TeV, all bundle muons
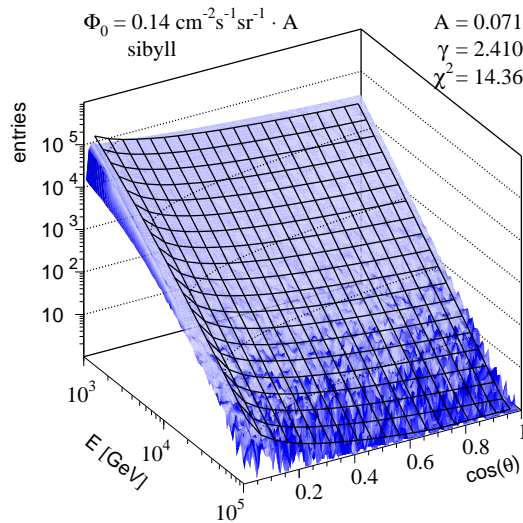
Figure 5.8: SIBYLL model, $1 - 100$ TeV, only maximum energy muons

Figure 5.9 shows a comparison of the *muon fluxsum* $A \cdot E^{-\gamma}$ with the parameters A and γ from Table 5.1. Also the variance between the high-energy interaction models is shown. It appears to have a minimum of 2% at ~ 1 TeV, which is the energy of the maximum sensitivity of the AMANDA-II detector to muons (see Section 5.3). Therefore it makes sense to compare results for the muon (e.g., vertical) flux at 1 TeV. Figure 5.10 shows the spectral indices and muon vertical fluxes found at 1 TeV for all six high-energy interaction models. Assuming a systematic error of 2% between high-energy interaction models, it is possible to present a muon flux result which is independent of the high-energy interaction model:

muon vertical flux at 1 TeV $= (1.05 \pm 0.02(\text{ice}) \pm 0.04(\text{atm}) \pm 0.06(\text{conf}) \pm 0.02(\text{HE int. model})) =$

$$(1.05 \pm 0.07) \cdot 10^{-10} \text{ cm}^{-2}\text{sr}^{-1}\text{s}^{-1}\text{GeV}^{-1} \quad \text{(at the South Pole)}.$$

A similar result is obtained for the 2nd method (see Figures 5.11 and 5.12):

muon vertical flux at 1 TeV $= (1.21 \pm 0.09(\text{ice}) \pm 0.07(\text{atm}) \pm 0.09(\text{conf}) \pm 0.03(\text{HE int. model})) =$

$$(1.21 \pm 0.15) \cdot 10^{-10} \text{ cm}^{-2}\text{sr}^{-1}\text{s}^{-1}\text{GeV}^{-1} \quad \text{(at the South Pole)}.$$
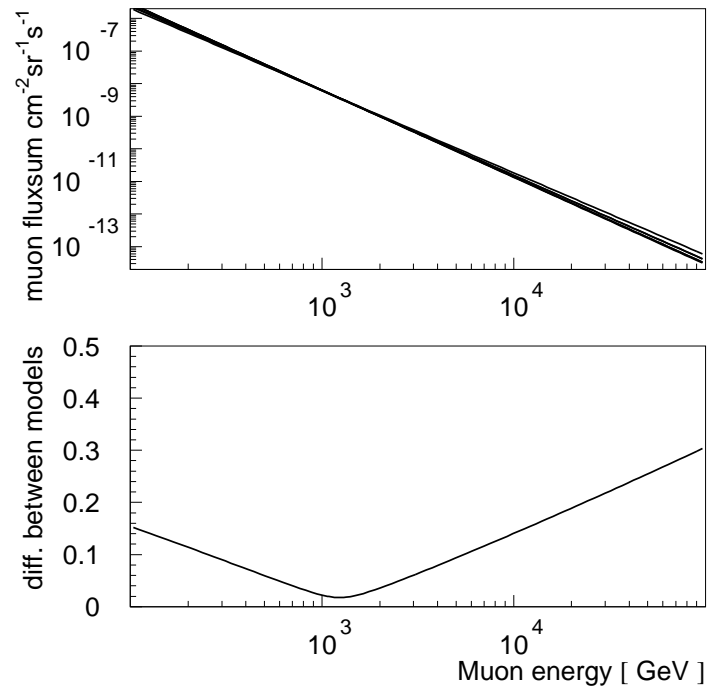
Figure 5.9: Muon *fluxsum* $A \cdot E^{-\gamma}$ for 6 high-energy models and variance between them, 1st method
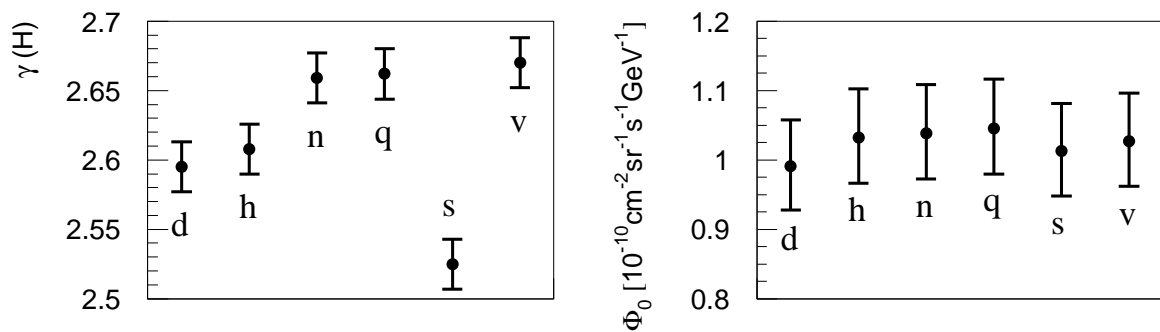
Figure 5.10: Results of the 1st method: muon spectral index and flux at 1 TeV. Shown are results for high-energy models (left to right): DPMJET, HDPM, NEXUS, QGSJET, SIBYLL, and VENUS
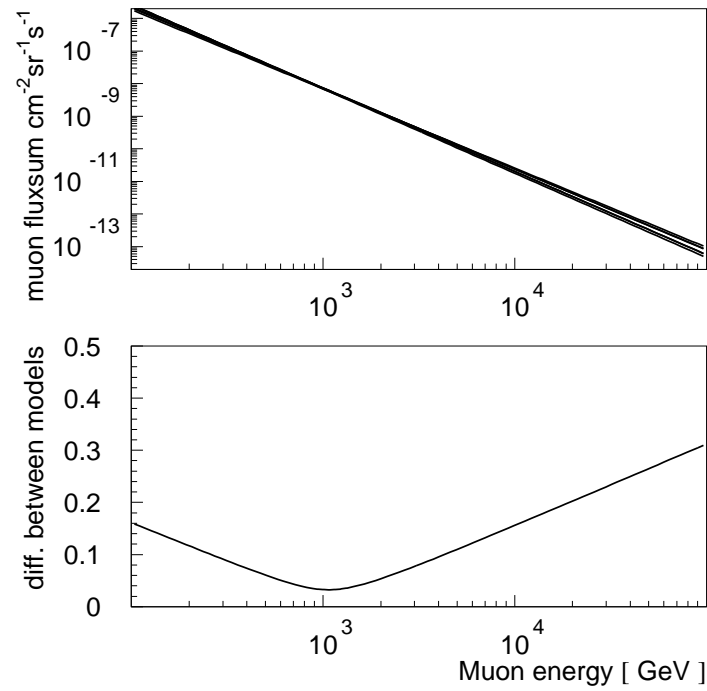
Figure 5.11: Muon *fluxsum* $A \cdot E^{-\gamma}$ for 6 high-energy models and variance between them, 2nd method
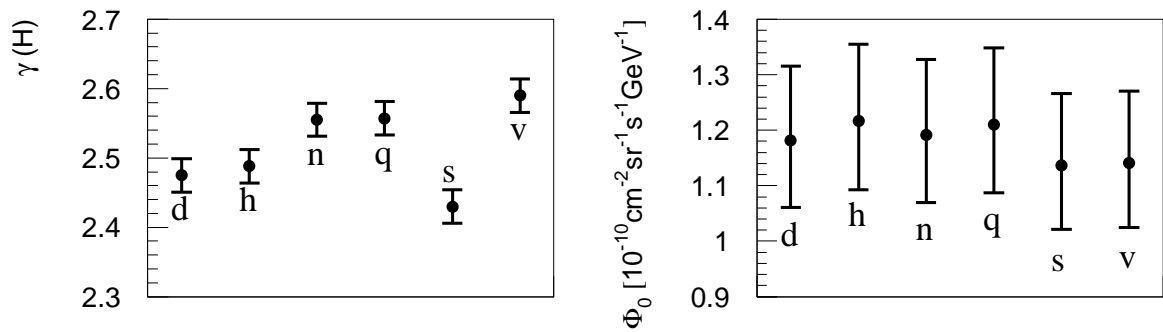
Figure 5.12: Results of the 2nd method: muon spectral index and flux at 1 TeV. Shown are results for high-energy models (left to right): DPMJET, HDPM, NEXUS, QGSJET, SIBYLL, and VENUS

5.3 Range of energies of applicability of results

Figure 5.13 shows the distribution of energies of primaries and muons observed by AMANDA-II. The majority of signal comes from muons with energies ~ 1 TeV produced in the showers generated by primaries with energies ~ 10 TeV. Figures 5.14 and 5.15 show these distributions vs. the number of hit channels N_{ch} in the AMANDA-II events. These distributions don't have a strong dependence on the number of observed hit channels, i.e., both methods (1 and 2), which depend on different N_{ch} ranges ($\sim 35 - 45$ and $\sim 55 - 65$), also have maximum resolution at energies of ~ 10 TeV for the primary and 1 TeV for the main muon[1].

5.4 Discussion

All high-energy interaction models have been tested to give similar results at the ice surface. To explain the observed difference between them in the simulated data of AMANDA-II, and also the difference in results obtained by methods 1 and 2, it is useful to define the *observed muon multiplicity*, which is the number of muons per event which have produced at least one hit in the AMANDA-II OMs during the applicable trigger window. Figures 5.16 and 5.17 show the distribution of muon energies vs. observed muon multiplicities. A sizable fraction ($\sim 50\%$) of events contain signal from Cherenkov photons produced by multiple muons. The energy distribution of the main muons in multi-muon events is similar to that in single muon events. Therefore multi-muon events produce a signal which consists of a part similar to the signal of a single muon event, plus more hits from extra muons, e.g., multi-muon events should produce brighter events and somewhat flatten the N_{ch} distribution. As seen from Figure 5.20, multi-muon events do produce a flatter N_{ch}

---

[1] The highest energy muon in the bundle.
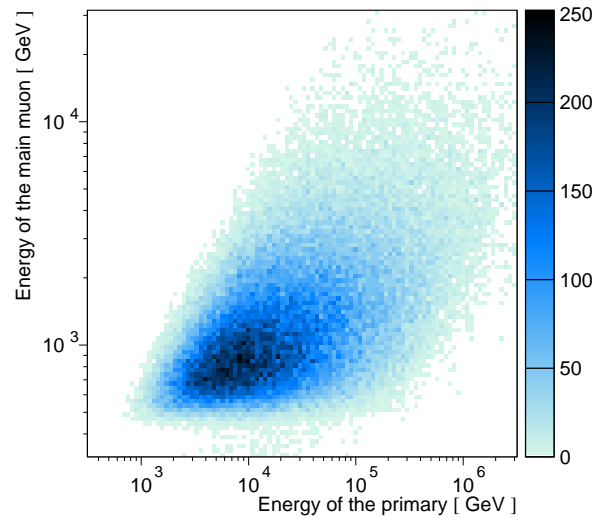
Figure 5.13: Energy of the main muon observed by AMANDA-II vs. energy of the primary
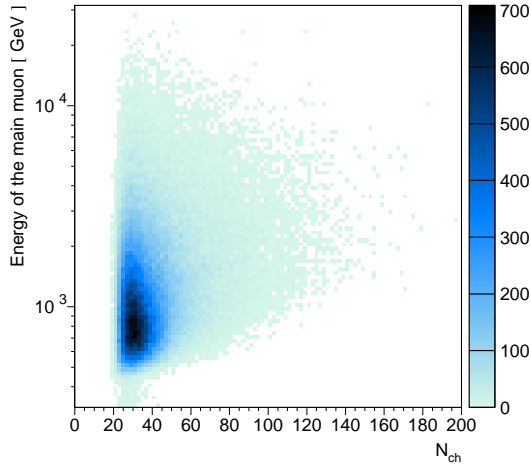
Figure 5.14: Energy of the main muon observed by AMANDA-II vs. N_{ch}
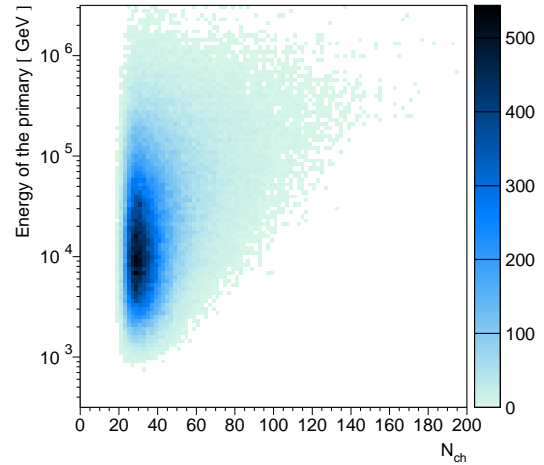
Figure 5.15: Energy of the primary vs. N_{ch}
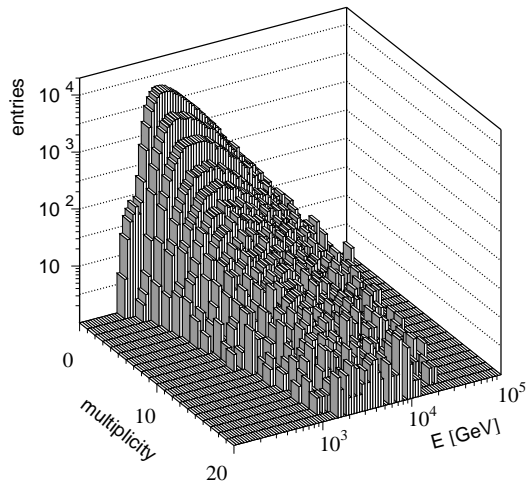
Figure 5.16: Energy of the main muon on the ice surface vs. observed muon multiplicity
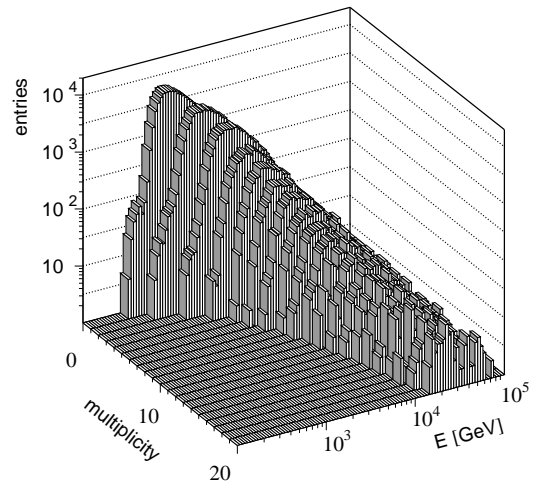
Figure 5.17: Total muon energy on the ice surface vs. observed muon multiplicity
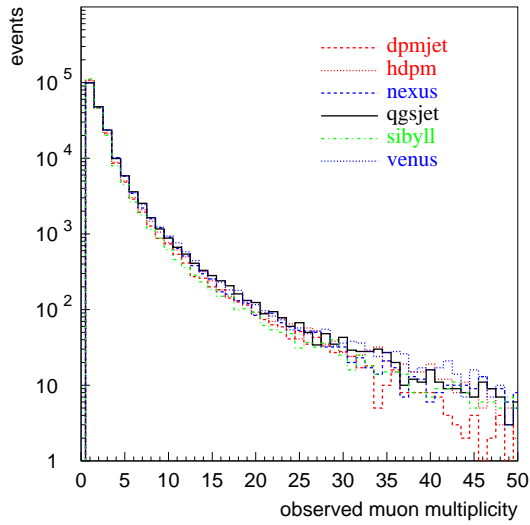
Figure 5.18: Observed muon multiplicity for different high-energy interaction models
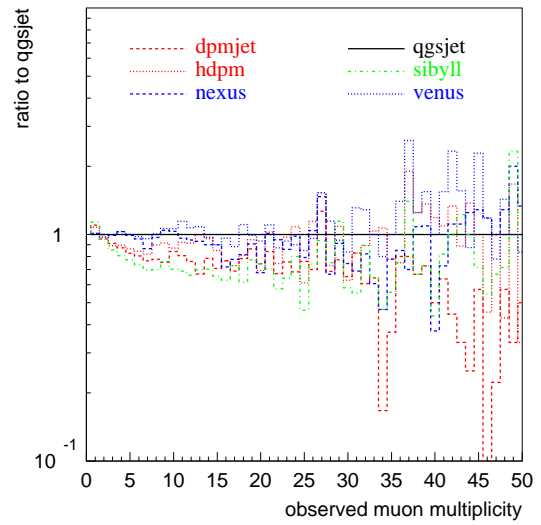
Figure 5.19: Observed muon multiplicity normalized to QGSJET model
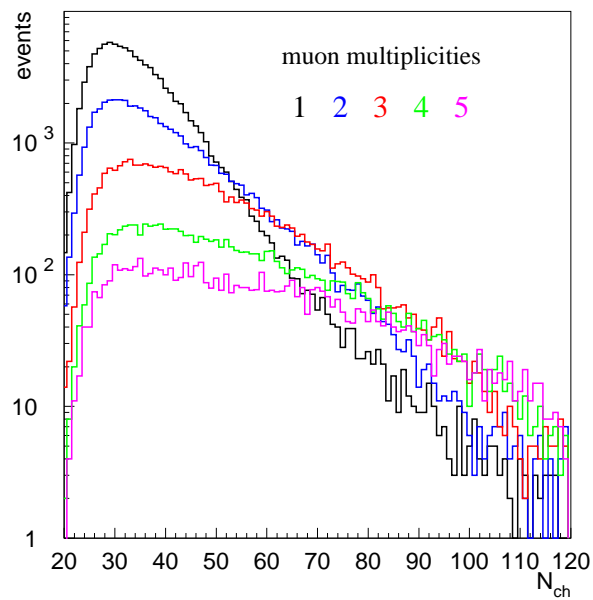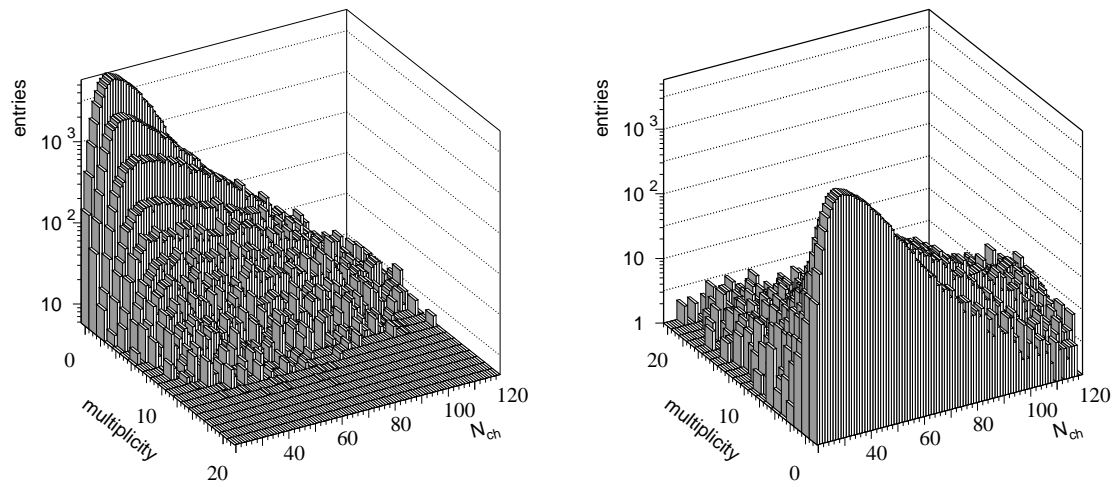
Figure 5.20: Observed muon multiplicity vs. N_{ch}

distribution. Although the location of the maximum appears not to change significantly between N_{ch} distributions corresponding to different observed muon multiplicities, the slope after the maximum (important for the first method) and the location of the *upturn* feature and rate of slope change (important for the second method) do vary quite a bit. As seen from Figures 5.18 and 5.19 the fraction of events with observed number of muons more than one is quite different between the models. In fact, the models are grouped in the same way as in their corresponding spectral index which fits the AMANDA-II data: QGSJET, NEXUS, and VENUS have almost idential fractions, DPMJET and HDPM have lower fractions, and SIBYLL has the lowest fraction of multi-muon events.

5.5 Comparison with other experiments

The results of this work are consistent with those from other experiments and with theoretical predictions (see Figures 1.1 and 5.21). The cosmic ray flux in the region of energies where AMANDA-II is sensitive is unaffected by the solar wind or the Earth's magnetic field, and is therefore independent of the geographical location where the measurement is done and can be directly compared to the other experiments. When the muon flux of this work is recalculated for a standard US atmosphere, one obtains a slightly higher flux of $(1.09 \pm 0.07) \cdot 10^{-10}$ cm^{-2}sr^{-1}s^{-1}GeV^{-1} at 1 TeV, than at the South Pole. Although the results of the 1st and 2nd methods for the muon flux at 1 TeV are compatible with each other, only the result of the 1st method is quoted here for reasons mentioned in the previous section (also because it can be quoted with smaller errors).
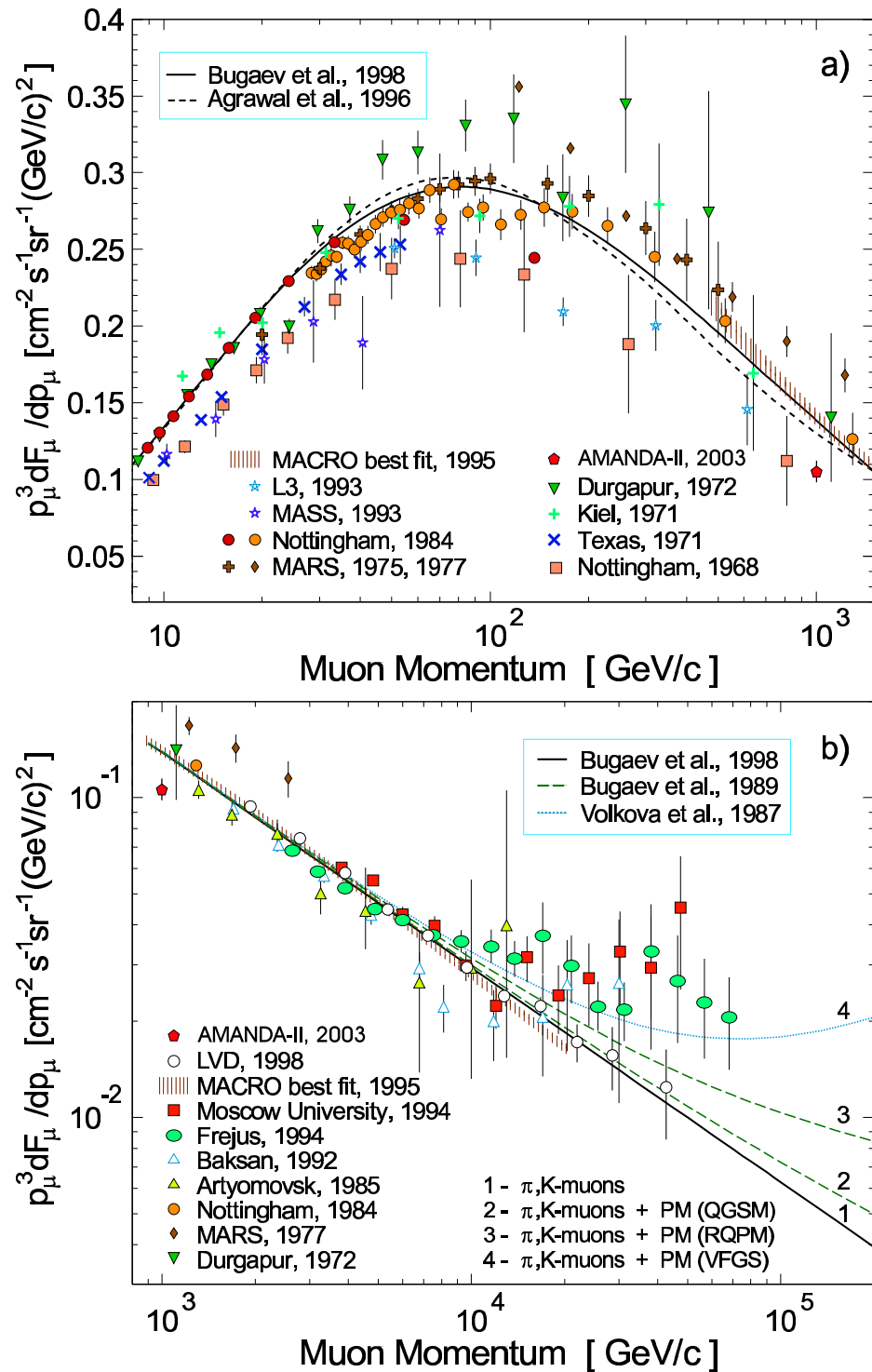
Figure 5.21: Comparison of the measured muon flux with the results of other experiments; figure adapted from [74]

Chapter 6

Conclusions

- Self-deception report -

The downgoing muon simulation was substantially improved by using the extensive air shower generator CORSIKA to describe the shower development in the atmosphere, and by writing a new software package for muon propagation (MMC), which reduced computational and algorithm errors below the level of uncertainties of the muon cross sections in ice. CORSIKA improved the description of shower generation and allowed us to use several different high-energy interaction models, and MMC reduced shower muon propagation errors to just 1%.

A method developed in this work appears to produce cosmic ray and muon flux values which depend only weakly on ice parameters and detector configuration. Starting with the primary abundances given in [1] (Appendix A), cosmic ray flux corrections for both spectral index and normalization are obtained. Results of different high-energy interaction models are compared with data from [1, 13] in Figure 5.1. For QGSJET, $\gamma = 2.70 \pm 0.02$ and $\Phi_0 = 0.106 \pm 0.007 \, \text{m}^{-2}\text{sr}^{-1}\text{s}^{-1}\text{TeV}^{-1}$ (for the H component). The cosmic ray flux, summed over all components (H, ...,Fe) in the region of energies where AMANDA-II is most sensitive, is shown in Figure

1.1 with a blue solid line.

The muon spectral index depends on the interaction model and is 2.66 ± 0.02 for QGSJET. The muon flux at 1 TeV appears to be independent of the high-energy interaction model and for vertical muons is $(1.05 \pm 0.07) \cdot 10^{-10} \text{ cm}^{-2}\text{sr}^{-1}\text{s}^{-1}\text{GeV}^{-1}$ (at the location of the South Pole). This value can be compared with that from the other experiments in Figure 5.21.

QGSJET, VENUS, and NEXUS produce similar results which agree best with those from other experiments and theoretical expectations, but QGSJET is by far the fastest code (also faster than the other three models).

It appears that insufficient accuracy in the description of the multi-muon events is the likely cause for disagreement between high-energy interaction models.

Bibliography

[1] Wiebel-Sooth, B. & Biermann, P.L. 1999, Landolt-Bornstein, vol. VI/3c, Springer Verlag, p37 − 90

[2] Fermi, E. (1949), Phys. Rev. 75, 1169

[3] Bell, A. R. (1978), Mon. Not. R. Astr. Soc. 182, 147 and 443

[4] Longair, M. S. (1981) High Energy Astrophysics, Cambridge University Press

[5] Gaisser, T.K. 1990, Cosmic Rays and Particle Physics, Cambridge

[6] Gupta, M., & Webber, W. R. (1989), Ap. J. 340, 1124

[7] U. of Chicago, website: http://astroparticle.uchicago.edu

[8] Morse, R., Neutrino Astronomy: First Light - Using the South Pole Ice Cap, Talk given at "Astrophysics from Antarctica" in Chicago, July 1997, AMANDA internal report 19980502

[9] Jacobsen, J. E., Simulating the detection of muons and neutrinos in deep antarctic ice, 1996, Ph.D. thesis, U. of Wisconsin-Madison

[10] Gaisser, T.K., Halzen, F., & Stanev, T. 1995, Phys. Rep. 258, 173

[11] Halzen, F., Proc. 26th ICRC (Salt Lake City, 1999)

[12] Andres, E., et al., AMANDA Collaboration, 22 Mar 2001, Nature 410, $441 - 443$

[13] Hörandel, J., Astropart. Phys. 19 (2003) 193

[14] http://www.ngdc.noaa.gov/stp/SOLAR/COSMIC_RAYS/cosmic.html

[15] Chirkin, D., & Rhode, W., 26th ICRC, HE.3.1.07, Salt Lake City, 1999

[16] Chirkin, D., & Rhode, W., 27th ICRC, HE 220, Hamburg, 2001

[17] Hundertmark, S., DESY-PROC-1999-1, 276, 1999

[18] Rhode, W., & Cârloganu, C., DESY-PROC-1999-01, 1999

[19] Chirkin, D., & Rhode, W., Proceedings of 2nd Workshop on Methodical Aspects of Underwater/Underice Neutrino Telescopes, Hamburg, 2001

[20] Wiebusch, C., Muon Energy Reconstruction with AMANDA, AMANDA manuscript No 19990701, http://amanda.berkeley.edu/manuscripts/

[21] Miocinovic, P., Muon Energy Reconstruction in the Antarctic Muon and Neutrino Detector Array (AMANDA), Ph.D. thesis, University of California, Berkeley, 2001

[22] Geenen, H., Energy reconstruction and spectral unfolding of atmospheric leptons with the AMANDA detector, diploma thesis, Wuppertal, 2002

[23] Heck, D., et al. 1998, Report FZKA 6019, Forschungszentrum Karlsruhe

[24] DeYoung, T. R., Observation of Atmospheric Muon Neutrinos with AMANDA, Dissertation, University of Wisconsin - Madison

[25] Knapp, J., Heck, D., & Schatz, G. 1996, Report FZKA 5828, Forschungszentrum Karlsruhe

[26] Heck, D., Schröder, F., et al., Proc. 26th ICRC (Salt Lake City, 1999)

[27] Heck, D., et al., CORSIKA: A Monte Carlo Code to Simulate Extensive Air Showers, physics manual distributed together with CORSIKA sources

[28] NSSDC: http://nssdc.gsfc.nasa.gov/space/model

[29] NGDC: http://www.ngdc.noaa.gov/seg/potfld/geomag.html, IGRF95 model

[30] dCORSIKA update report: http://area51.berkeley.edu/~dima/work/BKP/DCS/REPORT8/paper.ps.gz

[31] Volkova, L.V. 1980, Sov. J. Nucl. Phys. 31, 784

[32] Muon Monte Carlo: a new high-precision tool for muon propagation through matter, ICRC 2001; updated results here: http://area51.berkeley.edu/~dima/work/

[33] suggested by Paolo Desiati, data provided by Buford Price (2002)

[34] Boziev, S. N., et al., 1989, INR preprint P-0630, Moscow

[35] Desiati, P., & Rhode, W., 27th ICRC, HE 205 Hamburg, 2001

[36] mmc code homepage is http://area51.berkeley.edu/~dima/work/MUONPR/
mmc code available at http://area51.berkeley.edu/~dima/work/MUONPR/BKP/mmc.tgz

[37] Numerical Recipes (W. H. Press, B. P. Flannery, S. A. Teukolsky, W. T. Vetterling), Cambridge University Press, 1988

[38] Winterer, V.-H., SYMPHONY (talk)

[39] Bugaev, E., Sokalski, I., & Klimushin, S., hep-ph/0010322, hep-ph/0010323, 2000

[40] Schröder, F., Rhode, W., & Meyer, H., 27th ICRC, HE 2.2 Hamburg, 2001

[41] Daum, K., et al., Frejus Coll. 1995, Z. Phys. C 66, 417 Determination of the atmospheric neutrino spectra with the Frejus detector

[42] The European Physics Journal C vol. 15, pp 163-173, 2000

[43] Rossi, B., High Energy Particles, Prentice-Hall, Inc., Englewood Cliffs, NJ, 1952

[44] Kelner, S.R., Kokoulin, R.P., & Petrukhin, A.A., About Cross Section for High Energy Muon Bremsstrahlung, Preprint of Moscow Engineering Physics Inst., Moscow, 1995, no 024-95

[45] Bethe, H., & Heitler, W, Proc. Roy. Soc., A146, 83 (1934)

[46] Bethe, H., Proc. Cambr. Phil. Soc., 30, 524 (1934)

[47] Kelner, S.R., Kokoulin, R.P., & Petrukhin, A.A., Bremsstrahlung from Muons Scattered by Atomic Electrons, Physics of Atomic Nuclei, Vol 60, No 4, 1997, 576-583

[48] Bezrukov L.B., & Bugaev, E.V., Nucleon shadowing effects in photonuclear interactions, Sov. J. Nucl. Phys. 33(5), May 1981

[49] Kokoulin, R.P., Nucl. Phys. B (Proc. Suppl.) 70 (1999) 475-479

[50] Rhode, W., Diss. Univ. Wuppertal, WUB-DIS- 93-11 (1993); W. Rhode, Nucl. Phys. B. (Proc. Suppl.) 35 (1994), $250 - 253$

[51] ZEUS Collaboration, Z. Phys. C, 63 (1994) 391

[52] Kelner, S.R., & Kotov, Yu.D., Muon energy loss to pair production, Soviet Journal of Nuclear Physics, Vol 7, No 2, 237, (1968)

[53] Kokoulin, R.P., & Petrukhin, A.A., Analysis of the cross section of direct pair production by fast muons, Proc. 11th Int. Conf. on Cosmic Ray, Budapest 1969

[54] Kokoulin, R.P., & Petrukhin, A.A., Influence of the nuclear form factor on the cross section of electron pair production by high energy muons, Proc. 12th Int. Conf. on Cosmic Rays, Hobart 6 (1971), A 2436

[55] Kelner, S., Kokoulin, R., & Petrukhin, A., Direct Production of Muon Pairs by High-Energy Muons, Phys. of Atomic Nuclei, Vol. 63, No 9 (2000) 1603

[56] Butkevitch, A., Kokoulin, R., Matushko, G., & Mikheyev, S., Comments on multiple scattering of high-energy muons in thick layers, hep-ph/0108016, 2001

[57] Klein, S., Suppression of bremsstrahlung and pair production due to environmental factors, Rev. Mod. Phys., Vol 71, No 5 (1999) 1501

[58] Migdal, A., Bremsstrahlung and Pair Production in Condensed Media at High Energies Phys. Rev., Vol. 103, No 6 (1956) 1856

[59] Polityko, S., Takahashi, N., Kato, M., Yamada, Y., & Misaki, A., Muon's Behaviors under Bremsstrahlung with both the LPM effect and the Ter-Mikaelian effect and Direct Pair Production with the LPM effect, hep-ph/9911330, 1999

[60] Stanev, T., Vankov, Ch., Streitmatter, R., Ellsworth, R., & Bowen, T., Development

of ultrahigh-energy electromagnetic cascades in water and lead including the Landau-Pomeranchuk-Migdal effect Phys. Rev. D 25 (1982) 1291

[61] Ternovskii, F., Effect of multiple scattering on pair production by high-energy particles in a medium, Sov. Phys. JETP, Vol 37(10), No 4 (1960) 718

[62] Abramowicz, H., Levin, E., Levy, A., & Maor, U., A parametrization of $\sigma_T(\gamma^* p)$ above the resonance region for $Q^2 \geq 0$, Phys. Lett. B269 (1991) 465

[63] Abramowicz, H., & Levy, A., The ALLM parametrization of $\sigma_{tot}(\gamma^* p)$ an update, hep-ph/9712415, 1997

[64] Dutta, S., Reno, M., Sarcevic, I., & Seckel, D., Propagation of Muons and Taus at High Energies, hep-ph/0012350, 2000

[65] Badelek, B., & Kwiencinski, J., The low-Q^2, low-x region in electroproduction, Rev. Mod. Phys. Vol 68 No 2 (1996) 445

[66] Whitlow, L., Rock, S., Bodek, A., Dasu, S., & Riordan, E., A precise extraction of $R = \sigma_L/\sigma_T$ from a global analysis of the SLAC deep inelastic e-p and e-d scattering cross sections, Phys. Lett. B250 No1,2 (1990) 193

[67] Badelek, B., Kwiecinski, J., & Stasto, A., A model for F_L and $R = F_L/F_T$ at low x and low Q^2, Z. Phys. C 74 (1997) 297

[68] Bouchta, A., Muon Analysis with the AMANDA-B Four-String Detector, Ph.D. thesis, Stockholm University, 1998

[69] Askebjer, P., et al., Optical properties of the South Pole ice at depths between 0.8 and 1 kilometer, Science 267 (1995) 1147

[70] Pandel, D., Bestimmung von Wasser- und Detectorparametern und Reconstruction von Muonen bis 100 TeV mit dem Baikal-Neutrinoteleskop NT-72, diploma thesis, 1996

[71] Hundertmark, S., Vertical Ice Properties for the AMANDA-Simulation, AMANDA internal report No 20001001, also see http://www.amanda.wisc.edu/karle/ptd/

[72] Jelly, J. V., Cerenkov Radiation and its Applications, Pergamon Press, New York, 1958

[73] Volkova, L. V., Lebedev Physical Institute Report No. 72, 1969

[74] Bugaev, E. V., et al., Atmospheric Muon Flux at Sea Level, Underground and Underwater, hep-ph/9803488, also Phys. Rev. D58, 05401 (1998)

[75] Kelner, S., Kokoulin, R., & Petrukhin, A., Radiation Logarithm in the Hartree-Fock Model, Phys. of Atomic Nuclei, Vol. 62, No. 11, (1999) 1894

[76] Abramowicz, H., private communication (2001)

Appendix A

CORSIKA Tables

A.1 Spectra of primaries

Table A.1: Spectra of primaries (parametrized as $\Phi_0 E^{-\gamma}$) used in CORSIKA implementation for AMANDA-II (from [1])

El-t.	charge	at. weight	Φ_0	$\sigma(\Phi_0)$	γ	$\sigma(\gamma)$	χ^2
H	1	1.00797	0.1057	0.003	2.76	0.02	0.7
He	2	4.0026	0.0673	0.002	2.63	0.02	2.1
Li	3	6.939	0.00208	0.00051	2.54	0.09	0.9
Be	4	9.0122	0.000474	4.8E-05	2.75	0.04	0.37
B	5	10.811	0.000895	7.9E-05	2.95	0.05	0.45
C	6	12.0112	0.0106	0.0001	2.66	0.02	1.42
N	7	14.0067	0.00235	8.E-05	2.72	0.05	1.91
O	8	15.9994	0.0157	0.0004	2.68	0.03	1.7
F	9	18.9984	0.000328	4.8E-05	2.69	0.08	0.47
Ne	10	20.183	0.0046	0.0001	2.64	0.03	3.14
Na	11	22.9898	0.000754	3.3E-05	2.66	0.04	0.36
Mg	12	24.312	0.00801	0.00026	2.64	0.04	0.1
Al	13	26.9815	0.00115	0.00015	2.66	0.04	1.24
Si	14	28.086	0.00796	0.00015	2.75	0.04	0.1
P	15	30.984	0.00027	2.E-05	2.69	0.06	0.68
S	16	32.064	0.00229	0.00024	2.55	0.09	0.44
Cl	17	35.453	0.000294	1.9E-05	2.68	0.05	2.36
Ar	18	39.948	0.000836	3.8E-05	2.64	0.06	0.45
K	19	39.102	0.000536	1.5E-05	2.65	0.04	4.58
Ca	20	40.08	0.00147	0.00012	2.7	0.06	0.6
Sc	21	44.956	0.000304	1.9E-05	2.64	0.06	0.81
Ti	22	47.9	0.00113	0.00014	2.61	0.06	5.67
V	23	50.942	0.000631	2.8E-05	2.63	0.05	6.83
Cr	24	51.996	0.00136	0.00012	2.67	0.06	3.41
Mn	25	54.938	0.00135	0.00014	2.46	0.22	5.38
Fe	26	55.847	0.0178	0.0018	2.6	0.09	1.81
Co	27	58.933	7.51E-05	3.7E-06	2.72	0.09	1.13
Ni	28	58.71	0.000996	4.3E-05	2.51	0.18	5.47

A.2   Atmosphere parameters

Table A.2: Mass overburden parameter definitions

[0:4] km	
[4:10] km	$T(h) = a_i + b_i \cdot e^{-h/c_i}, i = 1, ..., 4$
[10:40] km	
[40:100] km	
[100:112.8] km	$T(h) = a_5 - b_5 \cdot h/c_5, b_5 = 1$

Table A.3: Atmosphere parameters (fit to [28])

	1	2	3	4	5
a_i, g/cm^2	-137.656	-37.9610	.222659	$-6.16201 \cdot 10^{-4}$	0.00207722
	-163.331	-65.3713	.402903	$-4.79198 \cdot 10^{-4}$	0.00188667
	-142.801	-70.1538	1.14855	$-9.10269 \cdot 10^{-4}$	0.00152236
	-128.601	-39.5548	1.13088	$-26.4960 \cdot 10^{-4}$	0.00192534
b_i, g/cm^2	1130.74	1052.05	1137.21	442.512	1.
	1183.70	1108.06	1424.02	207.595	1.
	1177.19	1125.11	1304.77	433.823	1.
	1139.99	1073.82	1052.96	492.503	1.
c_i, cm	867358.	741208.	633846.	759850.	$5.4303203 \cdot 10^9$
	875221.	753213.	545846.	793043.	$5.9787908 \cdot 10^9$
	861745.	765925.	581351.	775155.	$7.4095699 \cdot 10^9$
	861913.	744955.	675928.	829627.	$5.8587010 \cdot 10^9$

Appendix B

Influence of the Magnetic Field on the Shower Propagation with CORSIKA

Figures B.1−B.3 demonstrate the influence of the magnetic field on the deviation of muons from the direction of the primary (here called scattering). At zenith angles close to $90°$ such "magnetic" scattering is particularly strong. Therefore, a large number of upgoing primaries can produce downgoing secondaries. This can be accounted for by generating a few degrees worth of upgoing primaries at just below the horizon. Here up- and down- going primaries are meant in the detector frame, i.e., at least $1.3°$ below the value at which CORSIKA cuts away particles ($90°$). Apparently a small number of particles visible in the detector frame is still lost due to tracking algorithm imperfections, as seen in Figure B.1, which shows a small excess of negative over positive $\delta\theta$ deviations of muons from directions of primaries. This excess is exacerbated by the presence of the magnetic field, which adds significantly to the particle scattering.
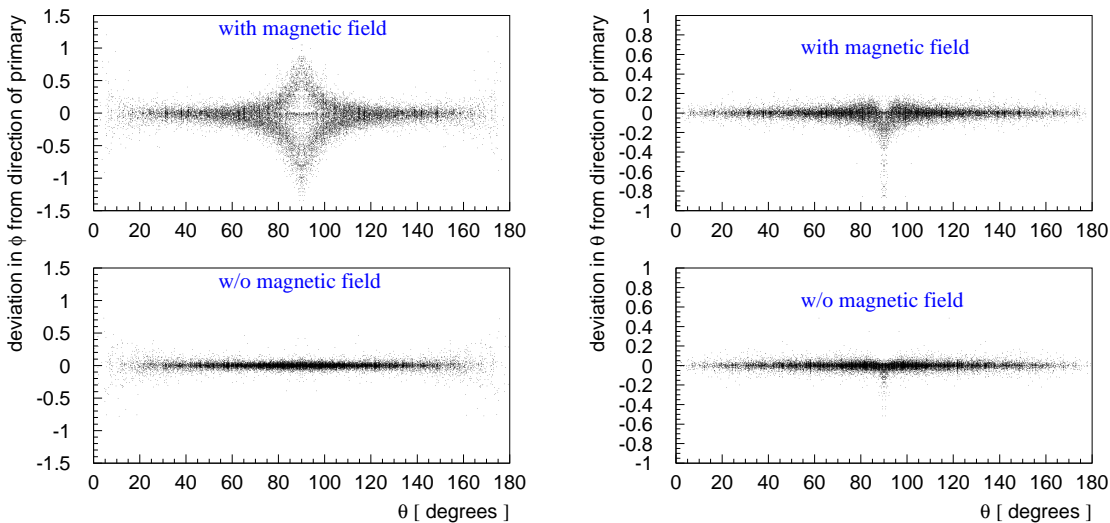
Figure B.1: Deviation of secondaries from primaries
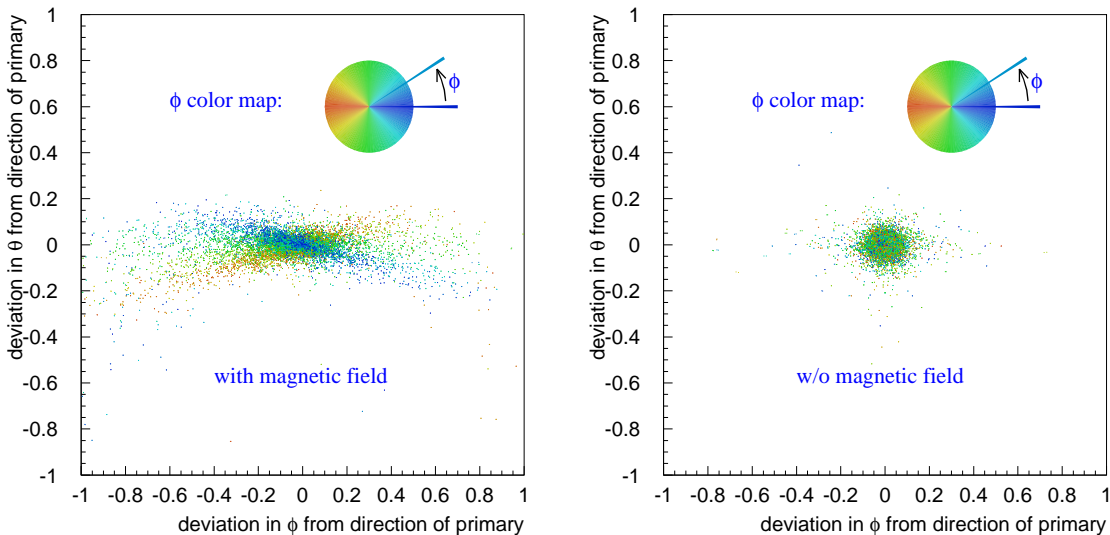
Figure B.2: Deviation of secondaries from primaries $\delta\theta$ vs. $\delta\phi$, ϕ color map
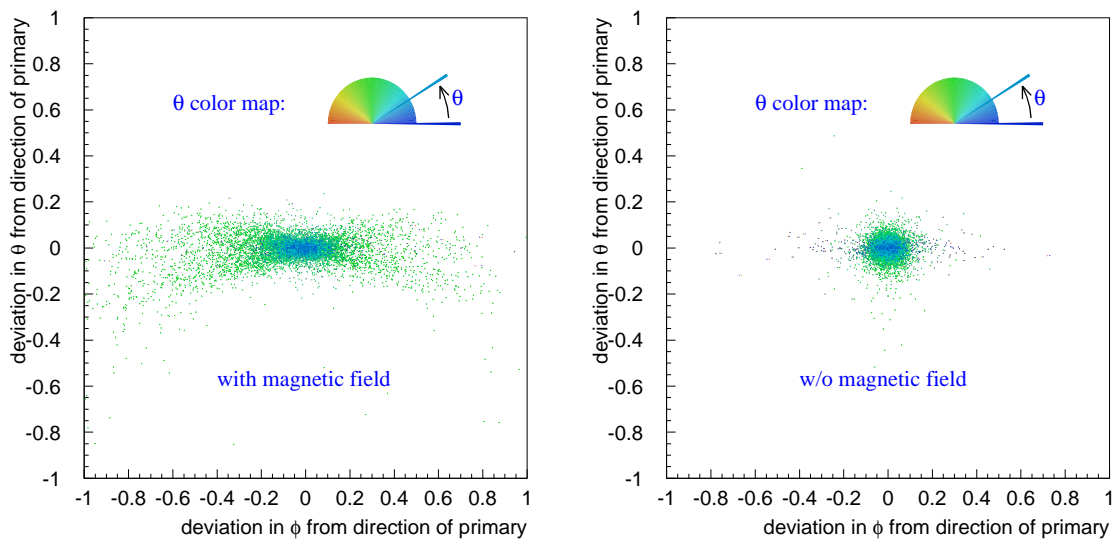
Figure B.3: Deviation of secondaries from primaries $\delta\theta$ vs. $\delta\phi$, θ color map

Appendix C

Tables used by Muon Monte Carlo

(MMC)

All cross sections were translated to units $[1/\mathrm{cm}]$ via multiplication by the number of molecules per unit volume. Many unit conversions (like eV $\rightarrow$ J) were achieved using values of $\alpha = e^2/\hbar c$ and $r_e = e^2/m_e c^2$.

Table C.1: Summary of physical constants employed by MMC

α	1/137.03599976	r_e	$2.817940285 \cdot 10^{-13}$ cm
N_a	$6.02214199 \cdot 10^{23}$ 1/mol	K	$0.307075\ MeV \cdot cm^2/g$
c	$299792458 \cdot 10^{10}$ cm/s	R_y	13.60569172 eV
m_e	0.510998902 MeV	m_π	139.57018 Mev
m_p	938.271998 MeV	m_n	939.56533 MeV
m_μ	105.658389 MeV	τ_μ	$2.19703 \cdot 10^{-6}$ s
m_τ	1777.03 MeV	τ_τ	$290.6 \cdot 10^{-15}$ s

Table C.2: Media constants

Material	Z	A	I, eV	C	a	m	X_0	X_1	$\rho, g/cm^2$
Water	1 +	1.00794	75.0	-3.5017	0.09116	3.477	0.240	2.8004	1.000
Ice	+ 8	15.9994	75.0	-3.5017	0.09116	3.477	0.240	2.8004	0.917
Stand. Rock	11	22	136.4	-3.774	0.083	3.412	0.049	3.055	2.650
Fréjus Rock	10.12	20.34	149.0	-5.053	0.078	3.645	0.288	3.196	2.740
Iron	26	55.845	286.0	-4.291	0.147	2.963	-0.001	3.153	7.874
Hydrogen	1	1.00794	21.8	-3.263	0.135	5.625	0.476	1.922	0.063
Lead	82	207.200	823.0	-6.202	0.094	3.161	0.378	3.807	11.350
Uranium	92	238.0289	890.0	-5.869	0.197	2.817	0.226	3.372	18.950

Table C.3: Radiation logarithm constant B (taken from [75])

Z	B	Z	B	Z	B	Z	B	Z	B
1	202.4	8	173.4	15	172.2	22	176.8	53	178.6
2	151.9	9	170.0	16	173.4	26	175.8	74	177.6
3	159.9	10	165.8	17	174.3	29	173.1	82	178.0
4	172.3	11	165.8	18	174.8	32	173.0	92	179.8
5	177.9	12	167.1	19	175.1	35	173.5		
6	178.3	13	169.1	20	175.6	42	175.9	other	182.7
7	176.6	14	170.8	21	176.2	50	177.4		

Table C.4: ALLM parameters (as in [63, 76])

|					
a_{P1}	-0.0808	a_{P2}	-0.44812	a_{P3}	1.1709
a_{R1}	0.58400	a_{R2}	0.37888	a_{R3}	2.6063
b_{P1}	0.60243^2	b_{P2}	1.3754^2	b_{P3}	1.8439
b_{R1}	0.10711^2	b_{R2}	1.9386^2	b_{R3}	0.49338
c_{P1}	0.28067	c_{P2}	0.22291	c_{P3}	2.1979
c_{R1}	0.80107	c_{R2}	0.97307	c_{R3}	3.4942
m_P^2	$49.457 \cdot 10^6$ MeV^2	Λ^2	$0.06527 \cdot 10^6$ MeV^2	m_0^2	$0.31985 \cdot 10^6$ MeV^2
m_R^2	$0.15052 \cdot 10^6$ MeV^2	$Q_0^2 - \Lambda^2$	$0.46017 \cdot 10^6$ MeV^2		

Appendix D

Comparison of Spectra of Secondaries Produced with MMC, MUM, LOH, and LIP

D.1 Spectra of the secondaries

In order to determine spectra of primaries consistently for all codes, the following setup was used. For each muon with fixed initial energy a first secondary created within the first 20 meters is recorded (Figure D.1). This is somewhat different from what was done for Figure 3.7, since the energy of the muon at the moment when the secondary is created is somewhat smaller than the initial energy due to continuous energy losses. These are smaller when v_{cut} is smaller, and are generally negligible for all cases considered below.

In Figures D.2−D.11 solid curves are probability functions normalized to the total num-

Figure D.1: Spectra of the secondaries: the setup
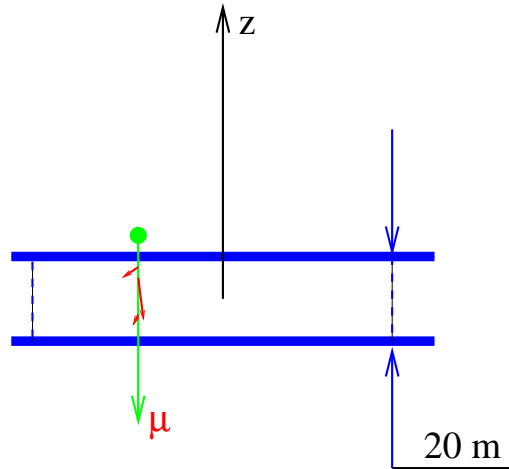
ber of secondaries above 500 MeV. In Figures D.12−D.15 solid curves are probability functions normalized to the total number of secondaries above $10^{-3} \cdot E_\mu$. In Figures D.16−D.19 solid curves are probability functions normalized to the total number of secondaries above $10^{-2} \cdot E_\mu$. A setting of $E_{big} = 10^{21}$ GeV is used for Figures D.5−D.7 (default is 10^{11} GeV).
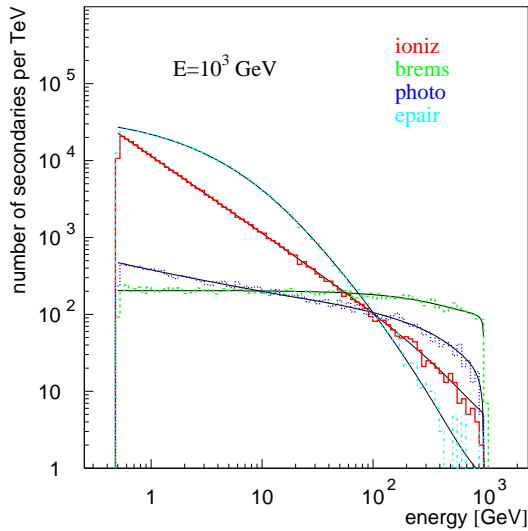
Figure D.2: MMC: $E_\mu = 10^3$ GeV, $E_{cut} = 500$ MeV
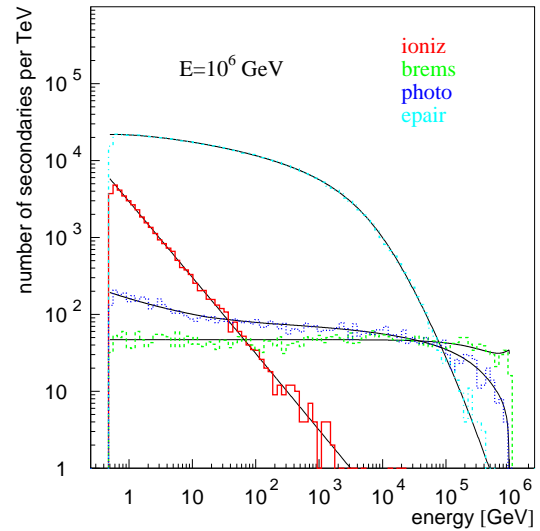
Figure D.3: MMC: $E_\mu = 10^6$ GeV, $E_{cut} = 500$ MeV

Figure D.4: MMC: $E_\mu = 10^9$ GeV, $E_{cut} = 500$ MeV

Figure D.5: MMC: $E_\mu = 10^{12}$ GeV, $E_{cut} = 500$ MeV
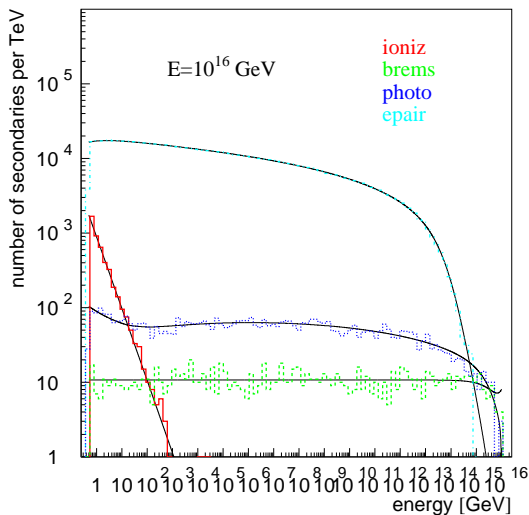
Figure D.6: MMC: $E_\mu = 10^{16}$ GeV, $E_{cut} = 500$ MeV
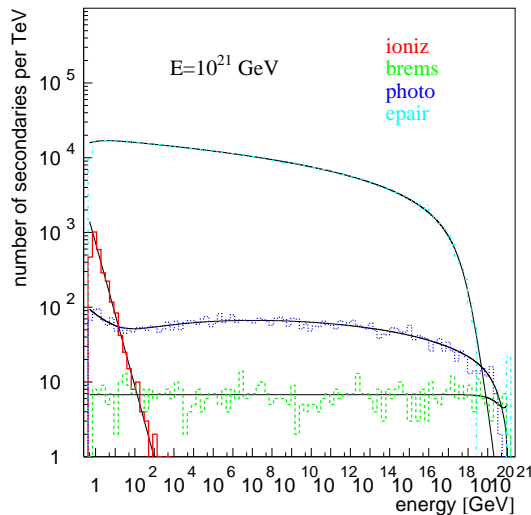
Figure D.7: MMC: $E_\mu = 10^{21}$ GeV, $E_{cut} = 500$ MeV
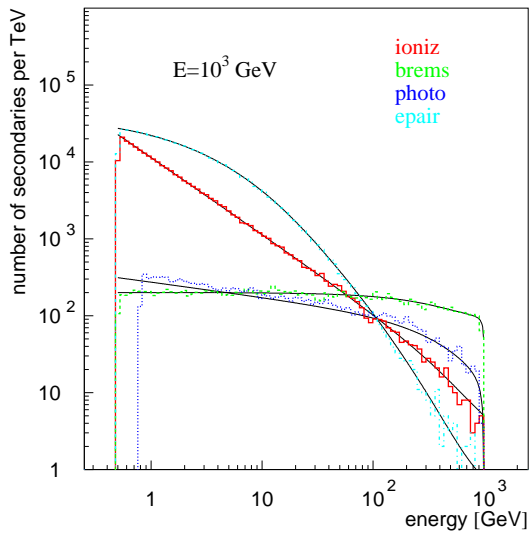
Figure D.8: MUM: $E_\mu = 10^3$ GeV, $E_{cut} = 500$ MeV
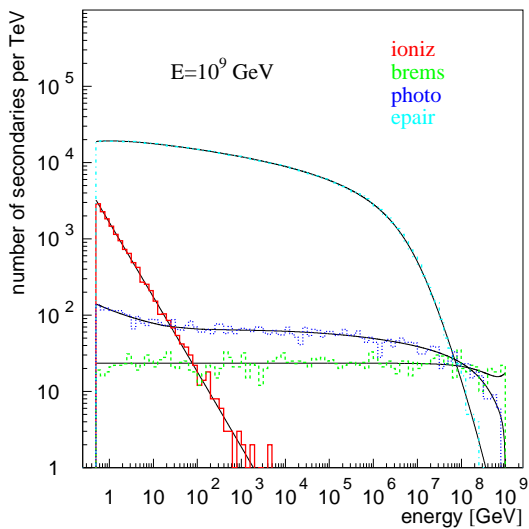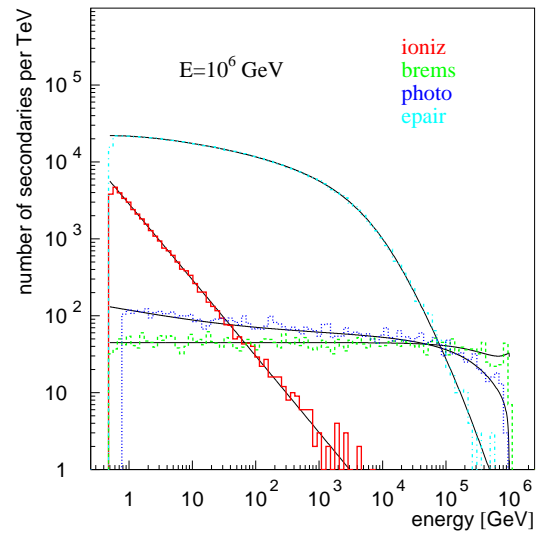

Figure D.9: MUM: $E_\mu = 10^6$ GeV, $E_{cut} = 500$ MeV

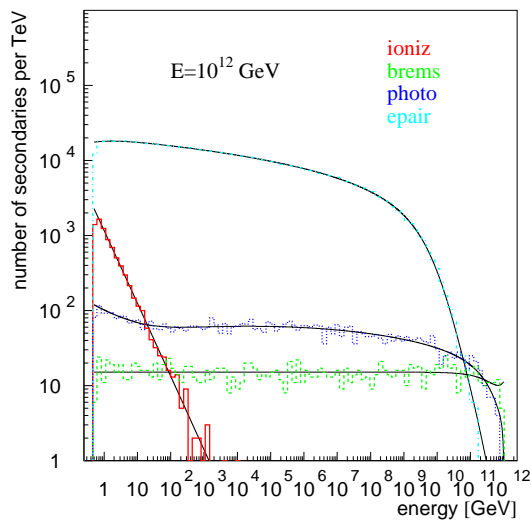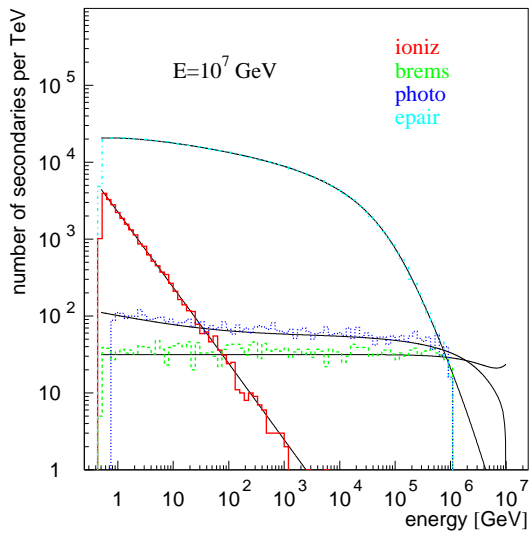Figure D.10: MUM: $E_\mu = 10^7$ GeV, $E_{cut} = 500$ MeV
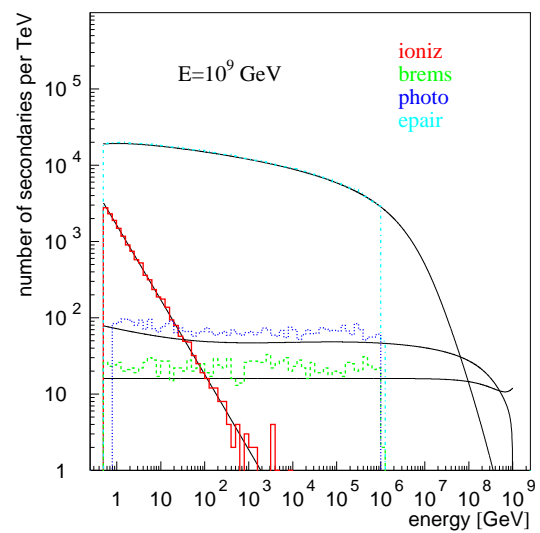
Figure D.11: MUM: $E_\mu = 10^9$ GeV, $E_{cut} = 500$ MeV
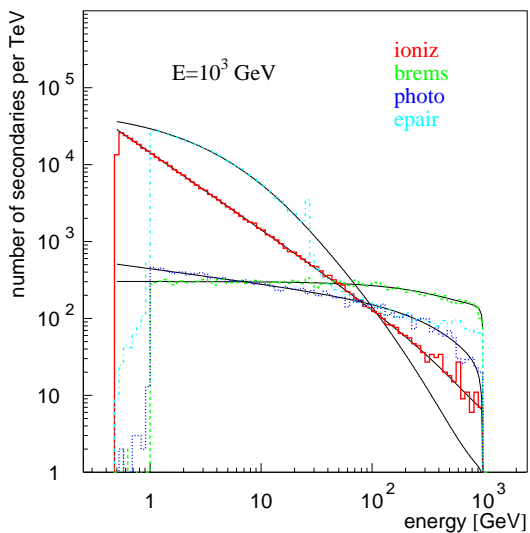
Figure D.12: LOH: $E_\mu = 10^3$ GeV
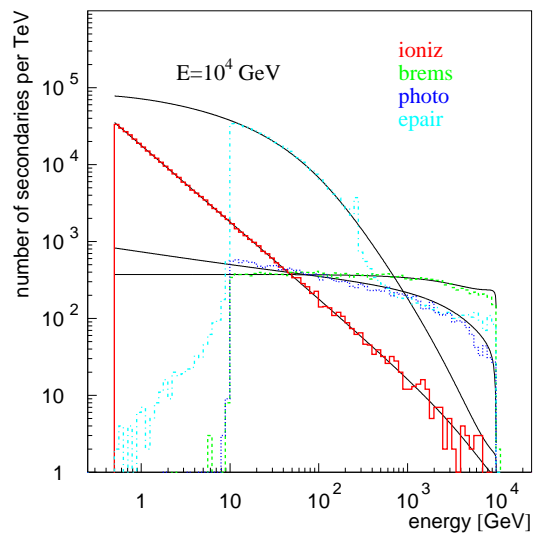
Figure D.13: LOH: $E_\mu = 10^4$ GeV
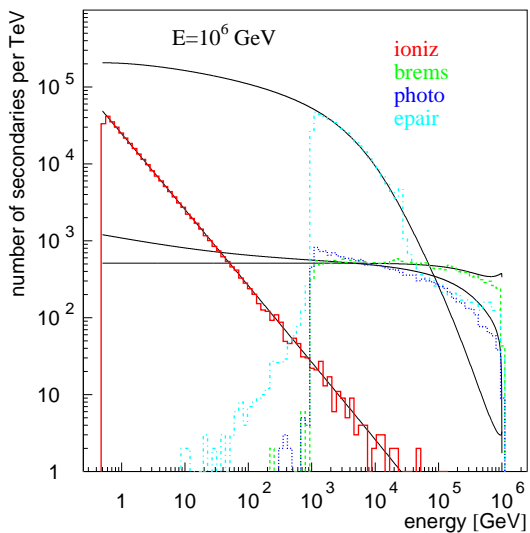
Figure D.14: LOH: $E_\mu = 10^6$ GeV
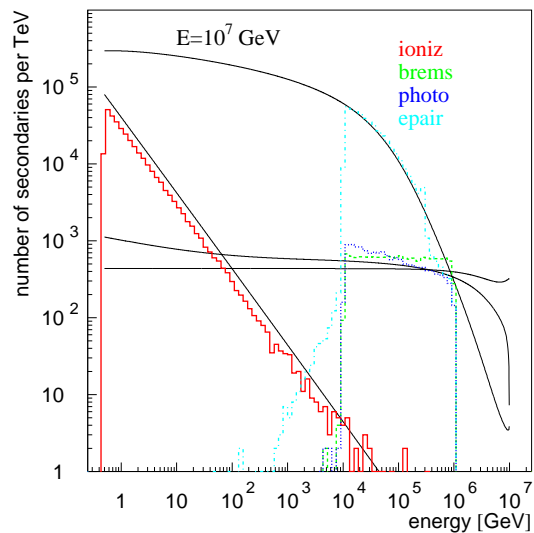
Figure D.15: LOH: $E_\mu = 10^7$ GeV
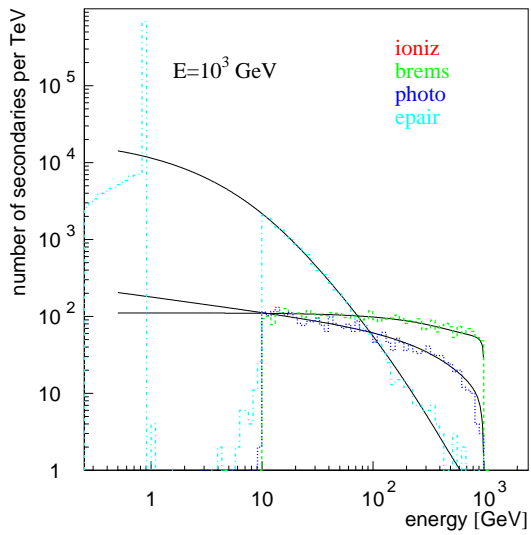
Figure D.16: LIP: $E_\mu = 10^3$ GeV
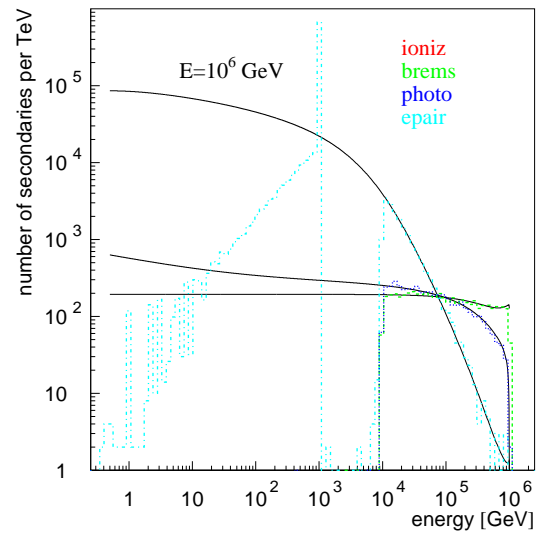
Figure D.17: LIP: $E_\mu = 10^6$ GeV
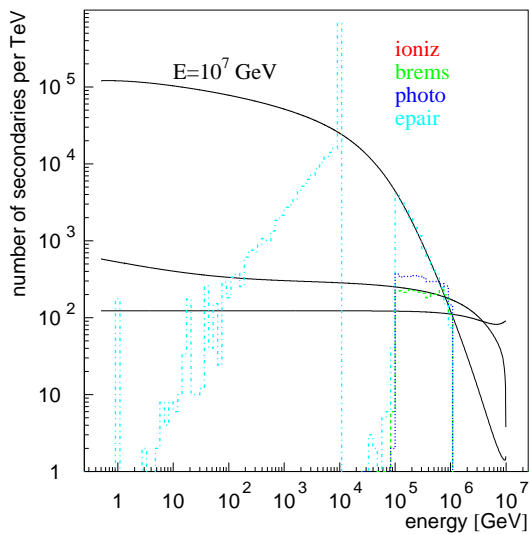
Figure D.18: LIP: $E_\mu = 10^7$ GeV
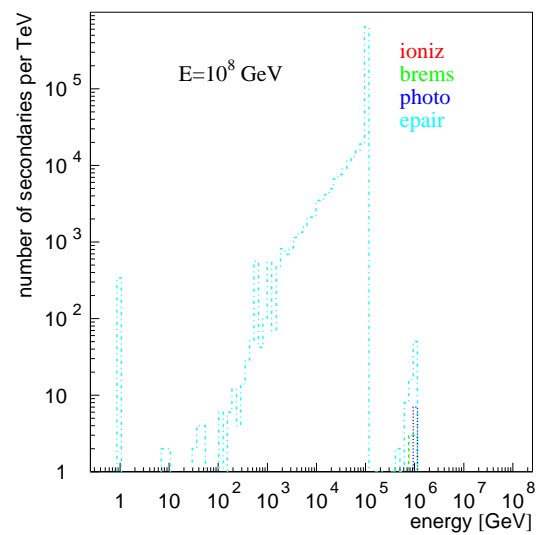
Figure D.19: LIP: $E_\mu = 10^9$ GeV

D.2   Tracking and energy integrals

$$\int_{E_i}^{E_f} \frac{\sigma(E)}{-f(E)} \cdot dE = -\log(\xi) \quad \text{(energy integral)}.$$

$$x_f = x_i - \int_{E_i}^{E_f} \frac{dE}{f(E)} \quad \text{(tracking integral)}.$$

Figure D.20: Tracking and energy integrals: derivation (see Section 3.3.1)

$$\text{x}_i \qquad \text{dx} \qquad\qquad\qquad \text{x}_f$$

Most common behavior of tracking and energy integrals is shown in Figures D.21−D.26.
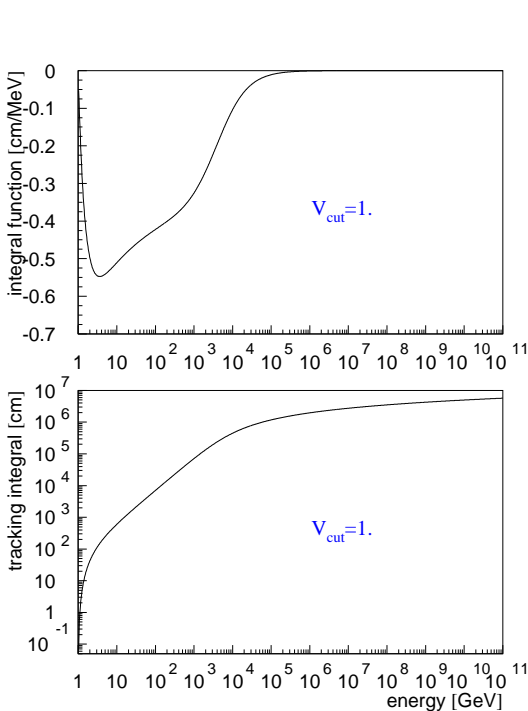
Figure D.21: Tracking Integral: $v_{cut} = 1$.
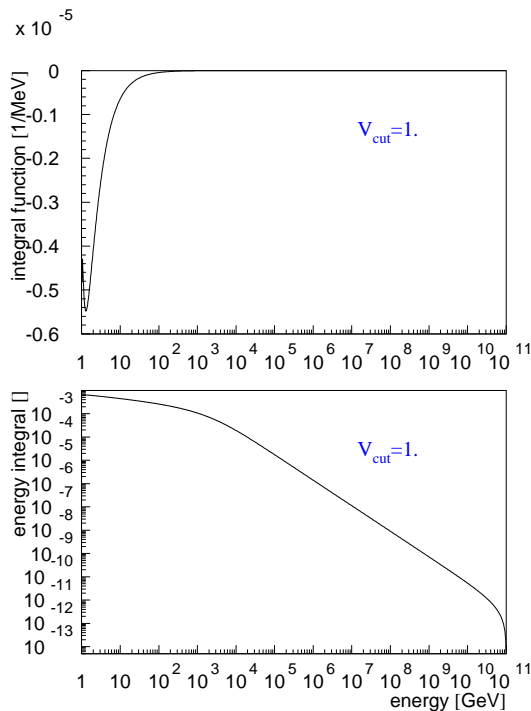
Figure D.22: Energy Integral: $v_{cut} = 1$.
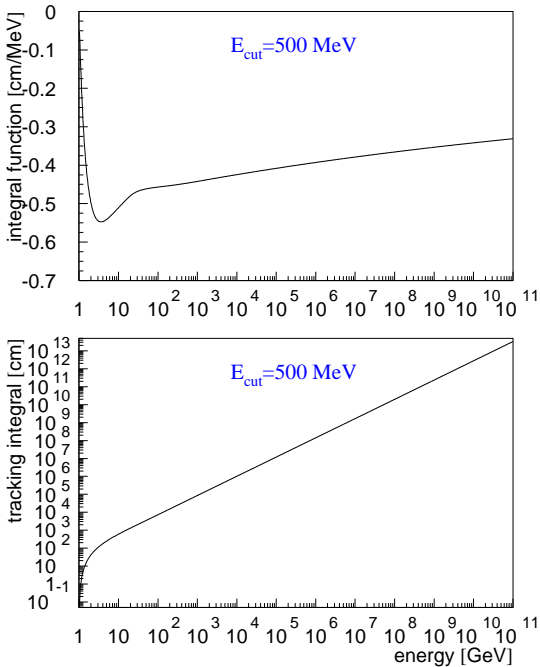
Figure D.23: Tracking Integral: $E_{cut} = 500$ MeV
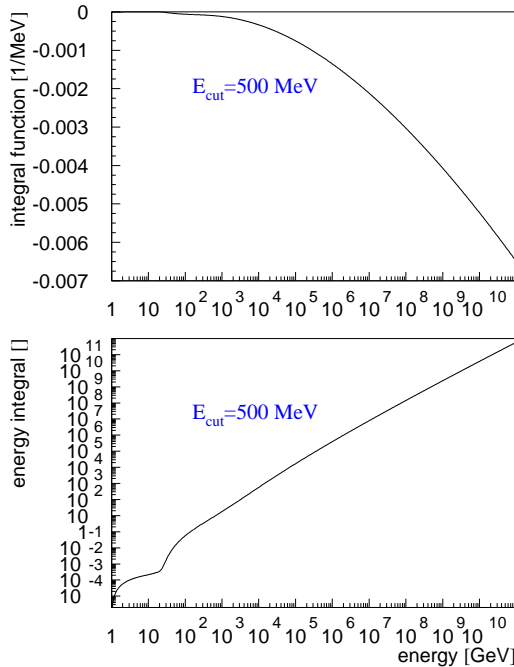
Figure D.24: Energy Integral: $E_{cut} = 500$ MeV
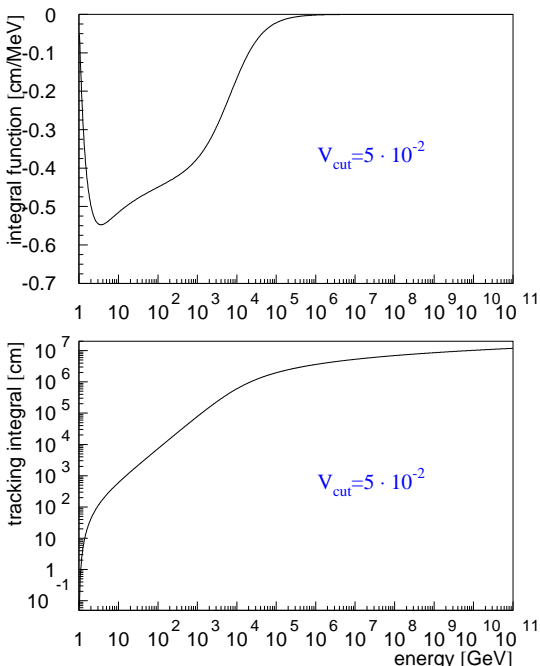
Figure D.25: Tracking Integral: $v_{cut} = 0.05$
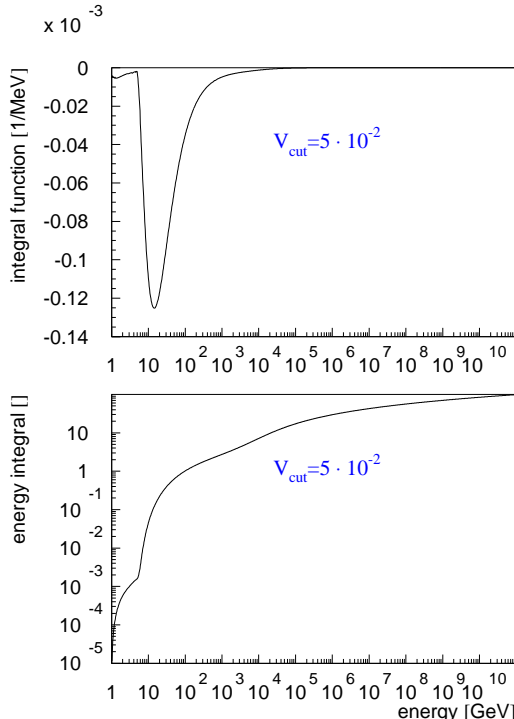
Figure D.26: Energy Integral: $v_{cut} = 0.05$

D.3 Number and total energy of secondaries
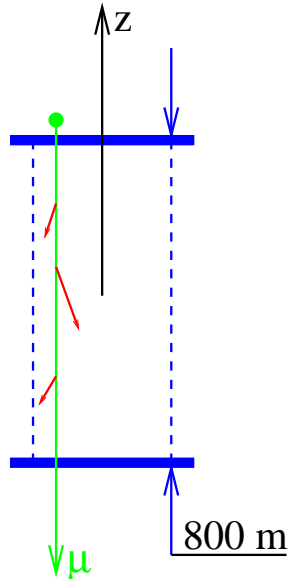
Figure D.27: Number and total energy of secondaries: the setup
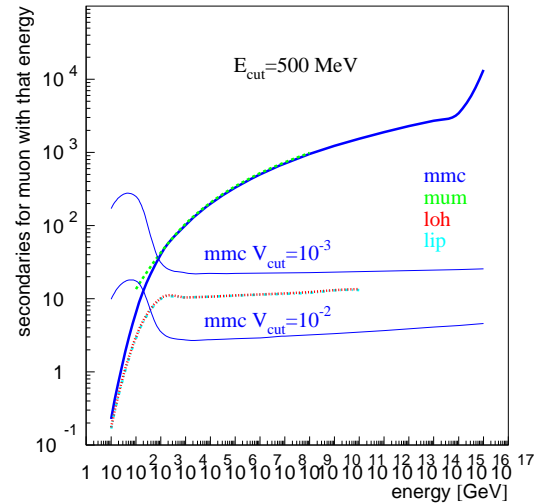
Figure D.28: Number of secondaries

In spite of the numerous problems with propagation codes other than MMC, shown in Figures D.8−D.19, it was possible to use these codes in the simulation of AMANDA-II. To understand why, the following setup is used. For each muon with fixed initial energy all secondaries created within the first 800 meters (equal to the height of the AMANDA-II detector) are recorded (Figure D.27). Although the number of secondaries generated by propagators LOH and LIP is different from that generated by MMC or MUM (Figure D.28), the total energy deposited in the volume of the detector is commensurable between all four propagators. The number of generated secondaries depends on the chosen value of E_{cut} or v_{cut}. While MMC and MUM allow one to select this value, LOH and LIP have a built-in value which cannot be changed. From Figure D.28 it appears that these codes use a value of v_{cut} which lies between 10^{-2} and 10^{-3} since their number of secondaries lies between that generated with MMC with $v_{cut} = 10^{-2}$ and $v_{cut} = 10^{-3}$. One would expect the total

energy of secondaries generated with LOH or LIP to be somewhat lower than that generated with MMC or MUM with $E_{cut} = 500$ MeV. This, however, is not true: the total energy of secondaries generated with LOH and LIP is somehow renormalized to match that of MMC and MUM (Figures D.29 and D.30).
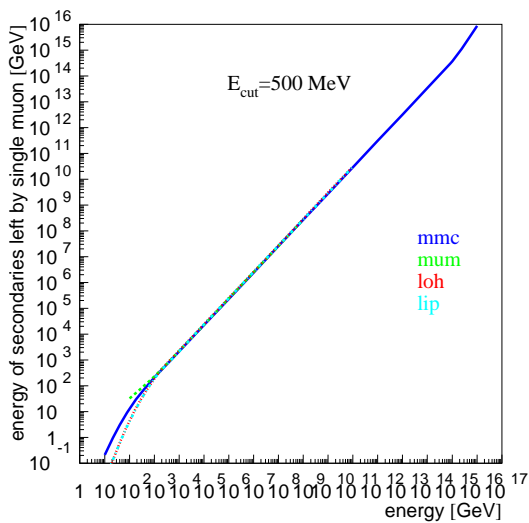
Figure D.29: Total energy of secondaries   Figure D.30: Relative energy of secondaries
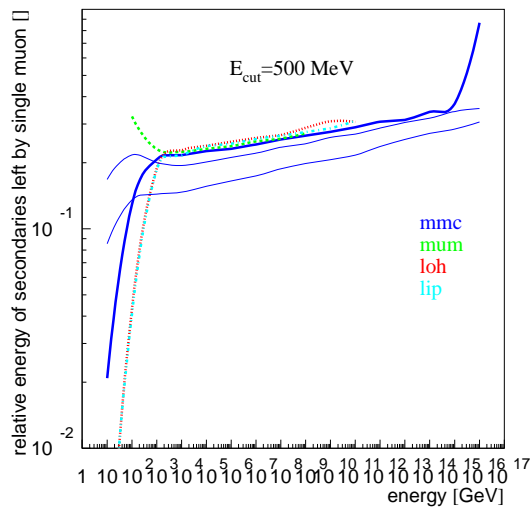
Figures D.28 and D.30 also demonstrate the region of energies for which MMC can be used: with fixed $E_{cut} = 0.5$ GeV, MMC seems to work for energies up to $0.5 \cdot 10^{15}$ GeV (determined mainly by the computer precision with which double precision numbers can be added: $0.5/0.5 \cdot 10^{15} \sim 10^{-15}$).

Appendix E

Main Analysis Supplements

E.1   Ice model definitions

Production of the simulated data used in this work was done using the Monte Carlo chain as shown in Figure 1.6. Figure E.1 shows the main features of the simulated data samples. High energy interaction models used by CORSIKA for the air shower generation were introduced in Section 2.2. Here different ice parameter sets are described.

The chosen method of photon propagation for this work is based on PTD [71]. This depends on the ice parameters. The following parameter sets were used:

1. **bulk** ice: assumes homogeneous optical properties.

2. **f125** ice: same as bulk, but scattering and absorption have been increased by F=1.25.

3. **stdkurt** ice: (standard Kurt) uses layered ice parameters (see Figure 4.3 for scattering coefficient).

4. **sudkurt** ice: (Sudhoff-Kurt) same as *stdkurt*, but different glass measurements which increase sensitivity by $\sim 25\%$.

5. **kgm** ice: (Kurt-Gary model) similar to *stdkurt*, but based on the best ice measurements as of Fall 2001, on average $\sim 20\%$ more scattering, $0 - 25$ % more absorption than in *stdkurt*.

6. **mam** ice: (Modified absorption model) starting from *kgm* model, absorption was increased to match time residuals of the arriving signals between data and Monte Carlo.

7. **mamint** ice: Same as mam, but using newer simulation package with multiple updates in software.

Points in plots 4.34 and 4.36 were averaged for each set (i.e., average parameters were calculated using all z-layers at -10 m $< z < 10$ m). The result is shown in Figures E.2 and E.3. The newest ice parameter sets are shown in black triangles (*mamint* and *kgm* models). The overall description of data with these new parameter sets is much converged (and is close to data points along their corresponding parabolas) compared to the range of the previous generation of the ice models.

E.2   Detector configuration uncertainties

In order to estimate uncertainties in the knowledge of the detector configuration (position and signal calibration of the OMs, etc.) and errors due to cross talk, detector configuration parameters were varied. Figures E.4 and E.5 show stability of the found spectral index correction with respect to these changes. The variance in the result obtained with different settings was taken as the "detector configuration error," or *conf* in the results.
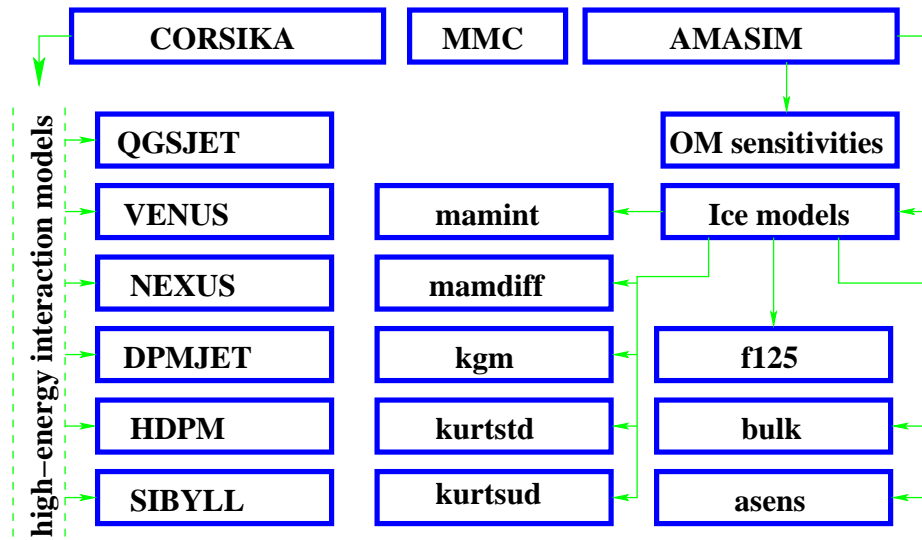
Figure E.1: Summary of simulation settings
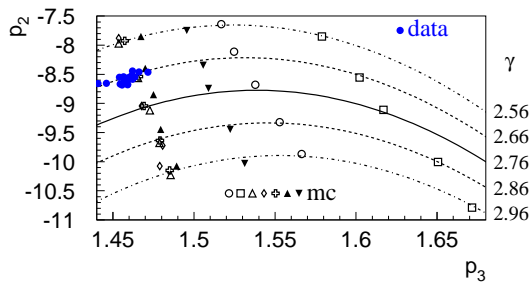
Figure E.2: Correlation p_1 with p_3

Figure E.3: Correlation p_2 with p_3

simulated data samples (mc, left to right): stdkurt, sudkurt, f125, mam, bulk, mamint, kgm
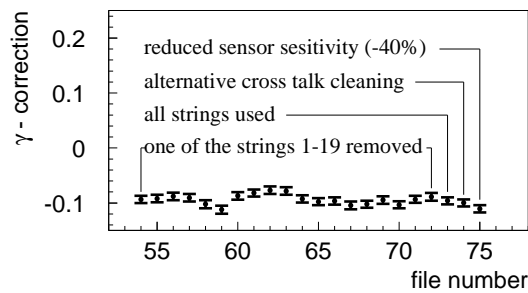
Detector configuration error estimate, spectral index

Figure E.4: 1st method
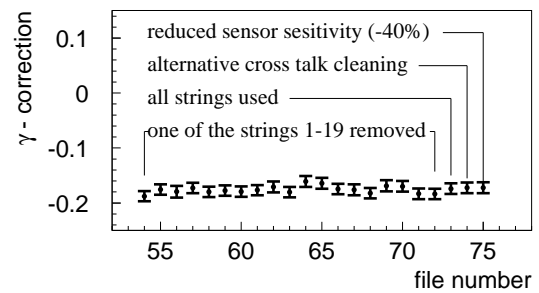
Figure E.5: 2nd method
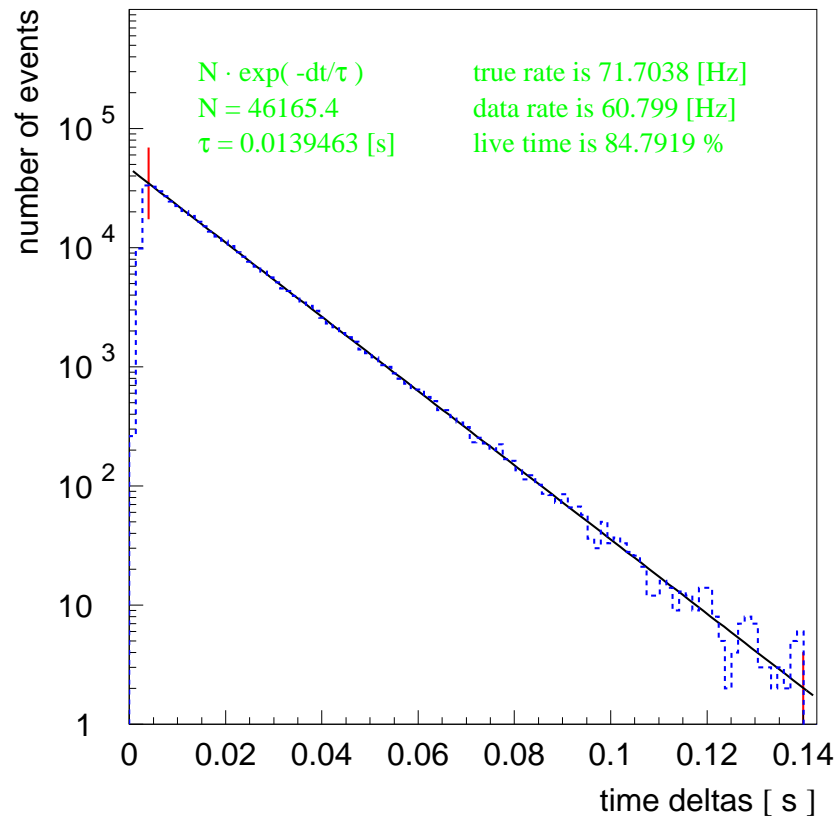
Figure E.6: Dead time calculation

E.3 Dead time correction

When the AMANDA-II electronics is triggered, its DAQ[1] takes some time to scan through its hardware and record the event. If during this process another event occurs, it will not be recorded, thus resulting in some loss of events. For each data sample time differences between consecutive events were histogrammed (Figure E.6) and an exponential was fit to the resulting distribution. The inverse of the time constant of the exponential gives the "true" data rate, which is what is expected if there were no hardware dead time. The measured data rate divided by this number gives the fraction of time the detector was operational.

[1]Digital acquisition system.

Appendix F

Software Parameters

F.1 CORSIKA configuration

Default CORSIKA configuration file INPUTS used is shown in Figure F.1. UCR (Utility for CORSIKA shower core Randomization) available parameters are shown in Figure F.2. COR-SIKA was run with **CORSIKA < INPUTS > printout**. Its output is then randomized with **ucr -out=out.gz DAT000001.gz -oms -tr=2 -over=1 -cmt=INPUTS -run=**[run number, here **1**] **-SHOWERS=10^6 -FLUXSUM=**[taken from the CORSIKA output; **0.1584** m^{-2}sr^{-1}s^{-1} for settings shown] **-LENGTH=800 -RADIUS=400 -DEPTH=1730 -HEIGHT=2834 -EARTHR=6**.4· **10^6 -DCORR=35 -cutfe=273. -curved=4 -cutth=85**.

```
RUNNR   1                           number of run
EVTNR   1                           number of first shower event
NSHOW   1000000                     number of showers to generate
PRMPAR  14                          particle type of prim. particle
ESLOPE  -2.7                        slope of primary energy spectrum
ERANGE  600.  1.E11                 energy range of primary particle
THETAP  0.  89.999                  range of zenith angle (degree)
PHIP    0.  360.                    range of azimuth angle (degree)
SEED    1   0   0                   seed for 1. random number sequence
SEED    2   0   0                   seed for 2. random number sequence
SEED    3   0   0                   seed for 3. random number sequence
OBSLEV  2834.E2                     observation level (in cm)
ELMFLG  T  F                        em. interaction flags (NKG,EGS)
RADNKG  2.E5                        outer radius for NKG lat.dens.determ.
ARRANG  0.                          rotation of array to north
FIXHEI  0.  0                       first interaction height & target
FIXCHI  0.                          starting altitude (g/cm**2)
MAGNET  16.4  -53.4                 magnetic field south pole
HADFLG  0  1  0  1  0  2            flags hadr.interact. & fragmentation
QGSJET  T  0                        use qgsjet for high energy hadrons
QGSSIG  T                           use qgsjet hadronic cross sections
ECUTS   273. 273. .003 .003         energy cuts for particles
MUADDI  T                           additional info for muons
MUMULT  T                           muon multiple scattering angle
LONGI   F  20.  F  F                longit.distr. & step size & fit
MAXPRT  0                           max. number of printed events
ECTMAP  100                         cut on gamma factor for printout
STEPFC  1.0                         mult. scattering step length fact.
DEBUG   F  6  F  1000000            debug flag and log.unit for out
DIRECT  ../output/                  output directory
ATMOD   13                          october atmosphere
DETCFG  1.                          detector information (l/d)
F2000   T                           choses F2000 format
LOCUT   T 1.58                      enables skew angle cutoff
RANPRI  T                           random primary
SPRIC   T                           separate primary energy cutoffs
FSEED   T                           enable random generator seed recovery
DSLOPE  0.                          slope correction
SCURV   T 6.4E8 1.73E5              curved surf., radius of Earth, depth
EXIT                                terminates input
```

Figure F.1: CORSIKA configuration INPUTS file

```
This program merges F2000 files, v0.02
Available options are: -h  = -help  print this message and quit
                       -q  = -quit  quit immediately
                       -out=[NAME]  change output file to NAME
                       -tr=[NUM]  output only events with # of tracks >= NUM
                       -over=[..] oversample by this number, default is 1
                       -r = -randomize randomize shower core xy locations
                       -c = -curved same for curved Earth's surface
                       -curved=[1-4] different curved surface treatment:
                         1: only downgoing primaries (th from 0 to 90 deg.)
                         2: only upgoing primaries (th from 90 to 180 deg.)
                         3: decide at random, either goes up or down
                         4: oversample x2 each event with th > cutth
                       -phi = -rphi     also randomize azimuth angle
                       -cutth=[degrees]     value used for -curved=4
                       -EARTHR=[radius]     of the Earth              [m]
                       -LENGTH=[length]     of the detector           [m]
                       -RADIUS=[radius]     of the detector           [m]
                       -DEPTH=[depth]       of the detector center    [m]
                       -HEIGHT=[altitude]   of the ice surface        [m]
                       -DCORR=[correction] depth correction (35 m) [m]
                       -rmpri   remove primaries
                       -rmusr   remove user blocks
                       -oms     output only muons
                       -ohm     leave only muon with highest energy per event
                       -msn     leave only muon and neutrinos, delete others
                       -cmt=[file]     append comments contained in the file
                       -run=[number]  set the run number
                       -FLUXSUM=[CORSIKA's value]    per meter2 second sr
                       -SHOWERS=[number] of showers generated by CORSIKA
                       -rr      remove possible previous xy randomization
                       -rr=[DEPTH]   and set the previous value of DEPTH
                       -test [num] [theta] [phi]    test xy randomization
                       -cutfe=[GeV]  angle-dependent cutoff energy for muons
                       -corr change time definitions to be Basiev-compatible
```

Figure F.2: UCR (Utility for CORSIKA shower core Randomization) parameters

```
This program propagates muons in Ice to/through the detector
Available options are: -length=[LENGTH of the detector volume in meters]
                       -radius=[RADIUS of the detector volume in meters]
                       -vcut=[value of vcut used for the 1st region]
                       -ecut=[ecut in  MeV  used for the 2nd region]
                       -medi=[medium name]
                       -mediadef=[file with media definitions]
                       -tau  propagate taus instead of muons
                       -sdec enable stopped muon decay treatment
                       -user     enable the mmc_en user line
                       -user=[z] same, but record energy at z, not CPD
                       -rdmc      enforce compliance with rdmc
                       -amasim   turn on workarounds for amasim
                       -time precise time of flight calculation
                       -cont enable continuous loss randomization
                       -scat enable Moliere scattering
                       -lpm  enable lpm treatment
                       -allm enable allm photonuclear parametrization
                       -phnu=[1-4] choose another photonuclear formula
                       -elow=[muon energy in GeV below which it is lost]
                       -ebig=[upper bound in GeV of the paramet. tables]
                       -surf=[h in meters]  propagate to the plane z=[h]
                       -face  only if detector is on opposite side of it
                       -maxbuf=[max number of lines per event] (10000)
                       -romb=[number of interpolation points]
                       -seed=[integer] sets random number generator seed
                       -raw  save tables in raw format
                       -tdir=[dir] specify directory for paramet. tables
```

Figure F.3: MMC (Muon Monte Carlo) parameters

F.2 MMC configuration

MMC (Muon Monte Carlo) available parameters are shown in Figure F.3. MMC was run

as follows: **ammc -r -a -length=800 -radius=400 -romb=5 -raw -user -sdec -time -cont -lpm**

-allm -scat -amasim. MMC user line is defined as follows:

USER_DEF mmc_en NR E_INI E_CPD E_IN E_OUT CDP_X CDP_Y CDP_Z Z_IN Z_OUT,

where the parameters are (in their order): muon track number, its initial energy, its energy at the

point of closest approach to the center of the detector, its energy when entering and exiting the

detector cylinder, coordinates of the point of closest approach, and z-coordinate when entering and

exiting the detector cylinder.